HIGH ENERGY PHOTON PRODUCTION IN NUCLEAR REACTIONS

By

Chui Ling Tam

A DISSERTATION

Submitted to

Michigan State University

in partial fulfillment of the requirements

for the degree of

DOCTOR OF PHILOSOPHY

Department of Physics

1989

ABSTRACT

HIGH ENERGY PHOTON PRODUCTION IN NUCLEAR REACTIONS

By

Chui Ling Tam

The production of high energy gamma rays (E_γ> 20 MeV) was studied using three Cherenkov telescopes. Each telescope consists of a BaF_2 active converter placed in front of the Cherenkov counter stack. The efficiency and the energy response of the detector were calibrated at the University of Illinois tagged photon facility. The efficiency of the telescope ranges from about 10% for 20 MeV photons to 20% for 80 MeV photons. The detector energy resolution varies from 30% FWHM at 20 MeV to 45% at 80 MeV.

Photon production from the following light-ion induced reactions were studied: ^{4}He + C, ^{4}He + Zn and ^{4}He + Pb at energies E/A = 25 MeV and 53 MeV; and ^{2}H + C, ^{2}H + Zn and ^{2}H + Pb at E/A = 53 MeV. The photon double differential cross sections are exponentially decreasing with increased energy. The slope parameters are steeper than those found in heavy-ion induced reactions at similar energies. The angular distributions in the nucleon-nucleon center-of-mass have larger dipole components than in heavy-ion induced reactions. We observed both target and projectile dependence in

the slope parameters and angular distributions. Calculations based on first-chance neutron-proton bremsstrahlung model was able to reproduce the projectile dependence of the slope parameters.

Photon production from the following 30 MeV/nucleon heavy-ion induced reactions were also studied: symmetric systems ^{7}Li + Li, ^{20}Ne + Mg and ^{40}Ar + Ca and the asymmetric systems ^{7}Li + Pb and ^{40}Ar + Pb. The energy spectra and the angular distributions are quite similar to those observed in earlier experiments. The ratios of total cross section for systems having different masses agree with predictions of the first-chance n-p bremsstrahlung model.

ACKNOWLEDGEMENTS

I wish to thank the faculty and staff of the National Superconducting Cyclotron Laboratory for their support of the completion of this dissertation.

I would like to specially thank my research advisor Professor Ed Kashy for his guidance during my graduate career. Many thanks go to Professor Walter Benenson and Professor John Stevenson, without their help, this dissertation would be all blank pages. I would also like to thank Professor George Bertsch and Professor Wolfgang Bauer for the many helpful discussions.

Finally, many hearty thanks go to my fellow graduate students for their friendship which made the endless working hours much more enjoyable.

TABLE OF CONTENTS

END OF TABLE

LIST OF FIGURES

LIST OF TABLES

Chapter 1

Introduction

Since the production of high energy gamma rays (E_γ>20 MeV) in intermediate energy heavy-ion collisions was discovered in 1984 by two independent groups at GSI [Gr 85] and MSU [Be 86], there has been a large amount of experimental and theoretical work done in this area. The study of high energy gamma ray production is quite interesting because, unlike the measurement of subthreshold pion production, the photons are not reabsorbed within the surrounding nuclear matter. So in spite of the difficulty in measuring its small cross-section, the production of high energy gamma ray should provide a relatively clean probe of the reaction dynamics in intermediate energy heavy ion reactions. (The term high energy indicates a greater energy than expected for nuclear level transitions, including decay of the giant dipole states.)

Several theoretical models have been proposed to explain these gamma rays at such relatively high energy. The majority of these models are based on the nucleon-nucleon or nucleus-nucleus bremsstrahlung during the very early stages of the reaction.

One early model suggested by Vasak et. al.[Va 85], attributed the production of the high energy gamma rays to coherent nucleus-nucleus bremsstrahlung. For symmetric systems, the destructive interference between bremsstrahlung from the acceleration of the projectile nucleus and from the

target nucleus would lead to a quadrupole angular distribution in the center-of-mass frame. The gamma ray yield depends on Z^2 and becomes most significant in heavier systems.

Also in an early attempt to reproduce the data from GSI and MSU group, both Nakayama and Bertsch [Na 86] and Bauer et al. [Ba 86a] arrived at the conclusion that the contribution of the nucleon bremsstrahlung from nuclear potential field is unimportant compared to the contribution of the individual nucleon-nucleon collisions.

Most of the more recent models of high energy gamma ray production suggest that gamma rays come from incoherent neutron-proton bremsstrahlung within the two colliding nuclei. For example, Bauer et al. [Ba 86b] conducted a dynamical study based on the Boltzmann-Uehling-Uhlenbeck equation, which describes the time evolution of the nucleon phase space density during the reaction process. Nakayama and Bertsch [Na 86] did a calculation using infinite matter approximations with a first-chance zero-range n-p interaction, and Remington et al. [Re 86] incorporated a semiclassical bremsstrahlung formula into the Boltzmann master equation [Ha 68]. These models all assume that the microscopic mechanism is individual nucleon-nucleon bremsstrahlung and that gamma rays are produced in the early stage of the reaction.

Nifenecker and Bondorf [Ni 85] introduced a different approach, which attributes the photon production to the multiple scattering during the later stages of the collision. In this approach, the gamma rays are produced by incoherent nucleon-nucleon collisions within a recoiling fireball formed by part of the target and projectile nucleons. The kinetic energy of the participating nucleons is assumed to be converted to thermal energy of the

fireball, so that gamma rays of relatively high energy can be produced, and the predicted angular distribution is expected to be isotropic in the frame of the moving source. Neuhauser and Koonin [Ne 87], combining a fireball model with the elementary nucleon-nucleon bremsstrahlung cross section, also found good agreement with experiment.

Shortly after the first high energy gamma ray observation by Beard et al. [Be 86] with the NSCL Enge Split-pole spectrograph [Sp 67], it was quite clear that a better detector system was needed for further investigation of this phenomenon. Development of a high energy gamma ray telescope made of a stack of Cherenkov plastic, conceived by Dr. J.Stevenson, began at Michigan State University. I had since begun participating actively in the detector construction and calibration and several high energy gamma ray experiments using these telescopes.

Using a pair of the high energy gamma ray telescopes, we first measured the inclusive high energy gamma ray production with ^{14}N beam at 20, 30 and 40 MeV/nucleon, and the production of high energy gamma ray in coincidence with light charged particles. Then a slightly modified third telescope was finished, and two more experiments were carried out, one measuring the light-ion induced gamma ray production, and the other gamma rays from intermediate energy symmetric systems. Later, two telescopes were taken to the Lawrence Berkeley Laboratories to perform an experiment using ^{136}Xe beam at 66, 98, and 124 MeV/nucleon. More experiments are being done here in MSU using these telescopes together with other detectors. We calibrated one of the detectors using the tagged-photon facility at the University of Illinois.

This thesis is organized as follows: Chapter 2 of this thesis covers the development of the gamma ray telescope and calibration with tagged photons. Chapter 3 describes the hardware and electronic set-up used in the actual gamma ray experiments, the method of background suppression and of extraction of experimental data. Chapter 4 presents the data from the light-ion induced high energy gamma ray production experiment and a discussion. Chapter 5 deals with the data from the near symmetric system experiment and its interpretation. In chapter 6, theorectical model calculations based on the nucleon-nucleon bremsstrahlung are presented and compared to the data. Finally, the summary and conclusions are in chapter 7.

CHAPTER 2

DESIGN AND CALIBRATION OF THE CHERENKOV TELESCOPE

A. Introduction

The gamma rays which range in energy from 20 MeV to 100 MeV and their small production cross-section present particular problems in the design of the detector system. There is also a large (10^4-10^5 times the photon yield) background of fast and slow neutrons, charged particles and low energy gamma rays. A number of different detectors have been used by various other experimental groups to measure these high energy photons.

A.1. Detection of High Energy Gamma Rays

A photon is uncharged and thus creates no direct ionization or excitation of the material through which it passes. The detection of gamma rays therefore depends on causing the photon to undergo an interaction that transfers all or part of its energy to secondary electrons in the absorbing material. These electrons can then be detected by means of the Coulomb interaction.

Although there are many possible photon interaction mechanisms known, only three major types of interactions lead to the conversion of a significant part of the photon energy to electron energy. They are: photoelectric absorption, Compton scattering, and pair production. The

relative importance of these three processes in different materials for various photon energies is illustrated in Figure II-1 [Ev 55].

In Figure II-1, the line at the left represents the photon energy at which photoelectric absorption and Compton scattering are equally probable as a function of the absorber atomic number. And the line at the right represents the photon energy and absorber atomic number at which Compton scattering and pair production are equally probable. Thus, three areas on the plot are defined within which one of the three processes dominate. It is clear that for $E_\gamma \geq 20$ MeV, photoelectric absorption is unimportant as the primary initial process.

Most of the high energy gamma ray detectors operate in the pair production zone and use material with high Z. Figure II-2 shows the relative efficiency of photon undergoing Compton scattering and pair production within BaF_2 Crystal. It is seen that for gamma rays of energy above 20 MeV, pair production plays a far more important role than Compton scattering. Currently, all detector systems used in the measurement of high energy gamma rays rely on photon pair production mechanism to convert high energy photons into electron-positron pairs.

A.2. Shower Type Detectors

Most of the shower type detectors operate on the basis of a formation of a large number of electron-positron pairs "shower" inside the detector. Shower type detectors are usually made of materials that have high atomic number Z to enhance the yield of the e^+e^- pair. In order to contain the shower, the sizes of these shower detectors are typically several radiation

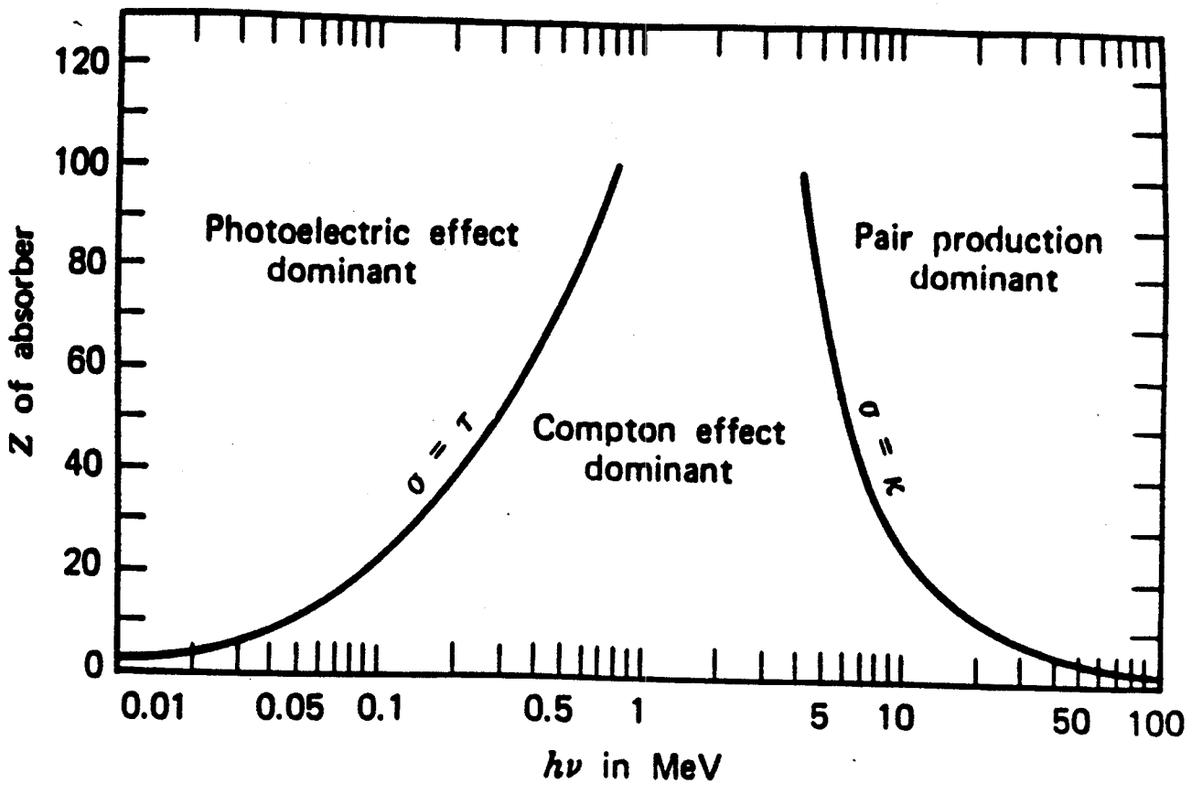

Figure II-1 Relative importance of the three major type of photon interactio as a funtion of photon energy and the atomic number of the medium [Ev 55].

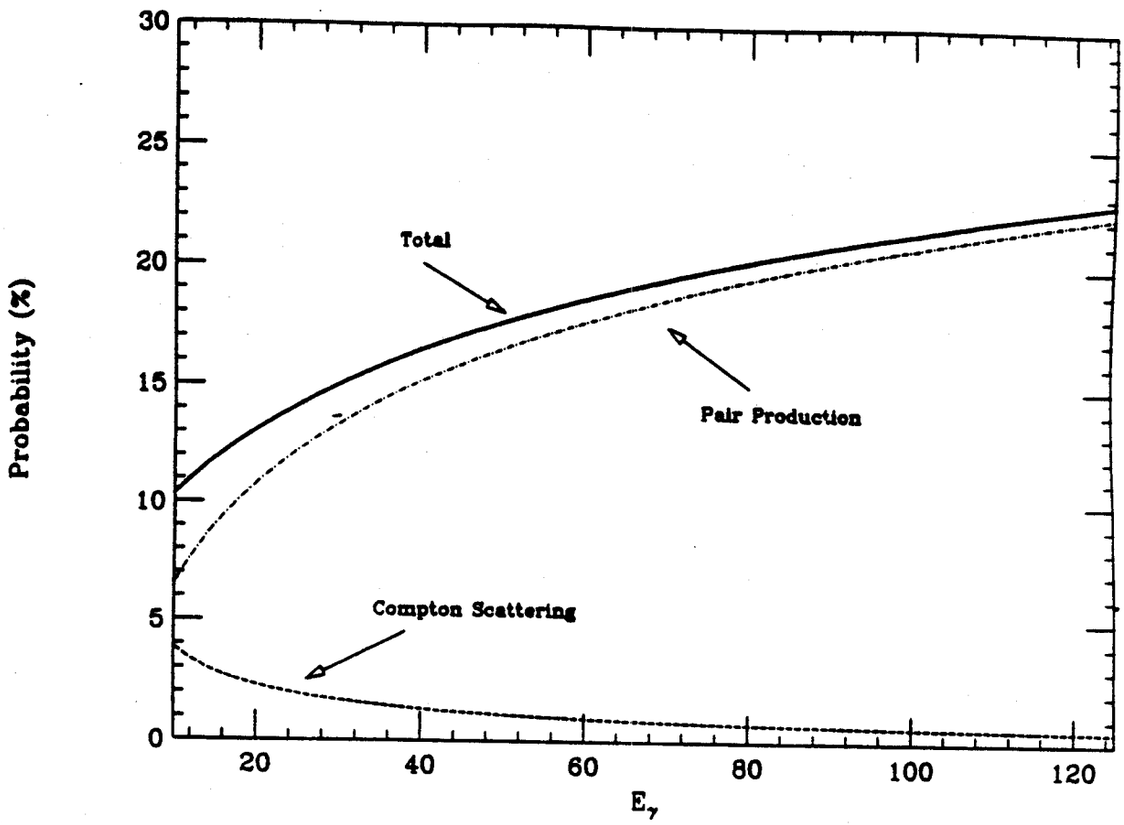

Figure II-2 The relative probability of Compton scattering vs. pair production in BaF_2.

lengths. Examples of this type of detector include lead glass detectors and large inorganic scintillators such as NaI and BaF_2.

A.2.1. Lead Glass Detector

One of the shower type detector used by several groups [Gr 86][Al 86] to detect high energy photon is the lead glass detector. In a lead glass detector, a photon is converted into an electron-positron pair either by an external converter or in the detector itself. As they pass through the detector, they emit photons by the Cherenkov mechanism. This is the well known emission of radiation observed when the velocity of a charged particle in a medium exceeds the speed of light in that medium [Ja 75a]. Because of the high atomic number of lead, these secondary electrons and positrons have a high probability of producing bremsstrahlung photons. Then, the secondary photon in turn produces more e^-e^+ pairs. This $\gamma \leftrightarrow e^+e^-$ process repeats itself many times forming a shower of electrons and positrons in the detector. The total Cherenkov light output of all the electrons and positrons is then collected and the sum gives the energy of the original photon. Because of the Cherenkov mechanism in the detector material, lead glass detectors offer the advantage of very low sensitivity to neutrons and low energy charged particles.

Lead glass detector, however, have relatively poor energy resolution for photons with energy below 100 MeV, particularly when compared to inorganic scintillator such as NaI and BaF_2. Moreover, the energy response function of a lead glass detector shows a pronounced high-energy tail that can cause serious errors in both the slopes and yields of steeply falling exponential spectra.

Herrmann et. al. made a direct comparison between a single block lead glass detector and a BaF_2 crystal using monoenergetic photons at the Mainz tagged photon facility [He 86]. The response function of the lead glass for various energies are presented in Figure II-3. The full-width at half-maximum (FWHM) of the energy resolution obtained, described by $\Delta E/E = 13.2\%/\sqrt{E(GeV)}$, is poor when compared to BaF_2 crystal. More comparisons of the energy resolution of lead glass with that of the inorganic scintillators and Cherenkov plastic range detector will be presented later. Therefore, as pointed out by Herrmann et. al., lead glass as a detector for the measurement of bremsstrahlung photons in intermediate energy should be used with great caution.

A.2.2. NaI Scintillator Detector

Inorganic scintillators are also widely used for the measurement of high energy photons. For example, the thallium-activated sodium iodide (NaI(Tl)) crystal is one of the most commonly used inorganic scintillators. In a scintillator detector, a photon is converted into an electron-positron pair either by a converter or in the detector itself. Then, as the pair passes through the detector, scintillation photons are emitted. Because of the relatively high atomic number of the crystal, these electrons and positrons also produce bremsstrahlung photons. The energetic secondary photons in turn generate more e^-e^+ pairs through the pair production process. This $\gamma \leftrightarrow e^+e^-$ process repeats itself many times, thus forming a shower of electrons and positrons in the detector. The total scintillator light output, assuming all

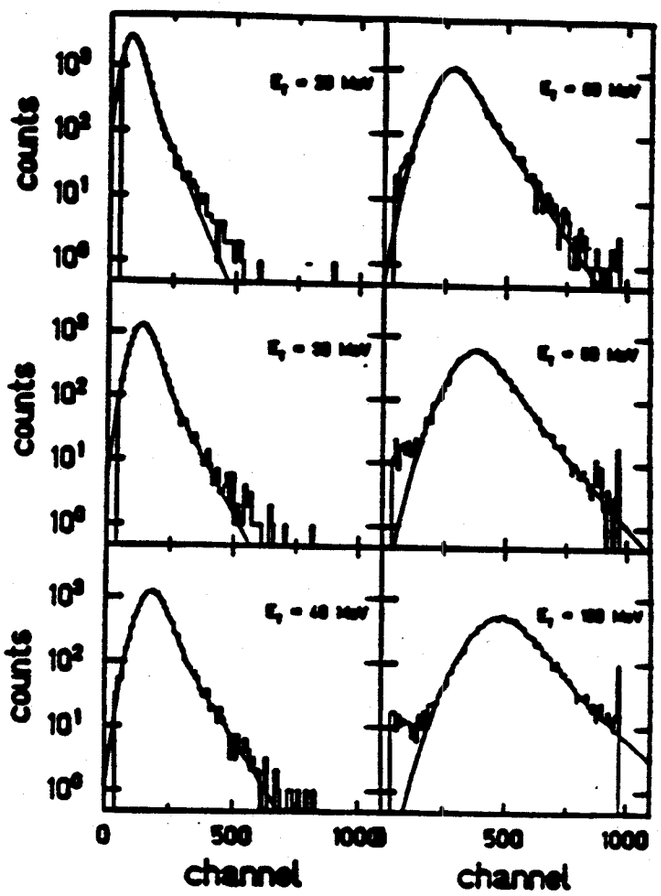

Figure II-3 The response functions of lead glass detector for energies from 20 MeV to 100 MeV [He 86].

electrons and positrons stop in the crystal, then gives the energy of the original photon.

NaI(Tl) crystal has the advantage of high light output and a close to linear response to gamma ray energy over most of the energy range. Its energy resolution is much better than that of the lead glasses. It is also possible to obtain large volume NaI crystals.

The disadvantages of NaI are that it is quite fragile and is also hygroscopic; if exposed to the atmosphere, it will deteriorate due to water absorption. Due to the large thermal neutron capture cross section of Iodine, NaI is also sensitive to neutrons, one of the major sources of background in the measurement of high energy gamma rays.

The energy resolution of NaI is predominantly limited by the loss of secondary electrons and photons escaping the detector volume. Figure II-4(a) shows the energy response of a 20 cm long and 15 cm diameter cylindrical NaI crystal illuminated by monoenergetic photon beams [Be 87]. The response is significantly better than that of the lead glass. The NaI spectrum has a low energy tail instead of the high energy tail seen in the case of lead glass. Such a low energy tail has a relatively smaller influence on exponential spectra than the high energy tail found on lead glasses.

Bertholet et.al. [Be 87] have combined a large inorganic scintillator block NaI(Tl) with a BaF_2 converter. The converter is "active", which means the light output from the converter is added to the light output of the detector, making it possible to take into account the energy lost by the e^+e^- pair in the converter. The resolution obtained for this NaI telescope detector system is a moderate $6.5\%/\sqrt{E\ (GeV)}$ (FWHM). The energy response

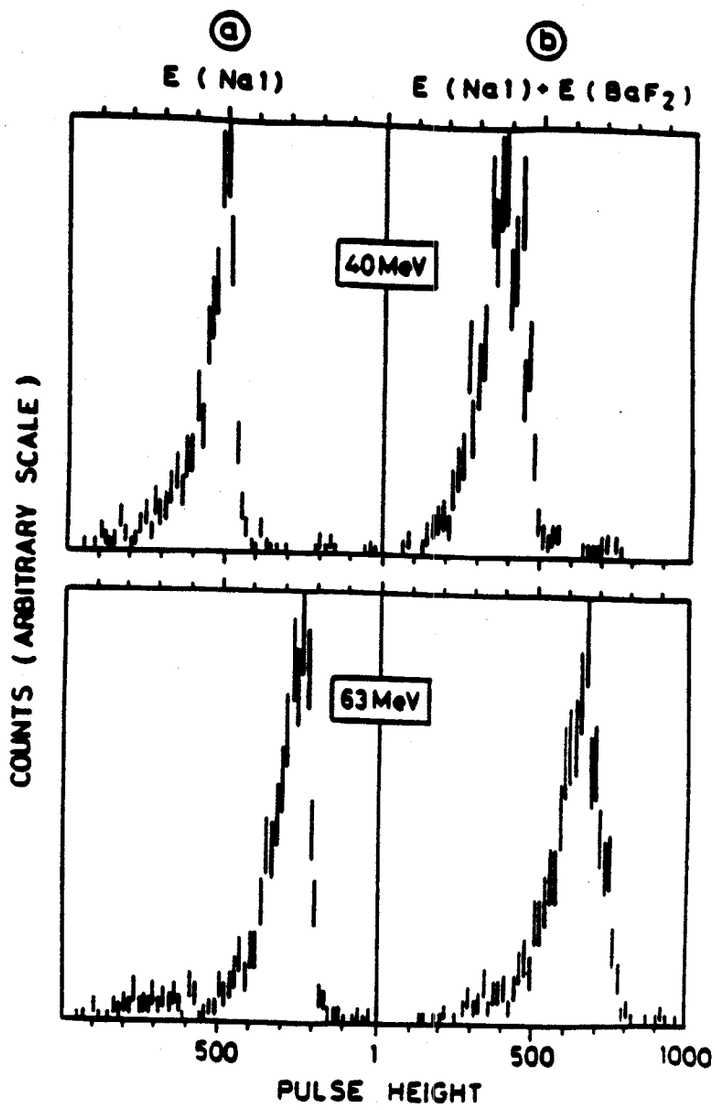

Figure II-4 The response functions of a single NaI crystal detector (a) and that of a NaI telescope with BaF_2 converter (b) [Be 87].

curves are shown in Figure II-4(b). At the end of this chapter, we will compare the energy response of the NaI telescope with that of the MSU Cherenkov plastic telescope.

A.2.3. BaF_2 Scintillator Detector

BaF_2 is a relatively new inorganic scintillator that has enjoyed more and more use in the last few years. It offers some advantages over the traditional NaI crystal detector. BaF_2 crystal, unlike NaI crystal, is not hydroscopic, so it is more stable in the air. It is less sensitive to thermal neutron capture than NaI. And it also has good time resolution (~ 400 ps) that makes for good fast neutron-gamma ray discrimination by time-of-flight when a beam with sharp time structure is used. At the present time, however, there are no single BaF_2 detectors that are large enough to contain the showers from 100 MeV gamma rays. So most of the BaF_2 detector systems consist of a cluster of several small BaF_2 whose light outputs are summed.

The energy resolution of BaF_2 detectors is also much better than that of lead glasses. Figure II-5 shows an example of the response function of a 14 X 10 cm BaF_2 crystal [Hi 87]. The resolution of the detector is $8\%/\sqrt{E\ (GeV)}$ (FWHM).

A.3. Cherenkov Plastic Telescope Detector

In the MSU Cherenkov plastic gamma ray telescope (Figure II-6), a high energy photon is converted into an electron-positron pair in the active BaF_2 converter placed in the front of the plastic Cherenkov detector stack. But

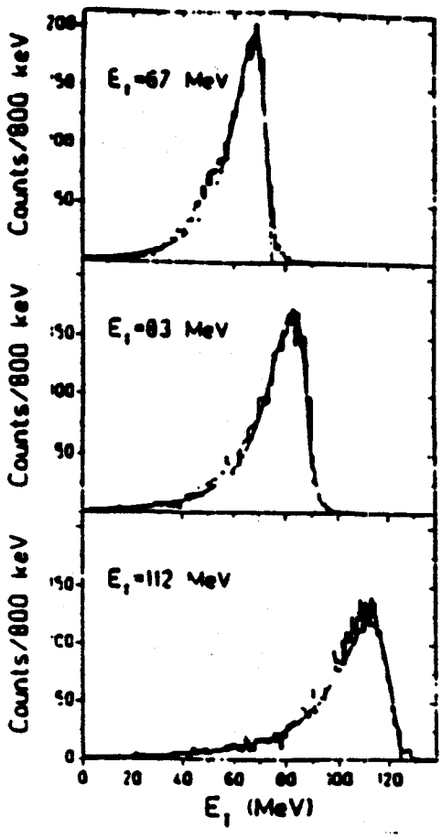

Figure II-5 Response functions of a BaF_2 detector at various energies [He 86].

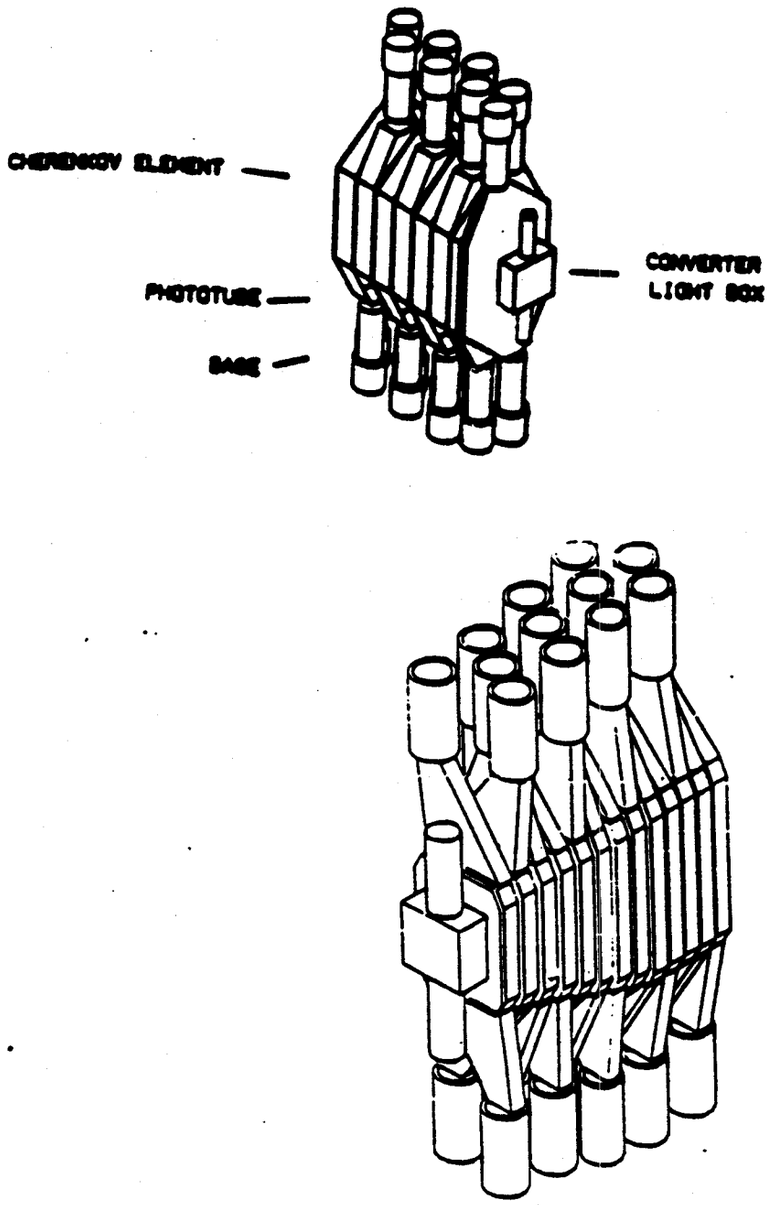

Figure II-6 A schematic picture of the Cherenkov telescopes. (a): The eight element telescope, (b): The 13 element telescope.

because of the low atomic number of the Cherenkov plastic (Lucite with a wave shifter additive), instead of forming a shower, the electron and positron simply lose all of their energy and stop in the stack. As the electron and positron travel down the stack of Cherenkov plastic, they emit Cherenkov light in the plastic elements they pass through. A waveshifter additive was added to the Cherenkov plastic which absorbs the highly directional, mostly short wave length UV Cherenkov light, and then radiates isotropically at a longer wavelength (425nm), to which the plastic is more transparent. The total energy of the photon was then obtained by the position weighted sum of the light output from each element. Since the measurement of the photon energy does not rely on shower formation, the length of this telescope is only slightly over one radiation length.

Due to the Cherenkov detection mechanism, this detector has the advantage of being very insensitive to neutrons and to low energy charged particles. Its energy resolution is better than that of the lead glass detectors for energies below 100 MeV. Also, a Cherenkov plastic telescope can usually be built at a fraction of the cost of any inorganic scintillator detector.

B. The Cherenkov Plastic High Energy Gamma Ray Telescope

B.1. The Construction of the Three Cherenkov Telescopes

The first two gamma ray telescopes built consisted of stacks of eight Cherenkov plastics, each with a 1/4 in. thick BaF_2 converter with an area of 4"x4".(Figure II-6(a)) The BaF_2 crystal gives good time resolution (~ 400ps), adequate light output, and its relatively high atomic number Z provides high pair conversion probability as described in the next section.

In order to collect the light from the crystal, the BaF_2 crystal was enclosed in a light tight box made of thin aluminum, painted in the inside with high reflectivity white paint(titanium dioxide) to achieve good light collection. Two 1.5" diameter photomultiplier tubes were mounted on the top and bottom of the box to collect the light.

All eight elements of the two telescopes have the same active area of 9"x9", The thickness of the first element of the stack is 0.5", the second 1", and all the rest are 2". The Cherenkov counters are connected by tapered light guides to 2" diameter phototubes (Hammamatsu R329) positioned on top and bottom of each element. The phototubes of adjacent elements are staggered so that the detector elements are in contact, leaving only a very small air gap between them. The Cherenkov counter and the light guides are made in one piece using Bicron BC-480 Cherenkov plastic, which is Lucite with waveshifter additive added. Each plastic element is polished carefully to obtain maximum internal reflection of the Cherenkov light.

The third telescope (Figure II-6(b)) uses the same BaF_2 converter as the first two. But instead of eight elements in the stack, there are thirteen 1" thick elements in the stack, which makes its total thickness comparable to that of the other two. The area of the elements, made of Bicron BC-480 Cherenkov plastic, ranges from 6"x6" in the front element to 10"x10" in the back. The tapered light guides are made of ordinary Lucite, then attached to the Cherenkov plastic using optical glue. The same 2" phototubes are used, and they are again staggered to eliminate gaps between elements.

To reduce the rate of cosmic ray muons, a major background in these experiments, the telescope is surrounded by anticoincidence shields on the

front, top and two sides. The anticoincidence shields used on the sides and top are 1/2" thick scintillator paddles, each connected by a tapered lightguide to a photomultiplier tube. The front anticoincidence shield is made of 1" thick Cherenkov plastic BC-480 to avoid being overwhelmed by the high flux of low energy charged particles. But because Cherenkov plastic has a relatively lower light output than scintillators, two photo multiplier tubes are used on the front shield to ensure adequate light collection. The combination of these shields reduces the muon background rate to about 2% of the unshielded rate.

The front anticoincidence shield also acts as a charged particle veto to eliminate fast charged particles such as fast protons and electrons. Neutron discrimination was done using the time-of-flight measurement. More detailed information on background elimination will be discussed in chapter III.

The detectors, including their muon shields, were assembled on a cart, and could be moved easily during the experiments. This enabled us to cover all the angles with our limited number of Cherenkov telescopes. It also allowed cross-checking of the response of all three detectors by placing different detectors at the same position during successive runs.

B.2. Photon Pair Conversion Coefficient

In the initial design of the detector and during the first experiment, the light output from the BaF_2 converter was not added to the total light output, i.e. the energy loss of the electron-positron pair in the converter was not taken into account. Thus, the choice for the thickness of the converter was a result of the compromise between high conversion efficiency

and low energy loss. (The energy lost in the converter was taken into account in all later experiments including those presented in this thesis)

The conversion efficiency of the BaF_2 crystal is photon energy dependent. The efficiency was calculated from the pair production cross section [Mo 69]:

$$\text{Efficiency} = t\,\rho_n[\sigma_e(Z_{Ba}+2Z_F)+(\sigma_{Ba}+\sigma_F)] \qquad \text{(II-1)}$$

where t is the thickness of the converter

Z_F and Z_{Ba} are the atomic numbers of F and Ba

ρ_n is the number density of the BaF_2 molecules within the crystal.

$\sigma_e = 3.11\sigma_o\log(2E_\gamma/m_ec^2)-11.3 = 3.11\sigma_o\log(2k)-11.3$

$\sigma_{Ba} = Z_{Ba}^2 3.11\sigma_o\log(2k)-8.047$

$\sigma_F = Z_B^2\ 3.11\sigma_o\log(2k)-8.047$

where k is the Boltzman constant

The thickness of all our converters are 0.25" (0.635 cm). The curve of the BaF_2 crystal conversion efficiency as a function of the photon energy is plotted in Figure II-7. For the photon energies we are interested in, it ranges from about 10% for photons having energies 20 MeV to over 20% for photons of 100 MeV.

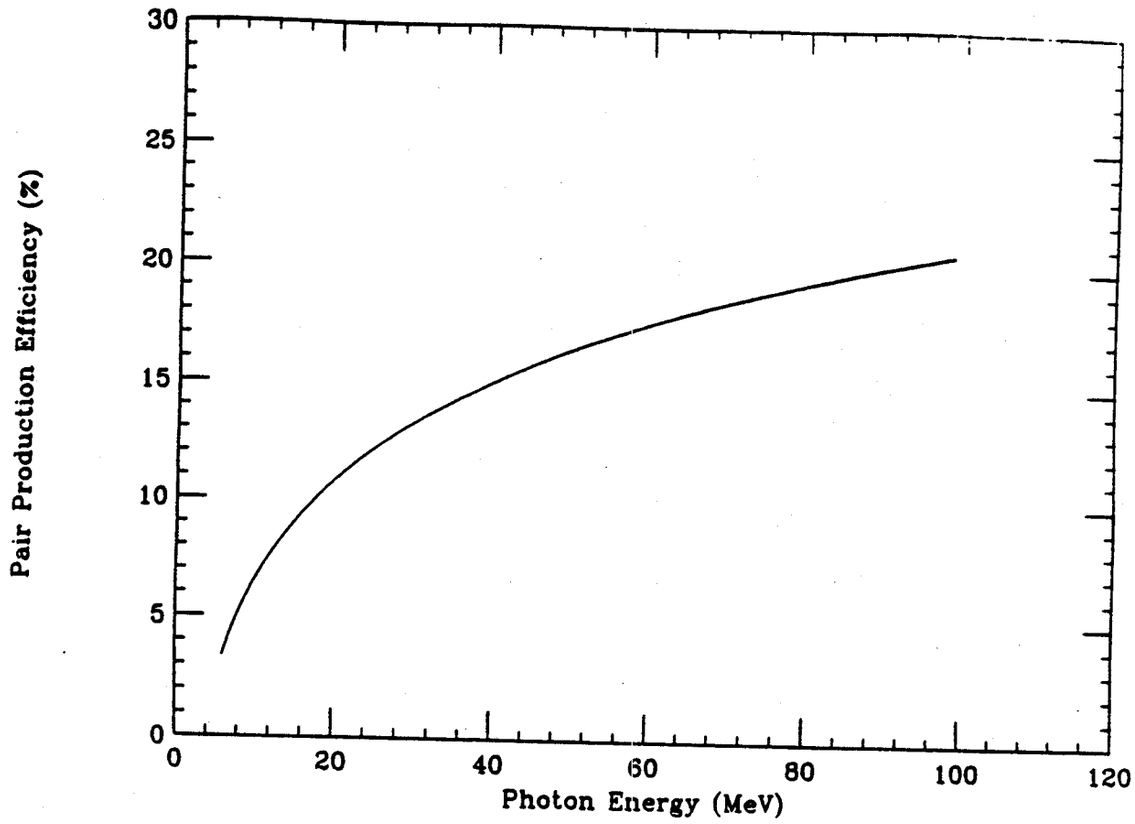

Figure II-7 Pair conversion efficiency of the BaF_2 converter as a function of photon energy.

B.3. Determination of the Photon Energy

B.3.1. Cherenkov Light Output Level

Each member of the e^+e^- pair can have a kinetic energy ranging from 0 $E_\gamma - 2m_e c^2$. The electron and positron dissipate their energy mostly through ionization and radiation as they travel through the detector and eventually stop in different depths of the Cherenkov stack (Figure II-8). Figure II-9 shows the range vs. energy relationship for electrons in the plastic. If we can determine the position where each member of the pair eventually stops, we then know its range and its kinetic energy. And by summing up the energy of the electron and the positron, we can obtain the energy of the original photon.

The Cherenkov light generated by a relativistic electron (or positron) is roughly proportional to the distance the particle traveled within the medium. The Cherenkov light output is only about 1% of the typical light output from a NaI scintillator. The number of photons in the visible range generated by a particle of speed β in unit path length of a medium having an index of refraction n is given [Pa 86] by:

$$N = \frac{\alpha}{c} \int [1 - \frac{1}{\beta^2 n^2}]\, 2\pi d\nu \approx 500 \sin^2\theta_c / cm \qquad \text{(II-2)}$$

where $\theta_c = \cos^{-1}[\frac{1}{\beta n}]$ is the half angle of the Cherenkov cone.

For singly charged particles, the Cherenkov light output level does not depend on the type of particle passing through the medium. We use the level of light output in each element produced by cosmic muons that pass through the entire Cherenkov stack from front to back to be the characteristic light

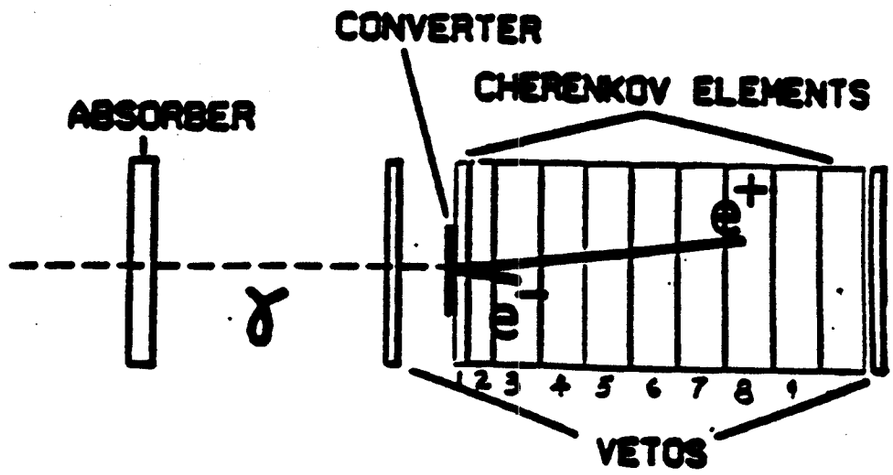

Figure II-8 Principle of operation for the Cherenkov plastic telescope.

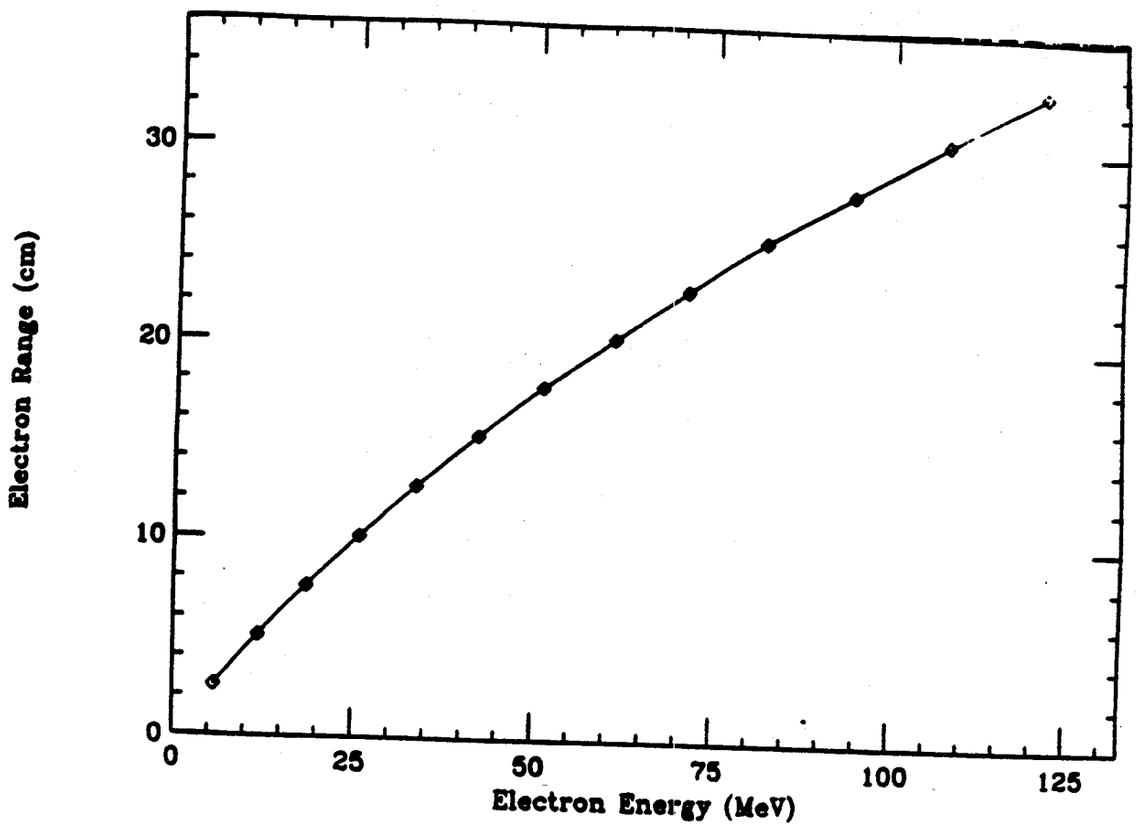

Figure II-9 Electron energy-range relationship in Lucite.

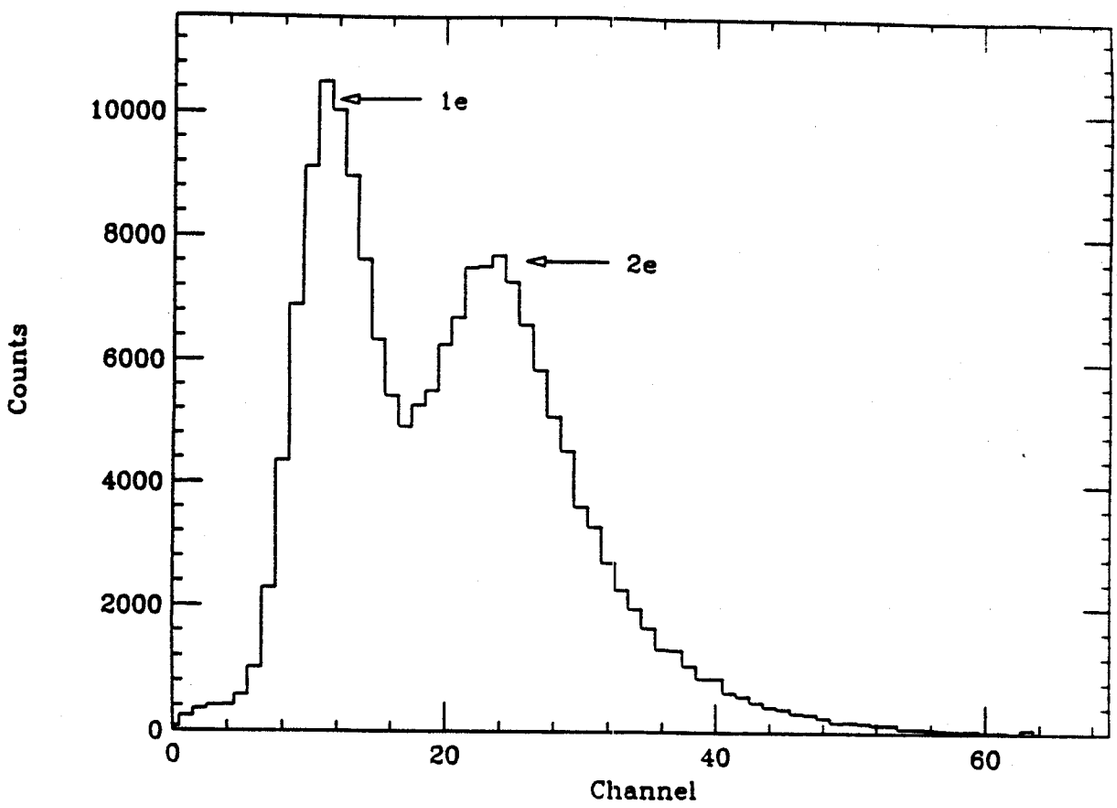

Figure II-10 Typical light output from one element (1" thick) of the Cherenkov stack.

output level of a single minimum ionizing particle passing through the stack. This calibrates the gain of the photomultiplier tubes for each element of the stack for different experiments and for comparison with the tagged photon calibration run. Figure II-10 is a typical histogram of the light output from one of the Cherenkov elements in the stack. Two peaks are seen, corresponding to either one or both members of the e^+e^- pair passing through that element.

Using formula II-2, we estimate the number of photons produced in unit thickness of Cherenkov plastic to be approximately 278 photons/cm. The efficiency of the photomultiplier cathode is about 25%. And the typical light collection efficiency of the scintillator is around 10%. Therefore, there are only about N ~ 278 x 25% x 10% ~ 7 photons/cm collected in the photomultiplier tubes for each electron. The small number of photons collected makes it difficult to determine accurately the location where each electron and positron stops in order to obtain their energy. Several different algorithms were tried to determine the photon energy using the electron range method without success. So, in the experiment, the method of position weighted sum of the total light output of each element was used to calculate the total energy carried by each e^+e^- pair.

B.3.2. Position Weighted Sum of Light Outputs

For electrons and positrons moving at relativistic speed, the Cherenkov light output is roughly proportional to the distance traversed. If the energy lost by an electron within the Cherenkov plastic were also proportional to that distance, the total energy of the pair would simply be the sum of the total light output from all the Cherenkov elements. However,

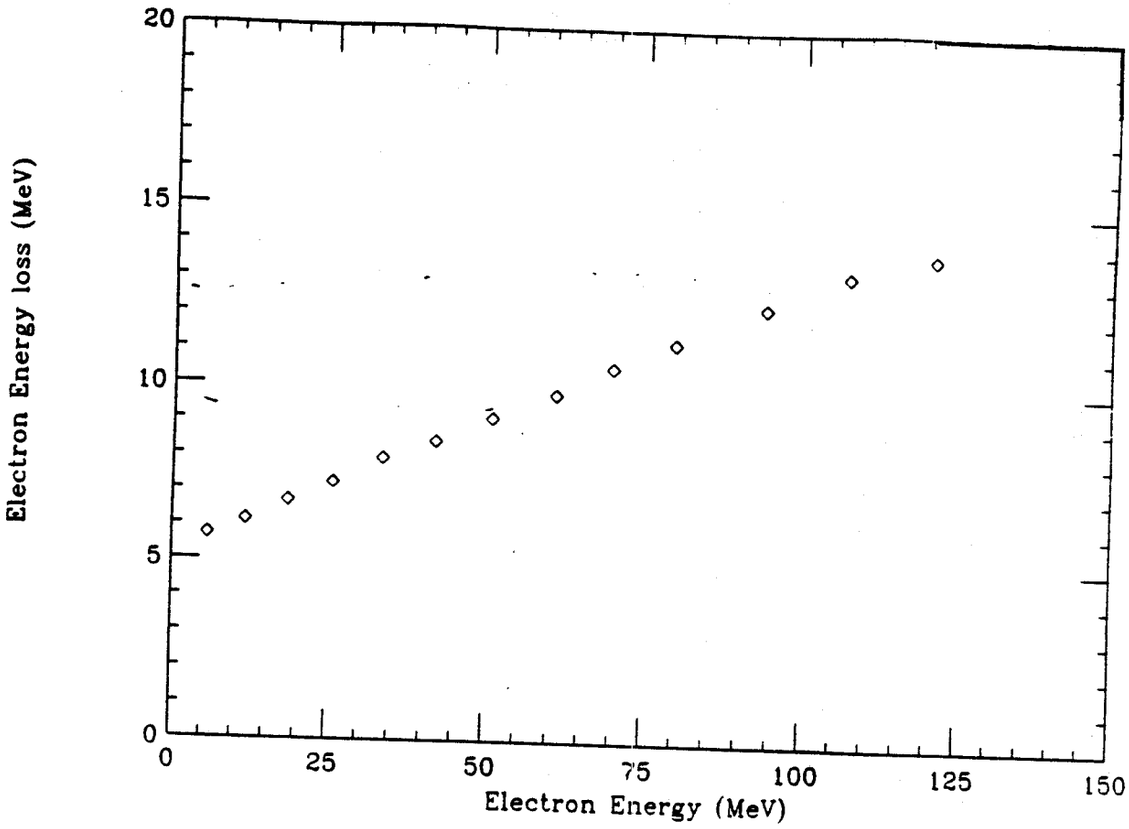

Figure II-11 Electron energy loss in 1" thick Cherenkov plastic as a function of energy.

the energy lost by an electron in the plastic does depend on the energy of the electron. A higher energy electron loses more energy per unit distance traveled than an electron of lower energy. Figure II-11 shows the energy losses of electrons of different energies when passing through a 1" thick Lucite (Cherenkov plastic). A 100 MeV electron, for example, loses about 12.4 MeV in passing through 1" of Cherenkov plastic, while an electron of 55 MeV loses about 9 MeV in traversing the same length. Therefore, a simple unweighted sum of the light output from each element of the stack would not yield the correct energy of the electron-positron pair. We tried the unweighted sum scheme and found it did not work as well as the weighted sum scheme.

In order to take into account the nonlinearity of the electron energy loss in the stack, we plot in Figure II-12 the electron energy loss as a function of the range of the electron. This range vs. energy loss relationship is used to determine the proper weight for the different elements of the Cherenkov stack. The weight assignment of the individual elements are tabulated in table II-1 (for detector 1 and 2) and II-2 (detector 3).

In the first column of the tables, the individual element of each Cherenkov stack are numbered from the front (right after the BaF_2 converter) to the back (see Figure II-8 for example of the numbering scheme). In the 2nd column, the thickness of the corresponding element (in cm) is listed. In column 3, we list the distance d from the back of that element to the front of the stack (behind the BaF_2 converter). Note that if an electron stops at the back edge of this element, we then know that the electron has a range equal to the distance d. And by making use of the electron range-energy

Table II-1 Electron energy loss in elements of detector 1 and 2.

Element #	Thickness (cm)	Distance to Convertor (cm)	Electron Energy (MeV)	ΔE (MeV)
1	1.27	1.27	2.89	2.89
2	2.54	3.81	8.67	5.78
3	5.08	8.09	22.02	13.35
4	5.08	13.17	37.62	15.60
5	5.08	18.25	55.70	18.08
6	5.08	23.32	76.78	20.98
7	5.08	28.40	100.9	24.22
8	5.08	33.48	129.0	28.15

Table II-2 Electron energy loss in elements of detector 3.

Element #	Thickness (cm)	Distance to Convertor (cm)	Electron Energy (MeV)	ΔE (MeV)
1	2.54	2.54	5.72	5.72
2	2.54	5.08	11.84	6.13
3	2.54	7.62	18.50	6.68
4	2.54	10.16	25.70	7.20
5	2.54	12.70	33.60	7.89
6	2.54	15.24	41.98	8.38
7	2.54	17.78	51.0	9.05
8	2.54	20.32	60.75	9.75
9	2.54	22.86	71.2	10.23
10	2.54	25.40	82.0	11.04
11	2.54	27.94	94.28	12.28
12	2.54	30.48	107.5	13.20
13	2.54	33.02	121.3	13.75

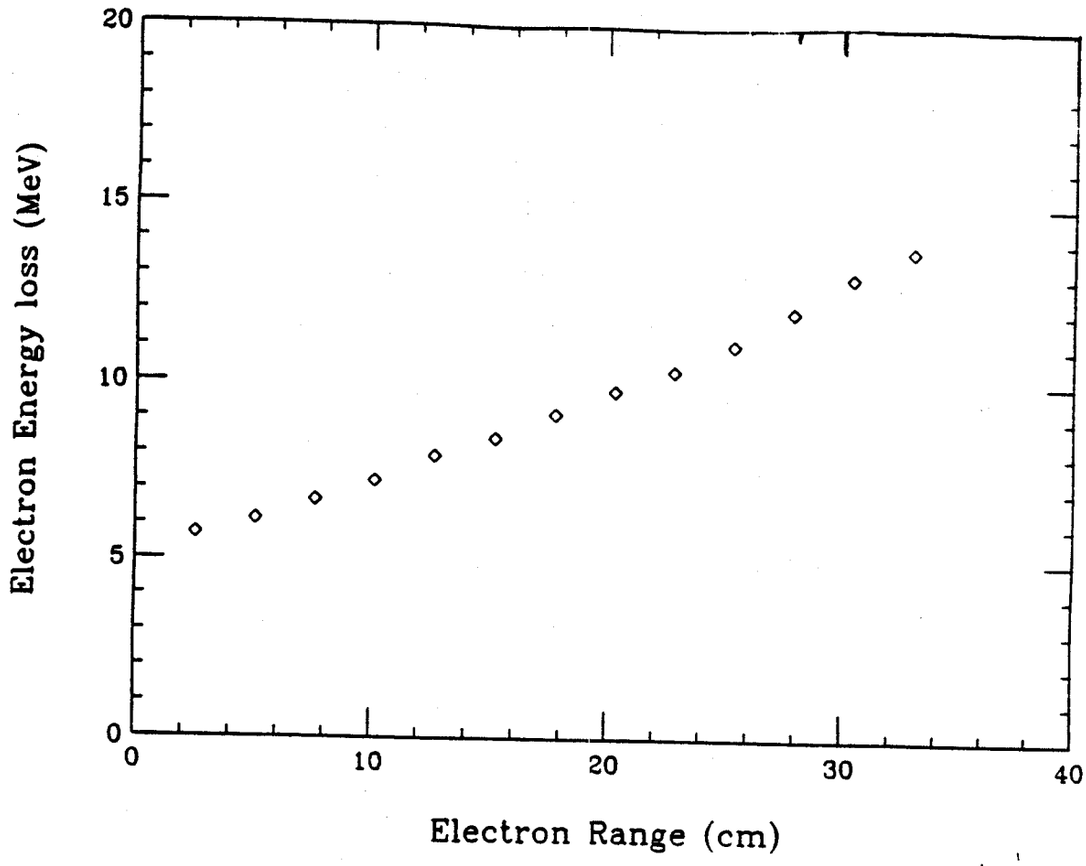

Figure II-12 Electron energy loss in 1" thick Cherenkov plastic vs. the range of the incident electron.

relationship (Figure II-9), we can then obtain the energy of the electron, which we put in column 4. In column 5, ΔE is obtained by subtracting the energy of an electron having a range of d_n by the energy of an electron of range d_{n-1}. This additional energy ΔE required for an electron to go pass element n-1 and reach the far edge of element n is the weight we assign to element n.

Following is an example of how the energy of the photon is determined utilizing the tables: suppose a 98.7 MeV photon was converted into an electron of 76.68 MeV and a positron of 22.02 MeV in telescope #1. The 76.68 MeV electron will have a range of 23.32 cm and will stop at the back of Cherenkov element #6. In the ideal case where there is no statistical fluctuation, this electron produces one unit of light output in elements #1 through #6. Therefore, the energy of this electron can be obtained by summing the ΔEs (column 6, table II-1) from elements 1 through 6:

$$E_e = 2.89+5.78+13.35+15.60+18.08+20.98$$
$$= 76.68 \text{ MeV}$$

The 22.02 MeV positron has a range of 8.09 cm and stops at element #3. It will produce one unit of light in element #1 through #3. So, the energy of the positron can then be obtained by summing the ΔEs from elements 1 through 3:

$$E_p = 2.89+5.78+13.35$$
$$= 22.02 \text{ MeV}$$

Therefore, the energy of the original photon is:

$$E_\gamma = E_e + E_p$$
$$= [(2.89+5.78+13.35+15.60+18.08+20.98)+(2.89+5.78+13.35)]$$
$$= [2 \times (2.89+5.78+13.35) + 1 \times (15.6+18.08+20.98)]$$
$$= 98.70 \text{ MeV}$$

This algorithm can also be understood the following way: since the electron and the positron both pass through elements #1 through #3, the pair produces two units of Cherenkov light in elements #1 through #3. But only the electron travels through element #4 through #6, it produces one unit of light in elements 4, 5, and 6. In another words, the energy of the photon can be determined from the sum of the light outputs from all the elements L_i, (in units of the characteristic light output of one electron passing through the same thickness LO_i) multiplied by the proper weight ΔE of the corresponding elements. That is:

$$E_\gamma = \Sigma_i \left(\frac{L}{LO}\right)_i \Delta E_i \Big|_{i=\#\text{ of elements}} \qquad \text{(II-3)}$$

As illustrated in the above example, we obtain the correct energy of the photon using this algorithm.

However, due to the small number of Cherenkov photons produced, there is a large statistical fluctuation of the light output level L in each element. The telescope was found to have only moderate energy resolution, i.e. ranging from about 10% FWHM at 20 MeV to 20% at 80 MeV.

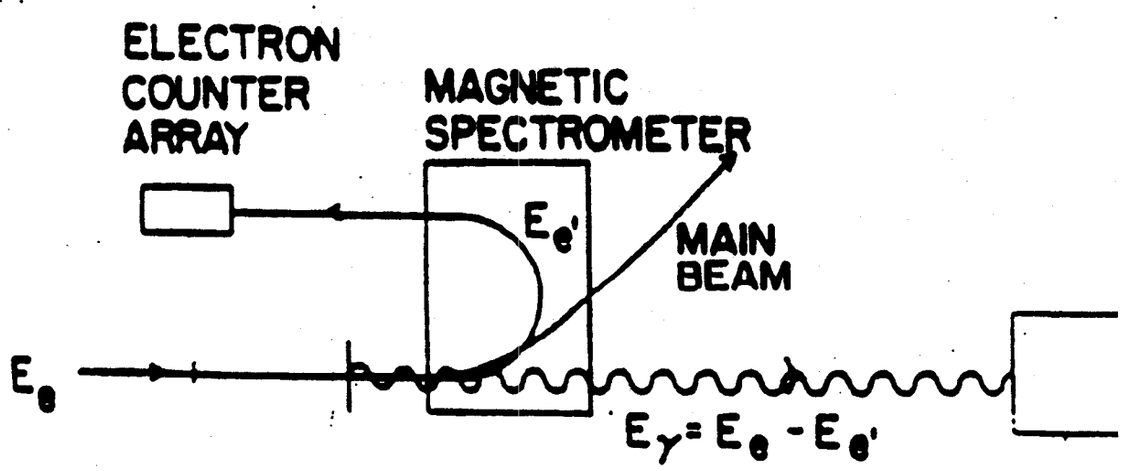

Figure II-13 Schematic set-up of the University of Illinois tagged photon facility.

C. Calibration of the Cherenkov Plastic Telescope Detector

The calibration of the Cherenkov plastic telescope was done at the tagged photon facility at the University of Illinois. The schematic setup of the facility is shown in Figure II-13. Bremsstrahlung photons were produced by electron beams bombarding a thin 25 μm aluminium foil. The primary electron beam that did not interact in the foil was bent into a beam dump. Electrons which interacted in the foil and generated bremsstrahlung photons were bent through 180° and detected in a 32 element scintillator counter array. The detector energy was determined by the position of the scintillator counter. By requiring a coincidence between the the photon detector and the electron counter, we then know the energy of the "tagged" bremsstrahlung photon by energy conservation. Four electron beam of energies 99, 77, 56 and 35 MeV were used, providing tagged photons ranging in energy from 74 to 82 MeV, 53 to 61 MeV, 37 to 43 MeV, and 17 to 23 MeV respectively. One of the eight-element Cherenkov telescopes was taken to the calibration site.

C.1. Calibration of the Detector Efficiency

The absolute efficiency of the Cherenkov telescope was obtained by comparing the efficiency of our detector relative to a large NaI detector provided by the University of Illinois. The NaI crystal, 30 cm diameter and 36 cm deep, was assumed to be close to 100% efficient when illuminated by a collimated beam to the center.

We define R as the ratio of the number of photon detector-tagged electron counter coincidences to the number of times the tagged electron

counter fired. The ratio R is also the product of the detector efficiency ε_{det} and the efficiency of the magnetic spectrometer ε_{spec}

$$R = \frac{N_{\gamma-e}}{N_e} = \varepsilon_{det}\varepsilon_{spec}$$

By measuring the ratio R for both the NaI and the Cherenkov telescope under identical geometrical configuration, it is possible to determine the efficiency of the Cherenkov telescope relative to the large NaI detector.

$$\frac{\varepsilon_{Cherenkov}}{\varepsilon_{NaI}} = \frac{R_{Cherenkov}}{R_{NaI}}$$

The magnetic spectrometer efficiency ε_{spec} was found to be dependent on the energy of the electron beam, varying from about 30% for the 35 MeV beam to 60% for the 99 MeV beam. Therefore, it was necessary to measure R for each beam energy. Since the efficiency of the large NaI detector were assumed to be 100% efficient, the relative efficiency we obtained were then assumed to be the absolute efficiency. Figure II-14 shows the efficiency of the Cherenkov telescope as a function of the photon energy. The efficiency varies from about 10% for 20 MeV photons to about 20% for photons of 80 MeV. The error bar on the data reflects mainly the uncertainty in the efficiency of the tagged electron counter. Also shown for comparison are the calculated efficiency from pair production discussed in section B.2. (formula II-1), and a calculation using the Stanford electron-photon shower code EGS4 [Ne 85]. The two calculations are in agreement with the measurement within the uncertainty.

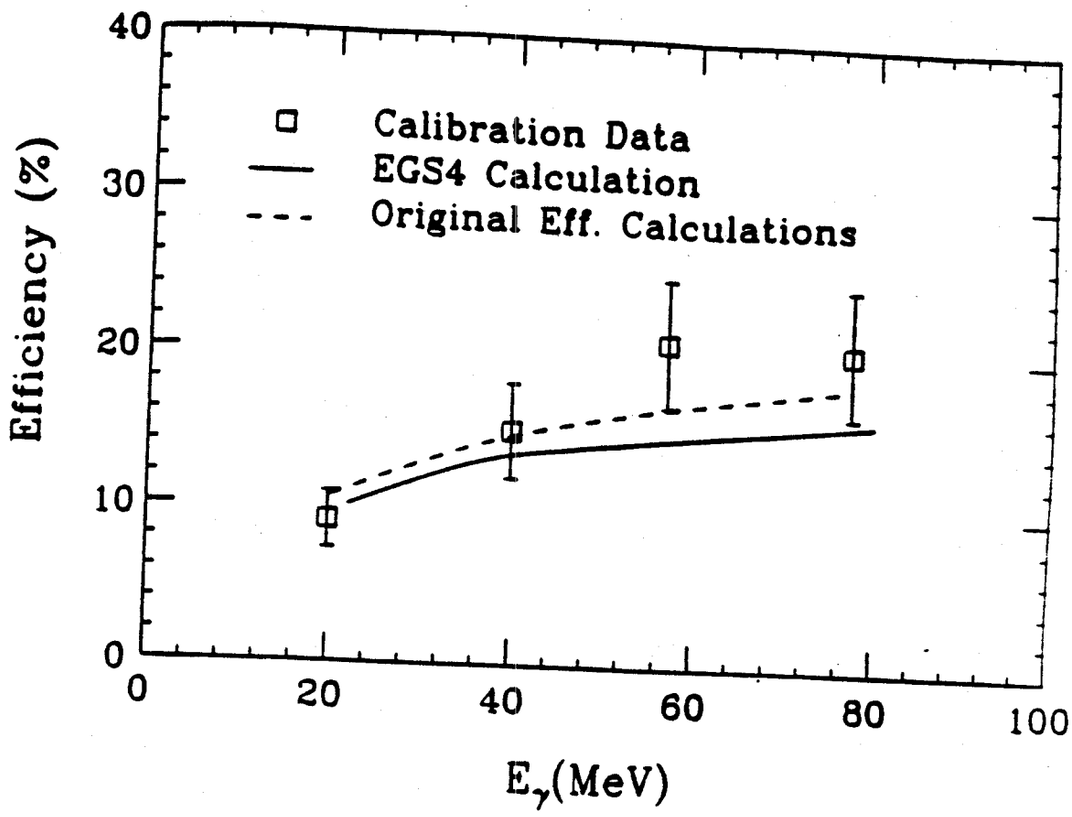

Figure II-14 Efficiency of the Cherenkov telescope as a function of photon energy.

C.2. Calibration of the Energy Response of the Detector

By energy conservation, the energy of the photon plus the energy of the secondary electron reaching the electron counter array equals the energy of the incident electron. By requiring a coincidence between the firing of the photon detector and the electron counter, we can then know the energy of the "tagged" bremsstrahlung photon. Each element of the 32 scintillator has a momentum bite of about 1.25%. This corresponds to a energy span of approximately 0.2 MeV at 20 MeV. The response of the photon detector was measured by taking photons corresponding to the firing of 10 adjacent tagged electron counters, which corresponds to a energy span of about 2 MeV.

The response of the Cherenkov gamma ray telescope for the 22, 42, 60 and 80 MeV tagged photons is shown in Figure II-15. The energies corresponding to the peak location of the response functions are found to be systematically lower than the known tagged photon energies E_γ by about 7 MeV. Figure II-16 shows the peak energy of the detector response function vs. the energy of the tagged photons. The dashed line represents the correct response. The response of the gamma ray telescope lies approximately 7 MeV below the dashed line.

Before the calibration, only the light outputs from the elements of the Cherenkov plastic stack were summed to obtain the photon energy, the energy loss of the e^+e^- pair within the BaF_2 converter were not taken into account. This neglect of the energy loss of the pair within the converter was found to be responsible for the systematic shift of the peak energy in the telescope response function.

To include the light output from the converter in the sum, the photon energy is now calculated using a modified formula II-3:

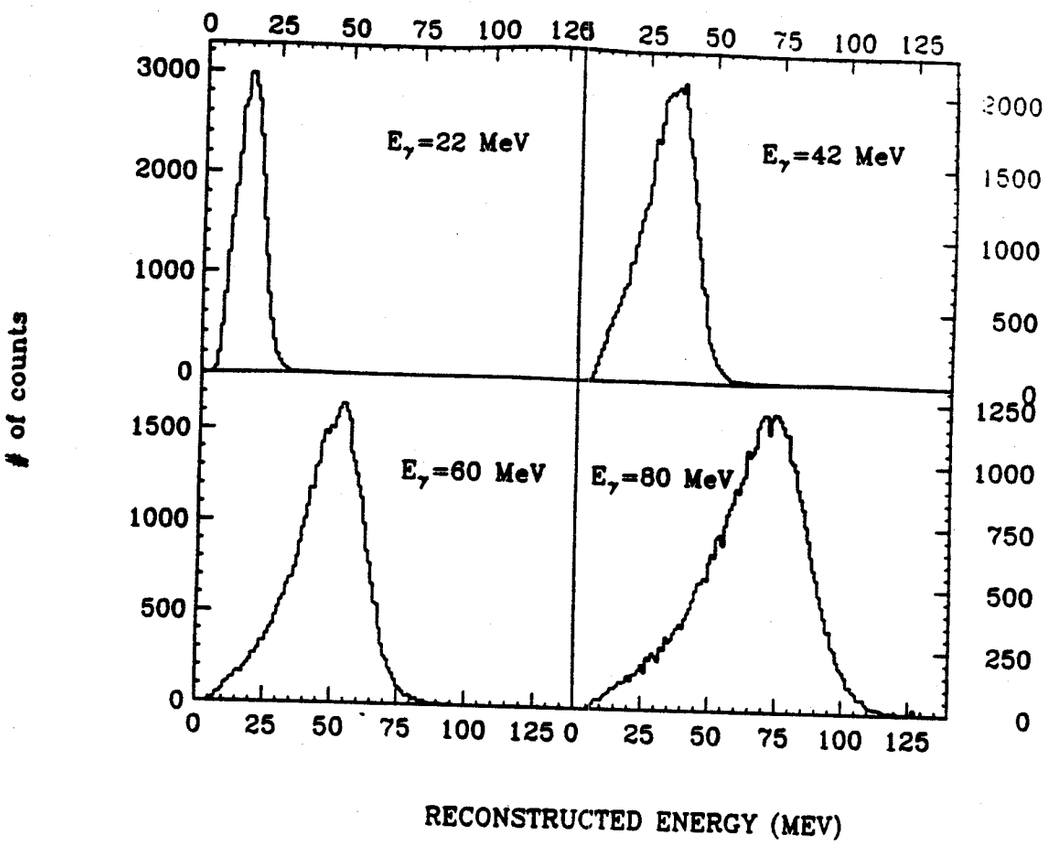

Figure II-15 Response function of the Cherenkov telescope at 22, 42, 60, and 80 MeV without including light output from the BaF_2 converter.

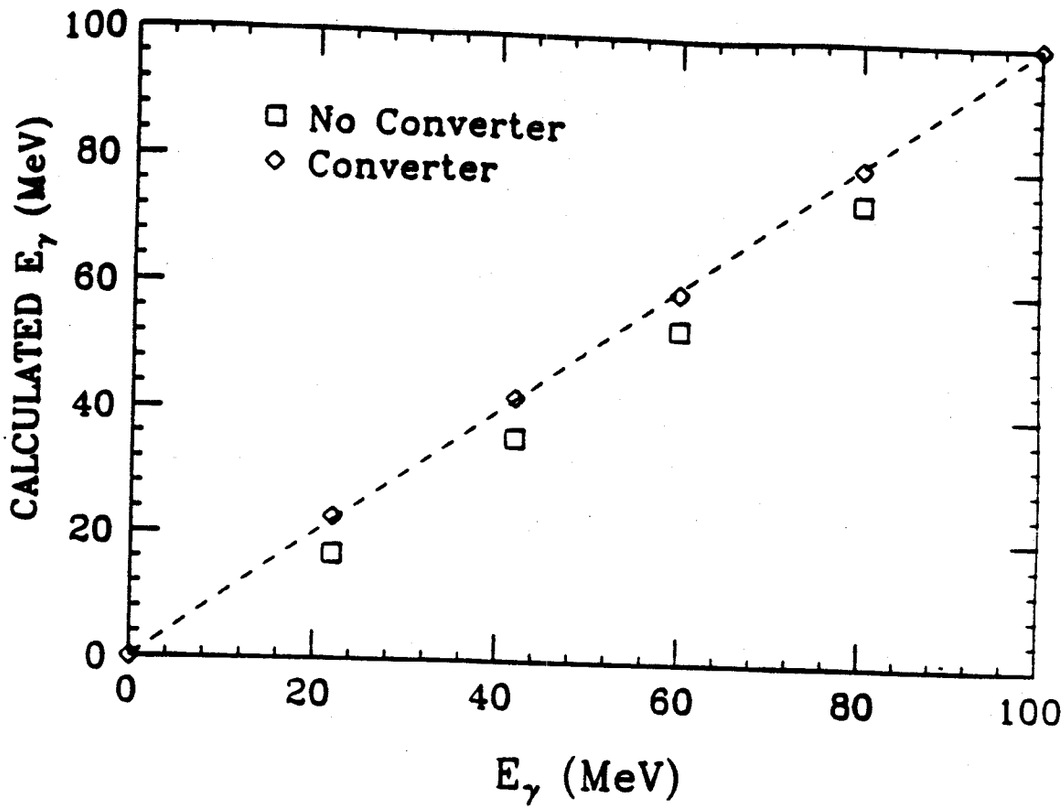

Figure II-16 Energies of the peak of the response function vs. energies of the tagged photon.

$$E_\gamma = \Sigma_i \left(\frac{L}{L0}\right)_i \Delta E_i \Big|_{i=\#\text{ of elements}}$$

Here the total number of elements is n+1 in order to take into account the energy losses of the electron and positron in the converter. The peak energies of the new response functions that include the light output from the converter are also plotted in Figure II-16 (diamonds). We found the peak energies of the new response function now lies on the correct response line.

In Figure II-17, the new response functions that include the converter light outputs are plotted (solid line histograms) in comparison with the response function without the converter light outputs (dashed lines). We found that including the converter light output not only shifted the peak of the response function to correct energy, it also improves the energy resolution of the detector at lower energy. We plotted, in Figure II-18, the full width at half maximum of the response functions of the Cherenkov plastic telescope using the two different algorithm, for all four energies. The improvement at lower gamma ray energy are considerable.

D. Comparison with Other Detectors

In Figure II-19, we compare the response function of our Cherenkov telescope with that of the NaI telescope used by the Bertholet et. al. We can see that scintillator type detector has a better resolution at higher energy ($E_\gamma \geq 80$). We also plotted the FWHM of the MSU Cherenkov telescope in comparison with that of the other type of detectors in Figure II-20. At energies below 60 MeV, the resolution of the lead glass detector are much

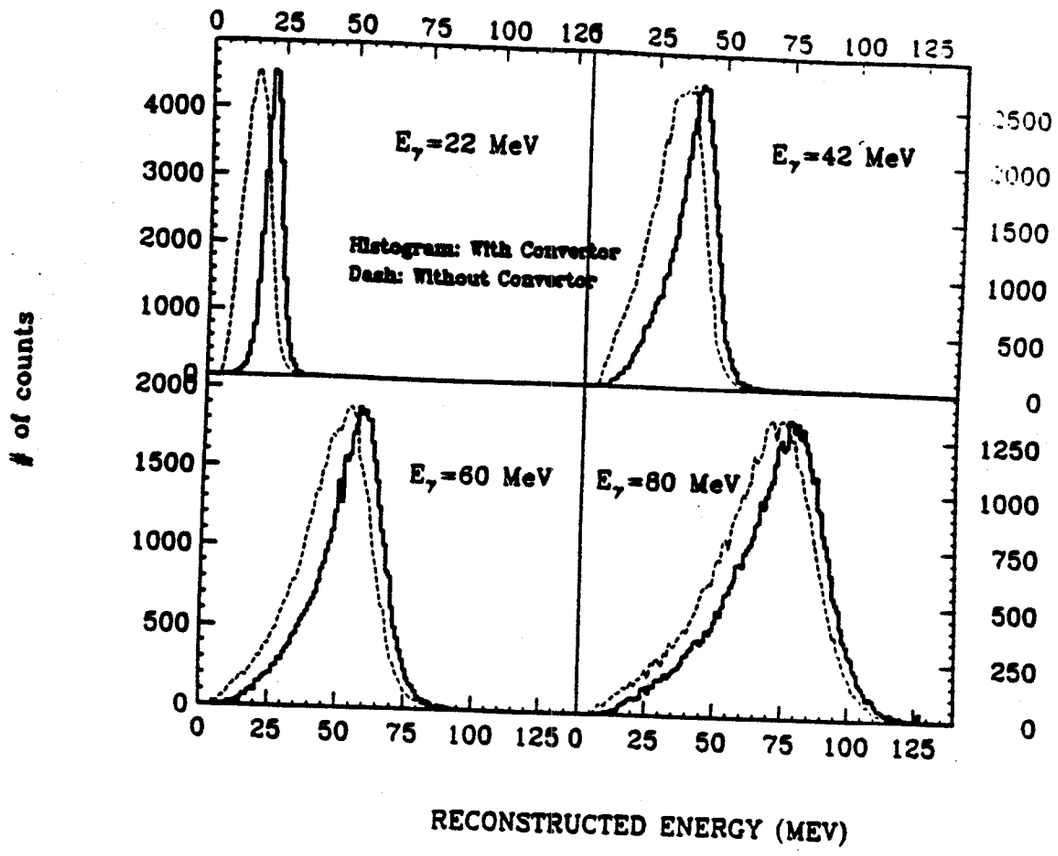

Figure II-17 Response function of the Cherenkov telescope with the light output from the converter taken into account.

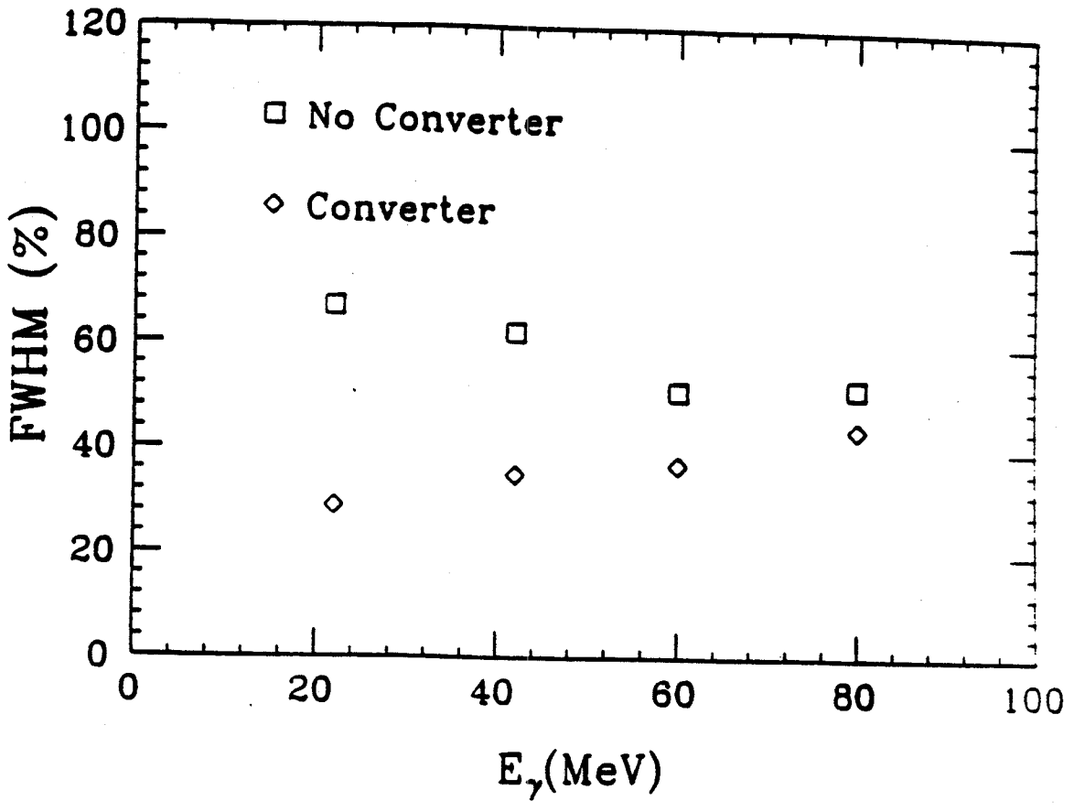

Figure II-18 FWHM of the response functions of the Cherenkov telescope with and without taking into account the converter light output.

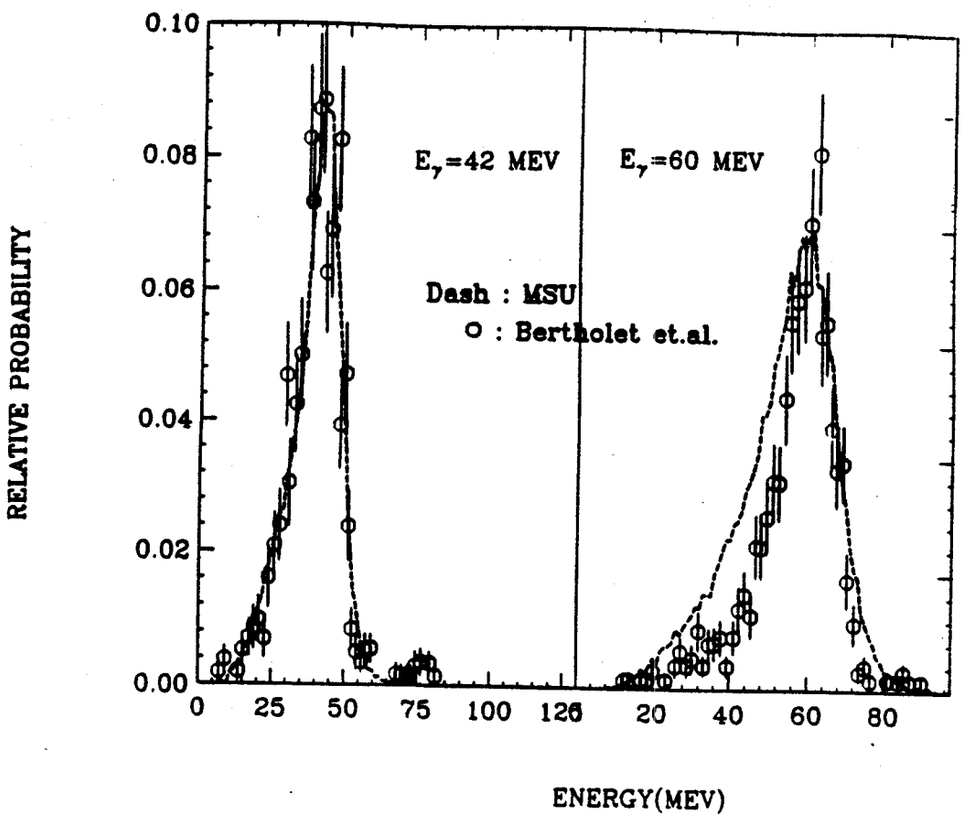

Figure II-19 Response functions of the Grenoble NaI telescope in comparison with the MSU Cherenkov telescope [Be 87].

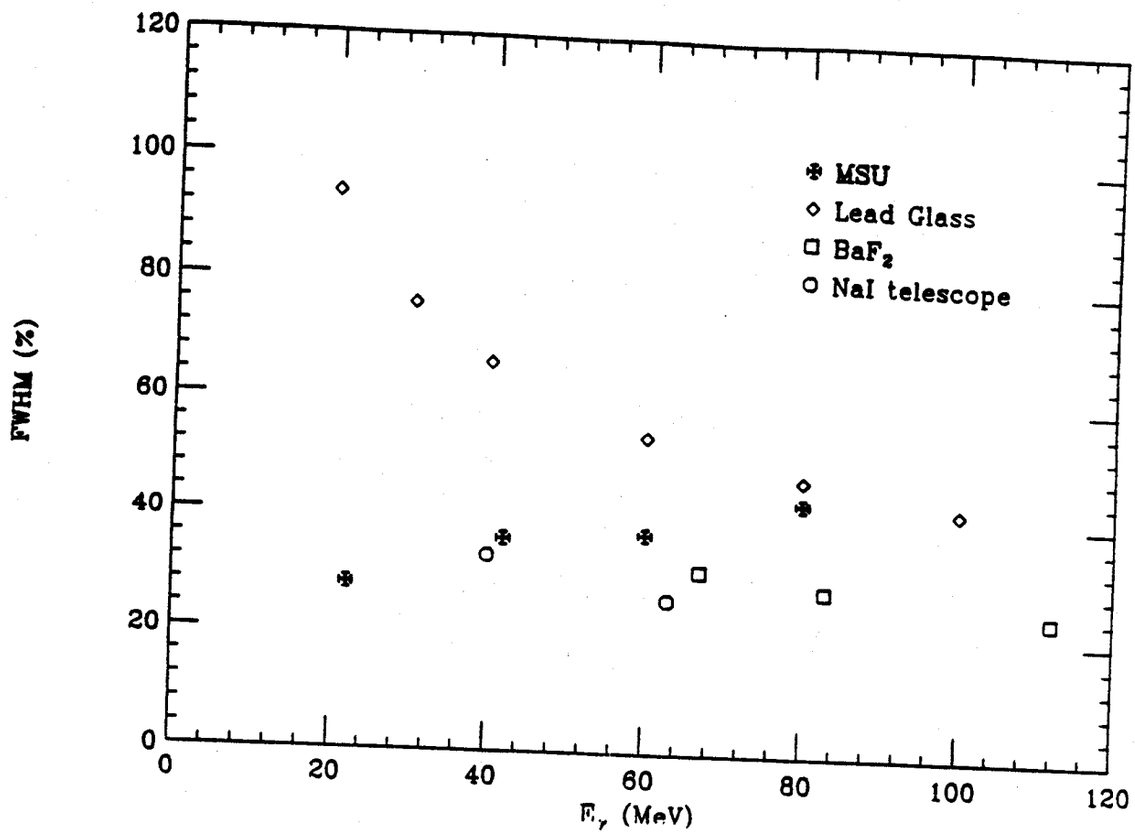

Figure II-20 The FWHM of different type of detectors used in high energy photon measurements.

worse than all the other types of detector, while the resolution of the scintillator detectors and the Cherenkov telescope are comparable.

E. Summary

Many different detectors have been used to measure the bremsstrahlung photon production cross section in intermediate energy heavy ion reactions. The majority of these detectors are shower type detectors such as NaI, BaF_2 or lead glass. We have designed and built three non-shower type gamma ray detectors based on the Cherenkov process.

The original concept of the Cherenkov telescope was to first convert photons into e^+e^- pairs in the BaF_2 converter. Then by determining the range of the electron and positron, the energies of the e^+e^- pair would be determined, so would the energy of the original photon. However, due to the small number of photons produced, the statistical fluctuations made the reliable determination of the electron and positron range impossible. Different algorithm were then tried, and the position weighted sum of the light outputs from all the elements of the stack was adopted to calculate the energy of the photon.

The Cherenkov telescope was calibrated in the tagged photon facility in the University of Illinois. The absolute efficiency of the telescope was found to range from roughly 10% for photons of 20 MeV to about 20% at 80 MeV. This is consistent with calculations both from pair production cross section and from the Stanford electron-photon shower code EGS4.

The energy response of the telescope was first found to have a systematic shift towards lower energy. The cause was due to the neglect of the energy loss within the converter. When the light output of the converter

was later included in the summation scheme, the peak location of the response functions agree with the known energy of the tagged photons. The inclusion of the converter light output also improves the energy resolution of the telescope considerably at low energy. We found the energy resolution of the Cherenkov telescope worse than scintillator detectors while better than that of the lead glass.

CHAPTER 3

EXPERIMENTAL SET-UPS AND DATA REDUCTION

A. Experimental Set-ups

A.1. Detector Lay-outs

Two high energy gamma ray experiments using the Cherenkov plastic telescopes were carried out at the National Superconducting Cyclotron Lab: 1) the light-ion induced gamma ray production using 25 MeV/nucleon ^{4}He, 53 MeV/nucleon ^{2}H and ^{4}He beams on C, Zn and Pb targets; and 2) the symmetric system experiment using 30 MeV/nucleon ^{7}Li, ^{20}Ne and ^{40}Ar beams on Pb target and targets having similar atomic mass. The experiment layout is shown in Figure III-1. Three telescope detectors were used to cover the angular range from 30° to 150° in 30° intervals. The first detector (D1) covers the more forward angles of 30°, 60° and 90°. The second detector (D2) was used for the backward angles: 90°, 120° and 150°. The third detector (D3) (the 13 element telescope) was positioned on the other side of the beamline covering angles of 60°, 90° and 120° (Figure III-1). This set-up enables extensive cross-checking of the relative efficiency of the three detectors. All detectors are positioned 50 cm from the target. At this distance, each telescope subtends a solid angle of 40 msr. One graphite absorber of 1" thickness was put between the target and each of the detectors to reduce the rate of charged particles, which would otherwise saturate the front anticoincidence shield of the telescopes.

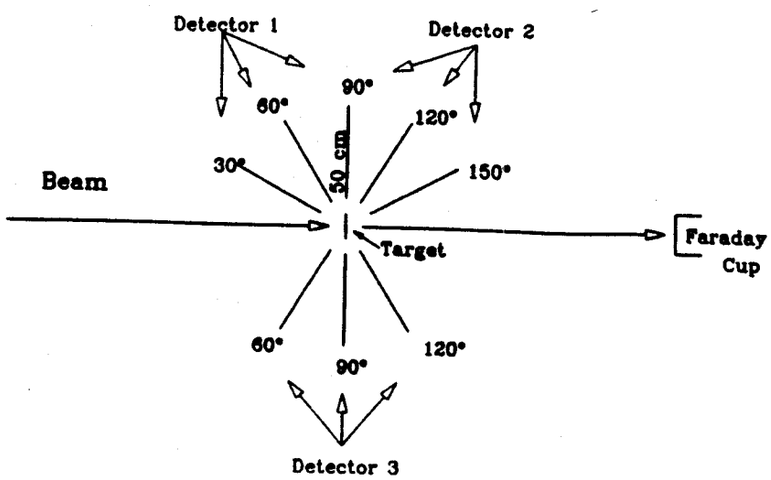

Figure III-1 Layout of the experimental area.

At laboratory angles of 60° and 120°, there are data from two detectors, while at 90°, data from all three detectors are available. This extensive cross-checking of the response of the three detectors indicated the systematic differences in the cross section measurements by the different detectors were less than 10%. Therefore, the average of data from different detectors at same laboratory angle were used to gain better statistics.

A.2. Electronics

Figure III-2 shows the master trigger used in the experiment. A three fold coincidence is required to fire the master trigger: a signal from one the two photomultiplier tubes of the converter, and from the first two elements of the Cherenkov stack. When the the master trigger is fired and the computer "not busy" condition was also satisfied, the pulse height and the time of the pulse from each phototube of all the Cherenkov plastic elements of the stack and the anticoincidence shields of that telescope were then recorded. Figure III-3 shows the general electronic circuitry.

In earlier experiments, all six phototubes (two from the converter, two from the first element and two from the second element of the Cherenkov stack) were required to fire together to trigger an event. But we later found that requiring the coincidence firing of only one of the two phototubes from each of the trigger elements achieves a better compromise between noise rejection and detector efficiency. The minimum photon energy the detectors are able to measure at this configuration are determined by the requirement that at least one member of the electron-positron pair reaches the second Cherenkov element. This corresponds to an energy

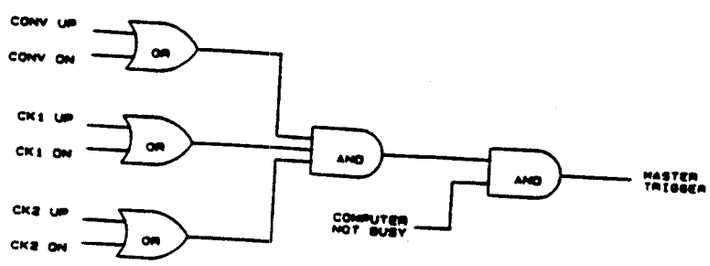

Figure III-2 Electronic schematic of the master trigger logic.

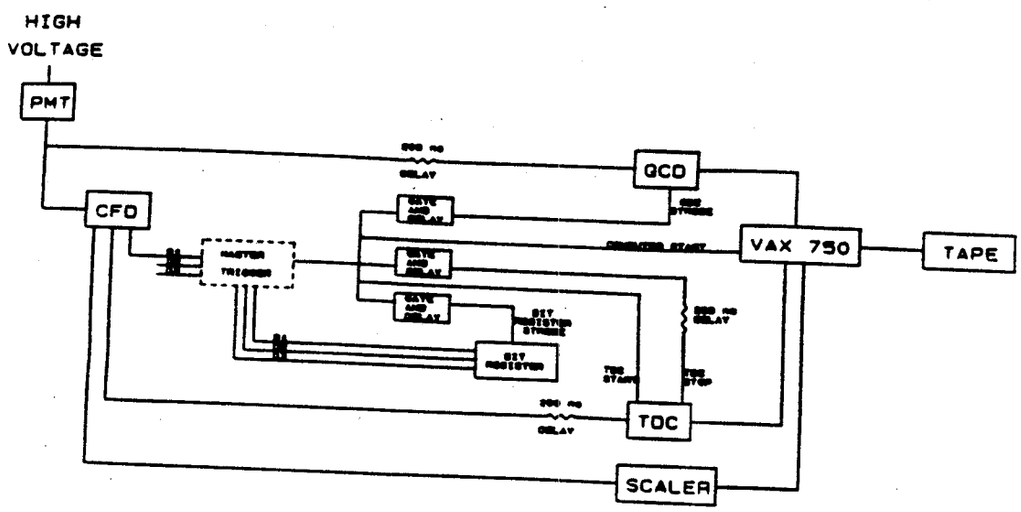

Figure III-3 Electronic schematics of the detectors.

threshold of approximately 10 MeV.

The cyclotron RF timing with respect to the master gate was also recorded. This crucial information was necessary for neutron discrimination.

B. Background Suppression

B.1. Suppression Of Energetic Neutrons

One of the major sources of background in the measurement of high energy gamma ray from intermediate energy nuclear reactions is the large number of energetic neutrons produced in the reaction. Unlike charge particles which can be vetoed by the front anticoincidence shield of the telescope, neutron discrimination was done by the time-of-flight (TOF) method.

The spectrum of the timing of the master gate with respect to the RF signal of the cyclotron is shown in Figure III-4. The slower moving neutrons show up as a "bump" at a later time than the sharp time peak of the gamma rays. By gating on the peak of the fast moving gamma rays, we were able to greatly reduce the background of slower moving neutrons. Figure III-5 shows the comparison of the energy spectra with and without the time-of-flight gate. In addition to a significant reduction of the background neutrons, the TOF gate also eliminates a large fraction of the random events produced by cosmic ray muons which do not have the correct timing with respect to the RF of the cyclotron.

B.2. Suppression of Cosmic Ray Muons

Another important background for high energy gamma ray measurements is cosmic ray muons. The muon rate can be significantly reduced by applying the

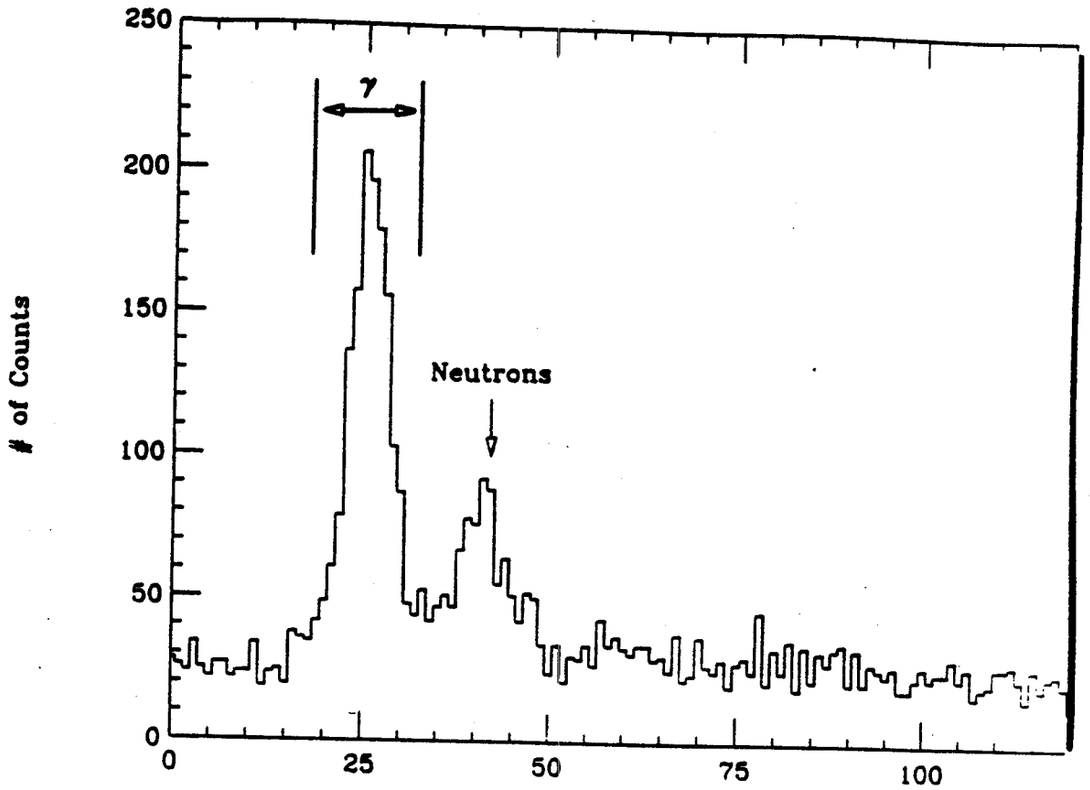

Figure III-4 A typical time spectrum of the gamma rays.

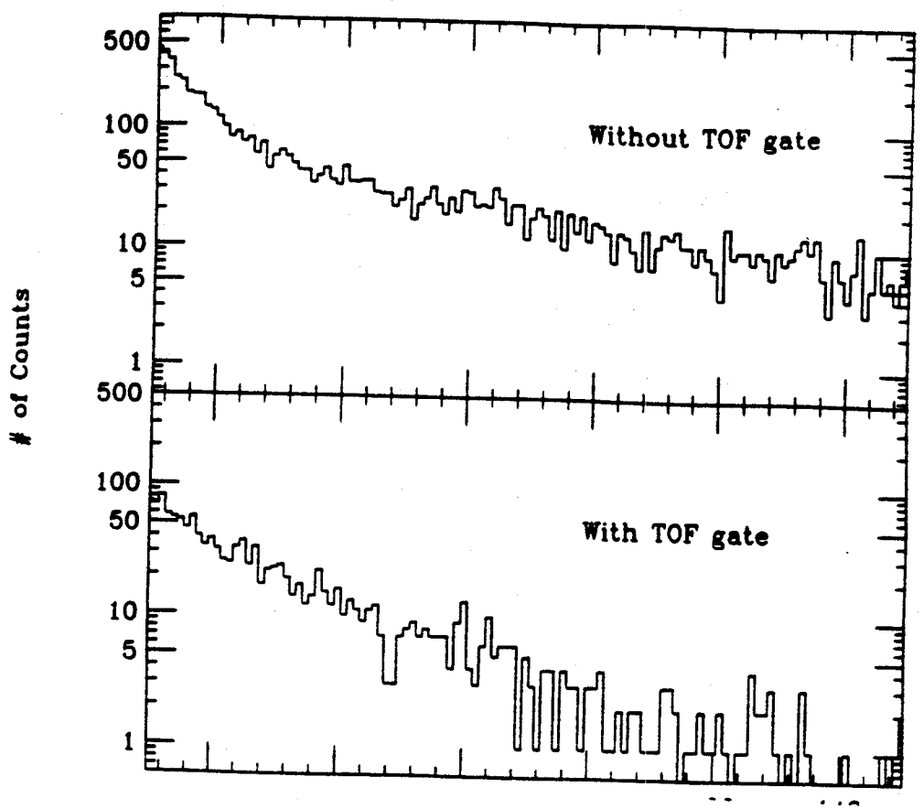

Figure III-5 Comparison of photon spectra with and without TOF gate.

TOF gates. However, because of the very small production cross section of gamma rays at high energy, the cosmic ray muon rate during the "beam on" period can still be significant. Therefore, it is in general necessary to employ the anticoincidence shields. Each detector is surrounded by anticoincidence shields on the front, top and both sides.

The suppression of the cosmic ray muon background was done during off-line analysis. An event is accepted only when no signal was present in any one of the anticoincidence shields. The anticoincidence shields alone were found to be able to reduce the muon background rate to approximately 2% of the unshielded rate. Figure III-5 shows a comparison of the photon energy spectrum with and without the anticoincidence shield. The reduction of muon back ground was most important in the high energy tail of the photon spectrum.

The final photon spectra were then obtained by combining both the anticoincidence conditions and the TOF to eliminate the cosmic ray muons and the fast neutrons.

C. Summary

Three Cherenkov plastic telescopes were used to cover laboratory angles of 30°, 60°, 90°, 120° and 150°. Extensive cross checking on the relative efficiency of the three detectors was done, and the systematic differences were found to be less than 10%. Therefore, data collected with different detectors at the same laboratory angles were averaged to obtain better statistics.

When an electron or positron from the e^+e^- pair passed through the BaF_2 converter and reached the second Cherenkov plastic element, the master gate

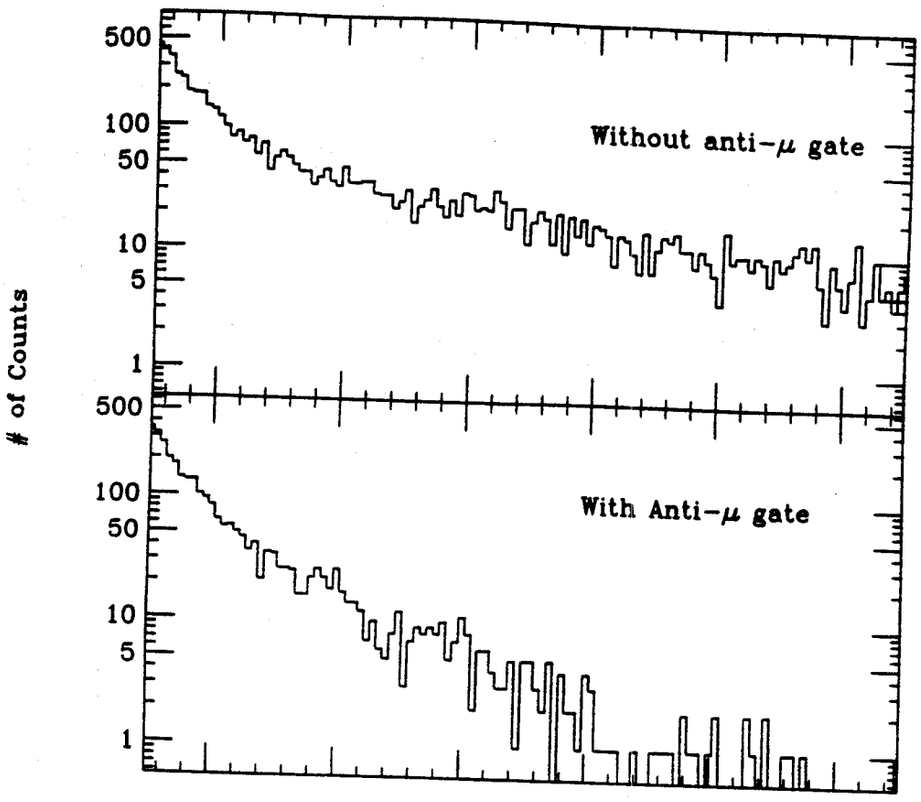

Figure III-6 Comparison of photon spectra with and without anti-μ shields.

was fired. Signals from all the elements of the Cherenkov plastic stack and from the anticoincidence shields of that detector were recorded. The corresponding minimum photon energy is about 10 MeV.

Charge particles from the target area were vetoed by the front Cherenkov plastic anticoincidence shield. The cyclotron RF timing with respect to the master gate was used to discriminate against energetic neutrons. An anticoincidence shield around each telescope was able to reduce cosmic ray muons rate to about 2% of the unshielded rate. The photon energy spectra were obtained by combining the TOF gate and anticoincidence gate to eliminate all the backgrounds.

Chapter 4

HIGH ENERGY GAMMA RAY PRODUCTION FROM LIGHT ION INDUCED REACTIONS

A. Introduction

A.1. History: The Measurements of High Energy Gamma Rays

The production of high energy gamma rays in intermediate energy heavy-ion reactions was discovered in 1984 independently by groups at GSI and MSU. Here at MSU, Beard et al. [Be 85], while studying subthreshold charged pion production, encountered a large background of quite energetic electrons and positrons, which they later attributed to the pair conversion of high energy gamma rays. At about the same time, Grosse et al. [Gr 85] were studying neutral pion production by detecting the two photons coming from the π^0 in coincidence using lead-glass detector when they, too, observed large yields of single photons.

Since then, a large number of experiments has been done to study the characteristics of these high energy gamma rays. These experiments can be categorized as either inclusive or exclusive high energy gamma ray measurements.

A large amount of work had been done to measure the inclusive photon production cross section. For example, Kwoto et al. [Kw 86] measured gamma rays produced in 30 MeV/nucleon ^{40}Ar + Au reaction, as well as from 44

MeV/nucleon ^{86}Kr beam on C, Ag, and Au targets. Our MSU group also conducted a systematic study [St 86] using ^{14}N beam of 20, 30 and 40 MeV/nucleon on C, Zn and Pb targets. Most of the measurements found the following major characteristics of the high energy photons from heavy-ion induced reactions: exponentially decreasing energy spectra with slope parameters which depend only weakly on projectile and target size; and slightly forward peaked angular distributions in the laboratory frame which can readily be transformed into a near isotropic or slightly dipolar angular distribution in the nucleon-nucleon center-of-mass frame.

A few exclusive measurements have also been carried out by several groups to obtain a more detailed understanding of the production mechanism. Hingmann et al. [Hi 87], for example, studied photons produced in the reaction $^{40}Ar + ^{158}Gd$ at E/A=44 MeV in coincidence with reaction products that carry impact parameter information. Lampis et al. of the MSU group [La 88] studied the production of the high energy photons in coincidence with light charged particles in the reaction of 30 MeV/nucleon ^{14}N + Pb. More coincidence measurements have been done recently to investigate the relationship between gamma multiplicity and the degree of violence of the reactions [Kw 88b], [He 87].

The majority of the high energy gamma ray experiments involve heavy-ion projectiles ($A_p \geq 12$) to study photons coming from nucleus-nucleus collisions. Few studies have been done on light-ion induced photon productions. Recently, results have become available [Kw 88a] [Pi 88] for proton beams of 72, 168 and 200 MeV bombarding various targets. The characteristics of the high energy photons produced in proton induced reactions share the basic features of the heavy-ion reactions, though there

are some differences. One such difference is that, in heavy ion induced reactions, although it is possible to observe photons having energies up to 2 to 3 time the beam energy/nucleon, the photon energy accounts for only a small fraction of the total available energy. In proton induced reactions, photons are observed to have energies up to all of the total energy available. This difference is attributed to the absence of Fermi motion and Pauli blocking in the proton projectile, which also makes detailed comparison with nucleus-nucleus results difficult.

Therefore, light-ion induced photon production is interesting in order to bridge the gap between heavy-ion and proton induced high energy photon production. As in the proton case, the photon energies are comparable to the total energy available in the system. On the other hand, it also resembles the heavy-ion reactions in that the Fermi motion in the projectile can also be important in determining the spectrum.

A.2. Theoretical models

Many theoretical models have been proposed for the high energy photon production mechanism. Most of the models are based on one of the three basic approaches: nucleus-nucleus bremsstrahlung, nucleon-nucleon bremsstrahlung, and statistical emission.

In an early model, Vasak et al. [Va 85] assume a collective nucleus-nucleus bremsstrahlung production mechanism, in which the gamma rays are thought to be produced early in the collision by the coherent bremsstrahlung of the projectile and the target nucleus. The model predicts a quadrupolar angular distribution in the center-of-mass frame, and a Z^2 dependence of the photon cross section. Most of the experimental data, as mentioned before,

points to the direction of a more isotropic angular distribution in the center-of-mass frame. However, as Herrmann et al. [He 84] point out, the angular distribution, when integrated over impact parameter, can be quite different from purely quadrupolar. Thus the angular distribution alone is not sufficient to judge the validity of this approach. In the next chapter, measurements of gamma rays produced in near symmetric systems of progressively larger masses will be compared with the Z dependence of the photon yield predicted by the model.

Most of the recent theoretical models of high-energy gamma ray production are based on a microscopic production mechanism, i.e. incoherent bremsstrahlung from individual nucleon-nucleon collisions within the colliding nuclei [Ba 86a] [Ba 86b] [Na 86] [Ne 87] [Ni 85] [Re 87]. The proton-proton bremsstrahlung is a quadrupole like process and its contribution are an order of magnitude smaller than the dipole like neutron-proton bremsstrahlung process[Ni 85]. Therefore, many nucleon-nucleon bremsstrahlung models attribute the production of the high energy photons to bremsstrahlung from first chance neutron-proton collisions early in the reaction. These models all predict the angular distribution in the nucleon-nucleon center-of-mass frame to be nearly isotropic or slightly dipolar, which is in good agreement with experimental observations.

In a third approach, the high energy photons are believed to come from the recoiling hot compound system in the later stage of the reaction. In this approach, the photons are produced by the bremsstrahlung of individual neutron-proton collisions within the hot zone [Ni 85] [Ne 87], or by the statistical emission from the hot zone [Pr 86] [Bo 88]. Since the photons are emitted from an equilibrated stage and the temperature of the hot zone

is governed by the total energy injected into the system, the relevant parameter in this model should be the total beam energy. In the light-ion induced reactions I will describe in the remaining of this chapter, we hope to be able to distinguish the first-chance n-p bremsstrahlung from the thermal approaches.

A.3. The Light-ion Induced Photon Production Experiment

In this experiment, we studied the reactions induced by three light-ion beams: 53 MeV/nucleon ^{4}He and ^{2}H, and ^{4}He at E/A=25 MeV. This combination not only enables us to study gamma ray productions from ^{4}He and ^{2}H at the same energy/nucleon, but the 25 MeV/nucleon ^{4}He and the 53 MeV/nucleon ^{2}H beams also allows us to compare their high energy gamma ray productions at about the same total energy ($E_{Total} \approx$ 100 MeV). These comparisons should give us some insight regarding whether the photon production mechanism is first chance nucleon-nucleon collision. In that case the spectrum from the 53 MeV/nucleon ^{2}H and ^{4}He beam at same energy/nucleon would be similar and differ by only a constant factor in yield. If the photons are produced by the multiple scattering within a recoiling 'fireball' whose characteristic only depends on the total energy of the hot zone, photons produced by 53 MeV/nucleon ^{2}H and 25 MeV/nucleon ^{4}He would have the same characteristic. The same three targets: 0.25mm thick C, 0.05mm Zn and 0.025mm Pb were used for all three beams.

B. Experiment Results

B.1. Photon Energy Spectra

Energy spectra of high energy gamma rays taken at 30°, 60°, 90°, 120° and 150° for the three beams on three targets are shown in Figure IV-1 to IV-9. The spectra can be separated into two regions, $E_\gamma < 25$ MeV and $E_\gamma > 25$ MeV. In the low energy region of $E_\gamma < 25$ MeV, the spectra are exponentially decreasing, with slopes typically ranging between 2-3 MeV. This region includes photons coming from the giant dipole resonance, from statistical decay of excited target fragments, as well as from bremsstrahlung photons [St 86]. The energy spectra in the high energy region ($E_\gamma > 25$ MeV) are also exponentially decreasing with increasing energy, but with much flatter slopes, ranging from 8 to 13 MeV. Photons in this energy region are believed to be predominately products of nucleon-nucleon bremsstrahlung, and are the primary interest in this thesis.

For the 53 MeV/nucleon ^{2}H induced reactions, the photon energy spectra from the three targets all extend to almost 100 MeV, which is close to the total energy available. In the case of ^{4}He induced reactions, the endpoint of gamma ray energy spectra are approximately 70 MeV for the 25 MeV/nucleon beam or nearly 3/4 of the total energy available, while it is 110 MeV for the 53 MeV/nucleon beam, which is slightly over half the available energy from the projectile. So the light-ion induced reactions share one of the features of proton induced reactions in that photons of energies up to a large fraction of the available energy were observed in all the systems we studied.

B.2. Angular Dependence

As can be seen from the Figures IV-1 to IV-9, energy spectra observed at different laboratory angles have slightly different slope parameters. The

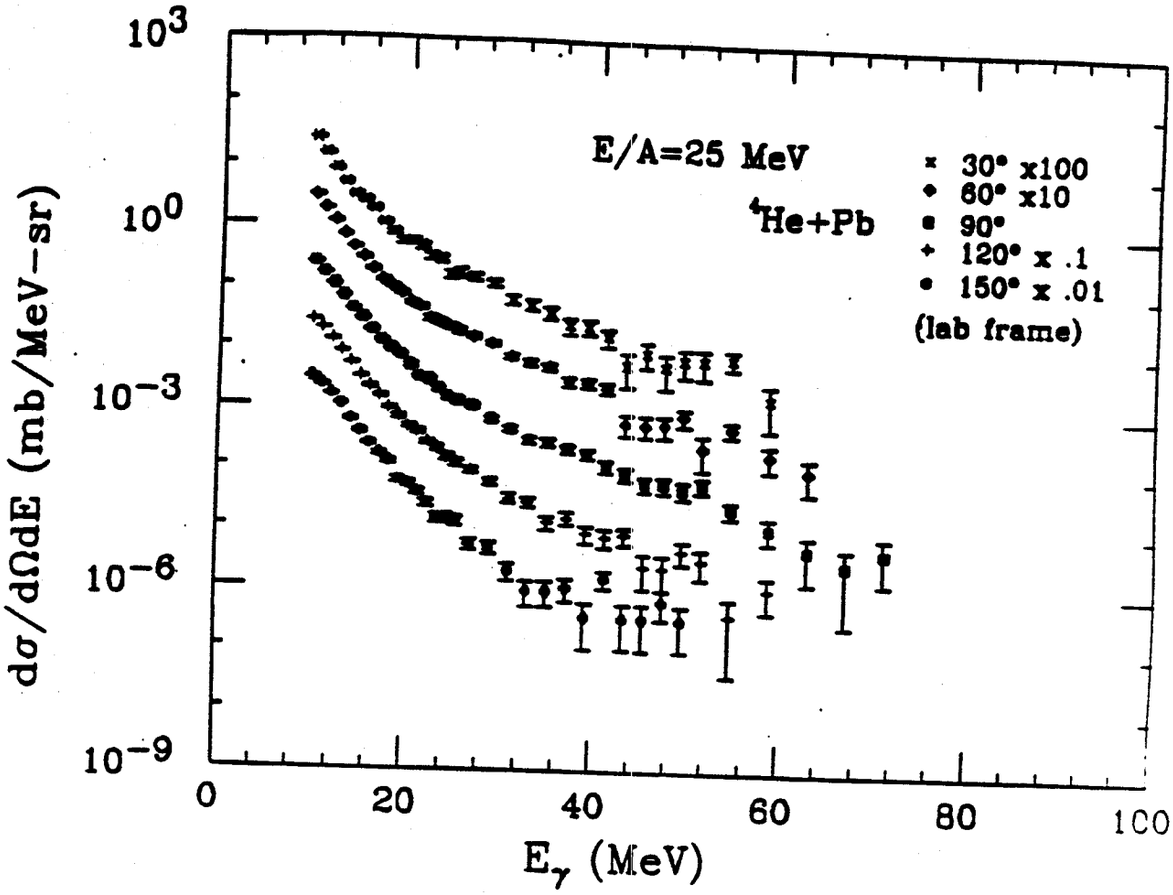

Figure IV-1 Photon energy spectra for 25 MeV/nucleon ^{4}He + Pb at laboratory angles of 30°, 60°, 90°, 120° and 150°.

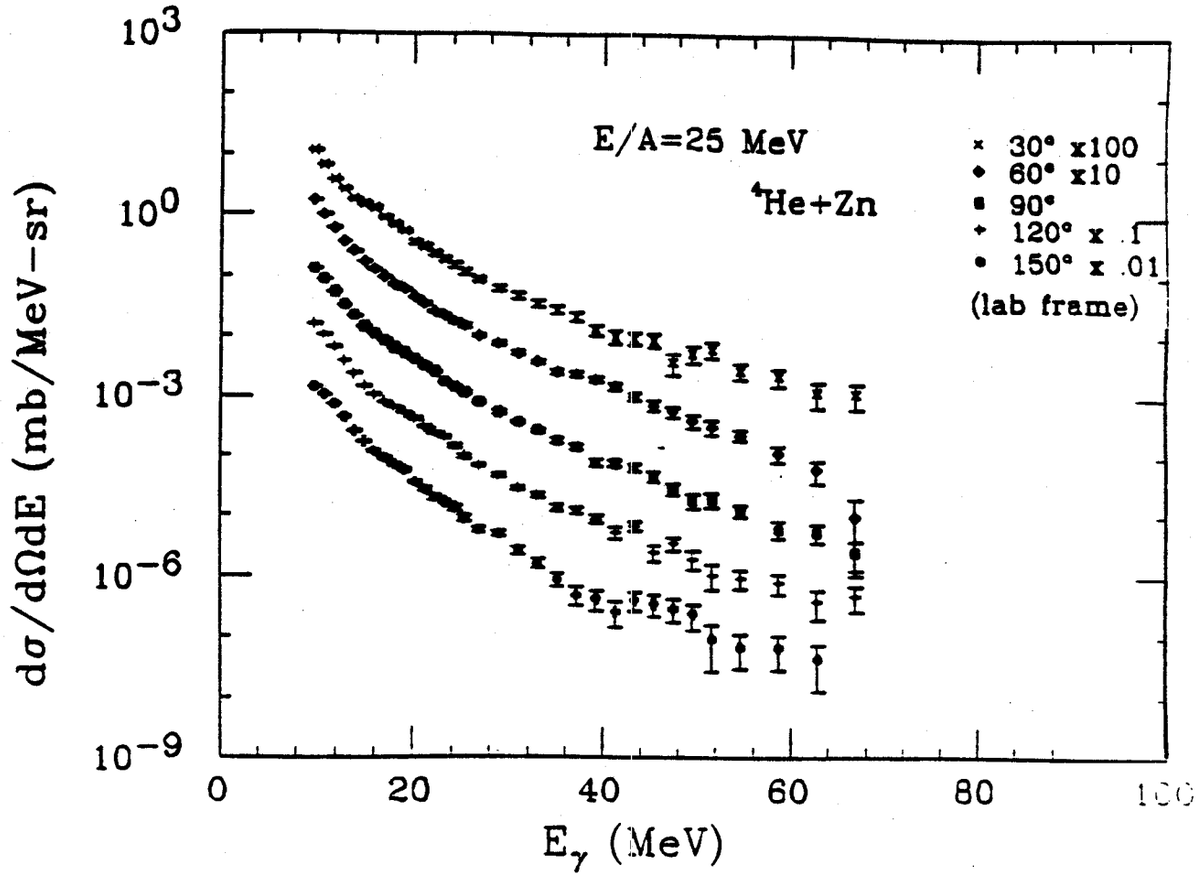

Figure IV-2 Photon energy spectra for 25 MeV/nucleon ^{4}He + Zn at laboratory angles of 30°, 60°, 90°, 120° and 150°.

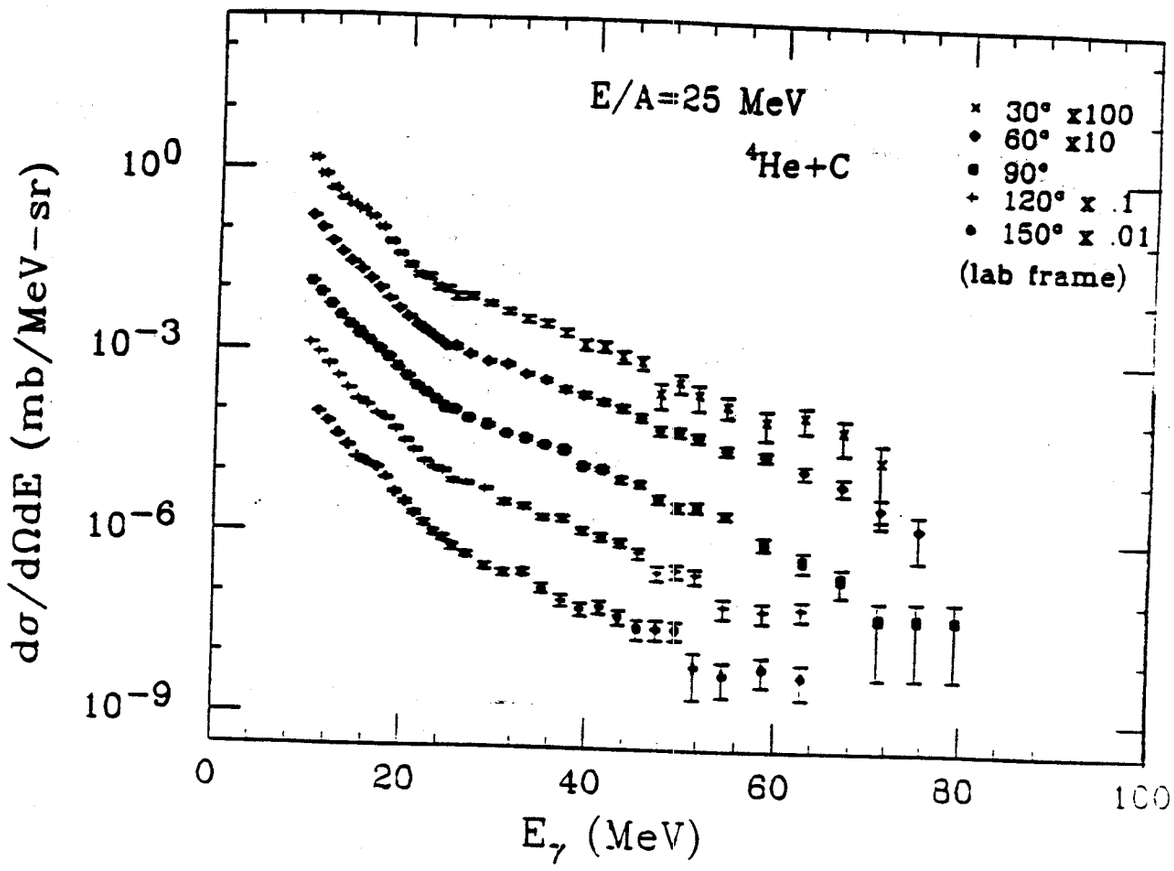

Figure IV-3 Photon energy spectra for 25 MeV/nucleon ^{4}He + C at laboratory angles of 30°, 60°, 90°, 120° and 150°.

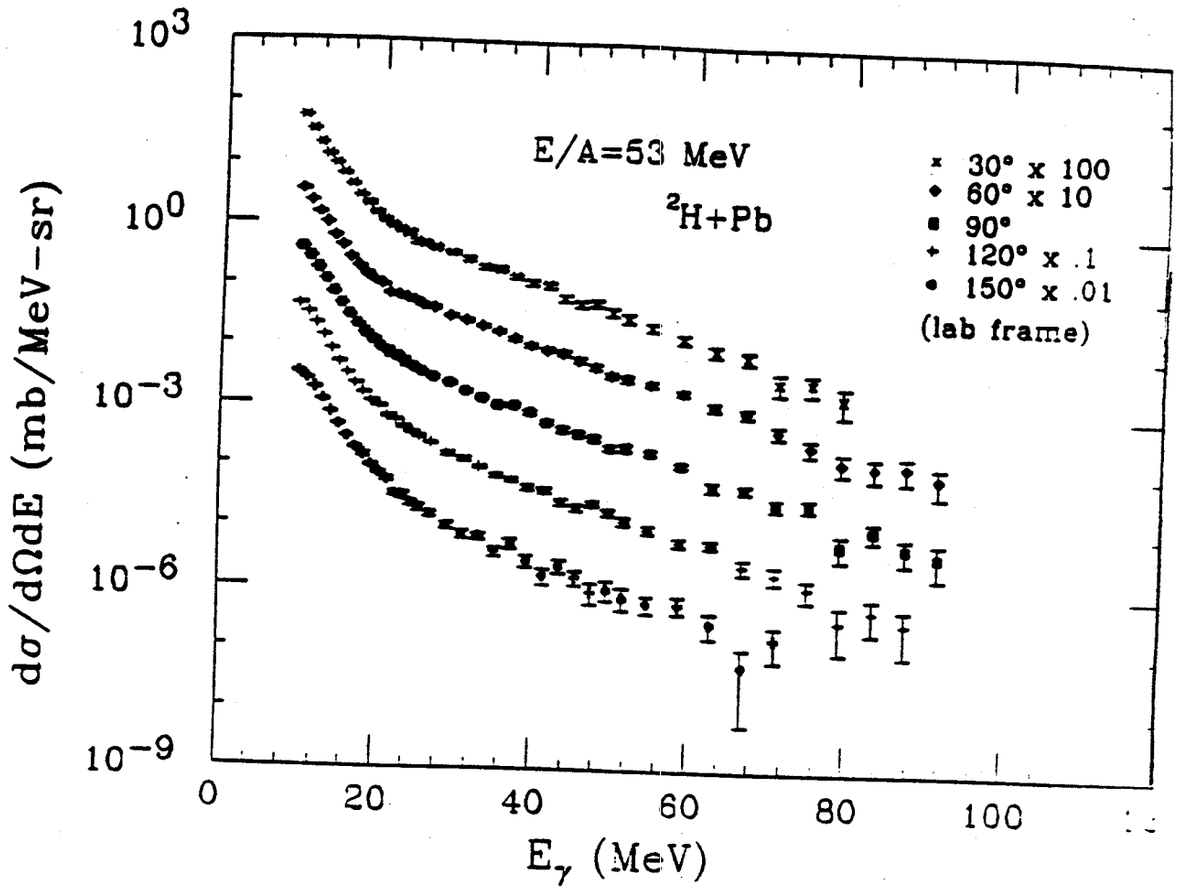

Figure IV-4 Photon energy spectra for 53 MeV/nucleon ^{2}H + Pb at laboratory angles of 30°, 60°, 90°, 120° and 150°.

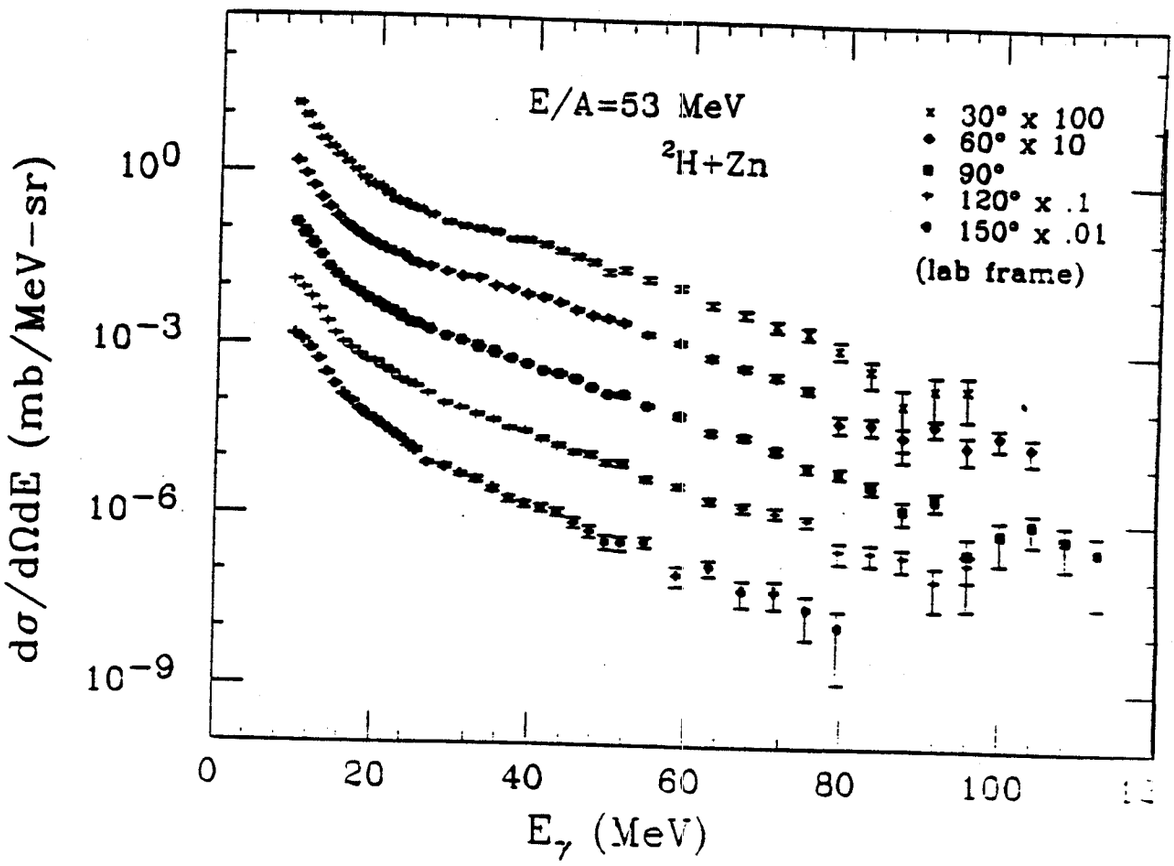

Figure IV-5 Photon energy spectra for 53 MeV/nucleon ^{2}H + Zn at laboratory angles of 30°, 60°, 90°, 120° and 150°.

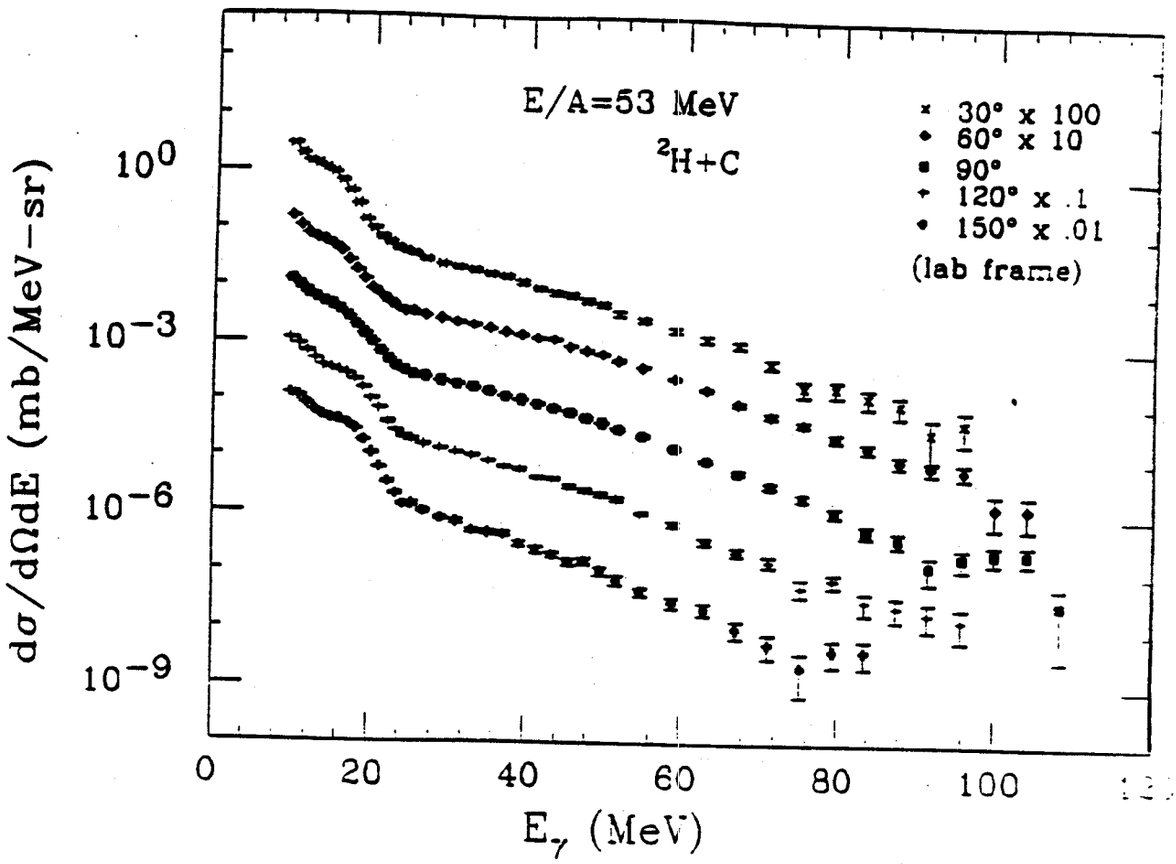

Figure IV-6 Photon energy spectra for 53 MeV/nucleon ^{2}H + C at laboratory angles of 30°, 60°, 90°, 120° and 150°.

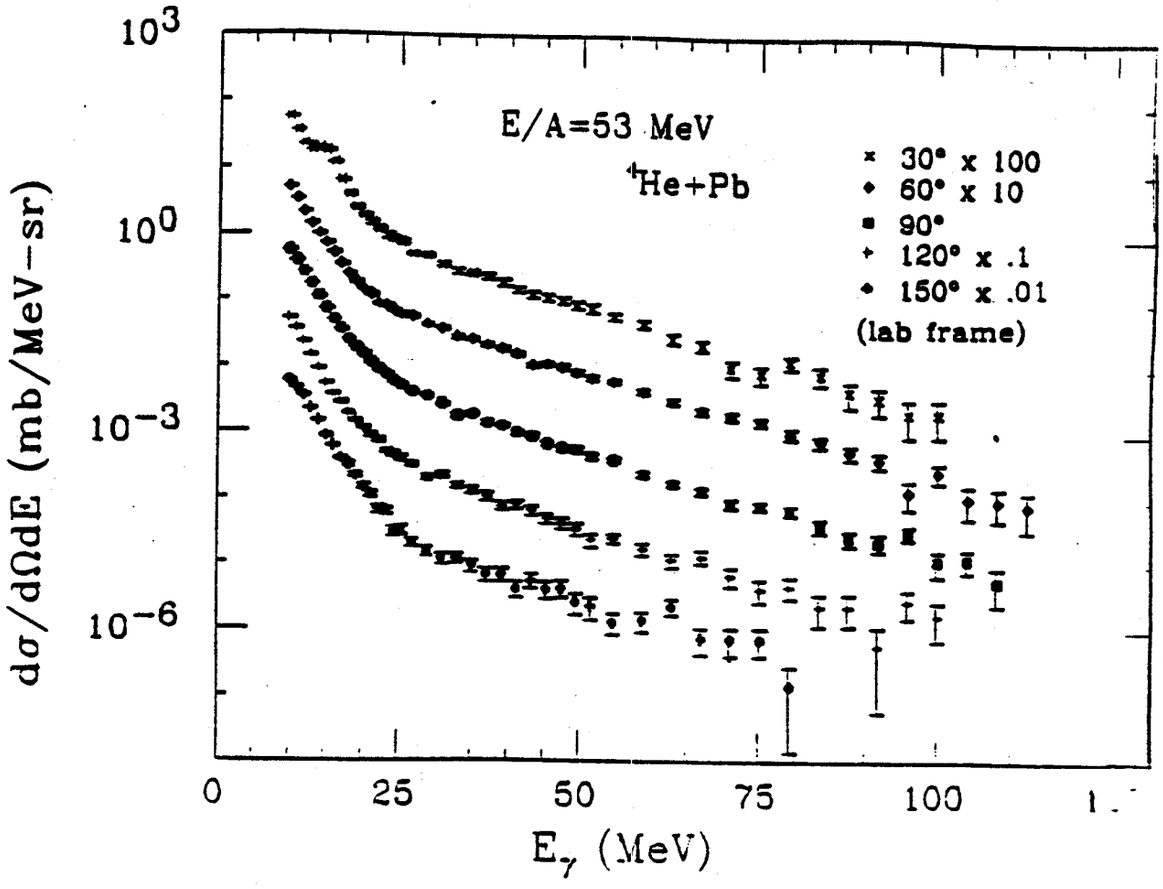

Figure IV-7 Photon energy spectra for 53 MeV/nucleon ^{4}He + Pb at laboratory angles of 30°, 60°, 90°, 120° and 150°.

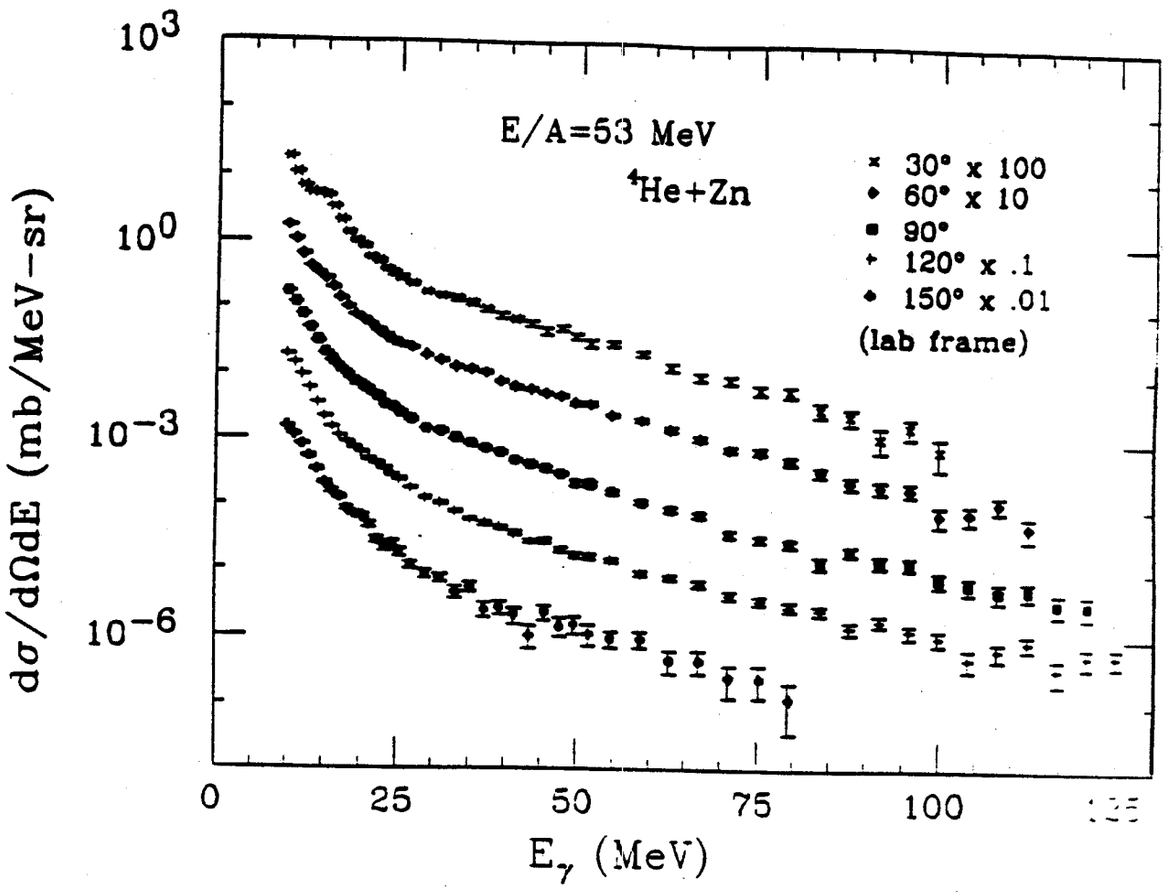

Figure IV-8 Photon energy spectra for 53 MeV/nucleon ^{4}He + Zn at laboratory angles of 30°, 60°, 90°, 120° and 150°.

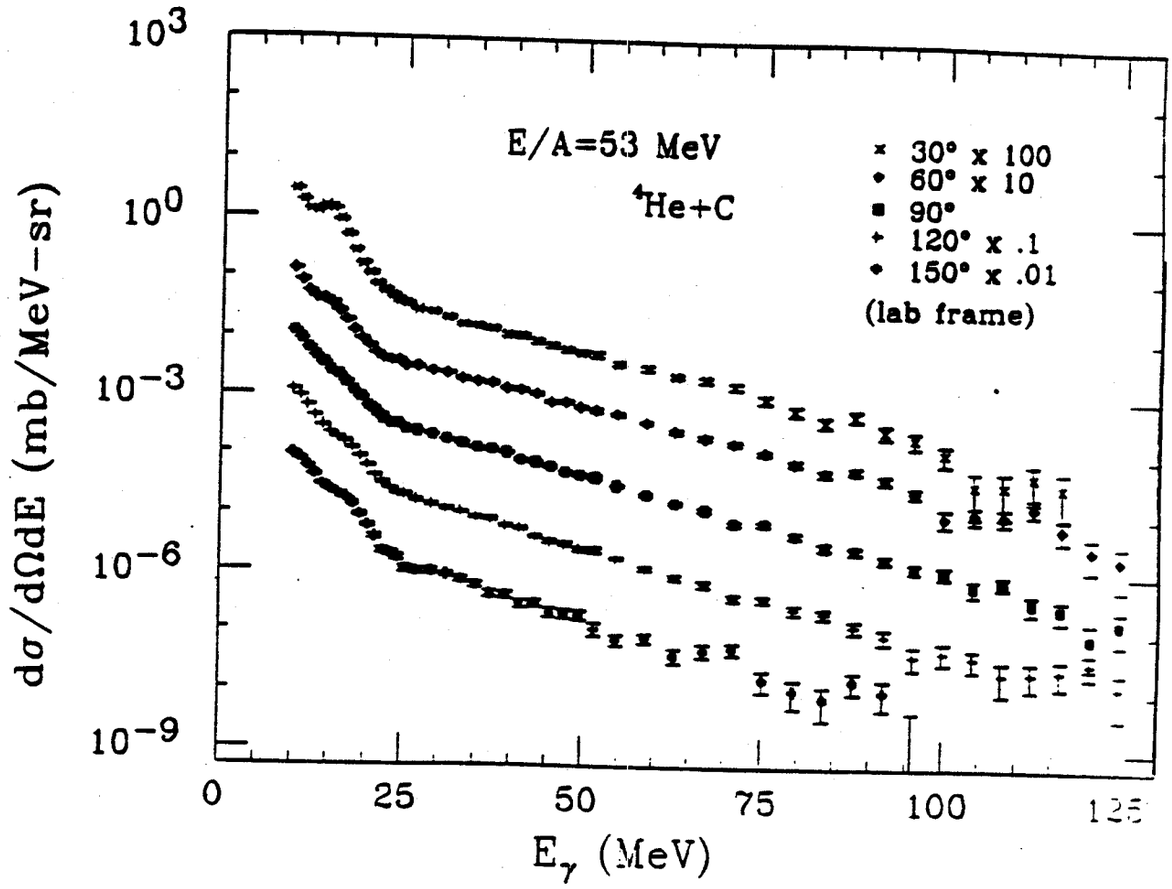

Figure IV-9 Photon energy spectra for 53 MeV/nucleon ^{4}He + C at laboratory angles of 30°, 60°, 90°, 120° and 150°.

larger the angle, the steeper the slopes. The angular distributions for a photon energy above 30 MeV (Figure IV-10) are typically forward peaked in the laboratory frame. These can be indications of photon emission from a recoiling source. The relationship between spectra at an angle θ_s in a source frame moving with velocity β with respect to the lab $\left(\frac{d^3\sigma(\theta,E)}{dEd\Omega}\Big|_s\right)$ and the observed laboratory spectra at angle θ_{lab} $\left(\frac{d^3\sigma(\theta,E)}{dEd\Omega}\Big|_{lab}\right)$ is as follows [Gr 85]:

$$E_s = E_{lab}\gamma(1 - \beta \cos\theta_{lab}), \qquad \text{where } \gamma = (1-\beta)^{-1/2}$$

$$\sin\theta_s = \sin\theta_{lab} \frac{1}{\gamma(1-\beta\cos\theta_{lab})}$$

$$\frac{d^3\sigma(\theta,E)}{dEd\Omega}\Big|_s = \frac{d^3\sigma(\theta,E)}{dEd\Omega}\Big|_{lab} \gamma(1-\beta\cos\theta) = \frac{d^3\sigma(\theta,E)}{dEd\Omega}\Big|_{lab} (E_s/E_{lab}) \qquad \text{(IV-1)}$$

The velocities of the moving source can be extracted from the two dimensional contour rapidity plots [Gr 85].

The rapidity y, of a particle moving with velocity β in direction θ in a certain reference frame, is defined as $y = \frac{1}{2} \ln \left[\frac{1+\beta\cos\theta}{1-\beta\cos\theta}\right] = \frac{1}{2} \ln \left[\frac{1+\beta_{\parallel}}{1-\beta_{\parallel}}\right]$ in that frame. If, in the laboratory frame, the rapidity of a particle with velocity β'' is y'', then viewed in a frame moving with velocity β with respect to the lab frame, the same particle will have a different velocity β' and rapidity y'. The relation between the parallel components of the three velocities β, β', and β'' is known [Ja 00] as $\beta'' = \frac{\beta + \beta'}{1 + \beta\beta'}$. Then the additive property of the rapidity can be shown in the following:

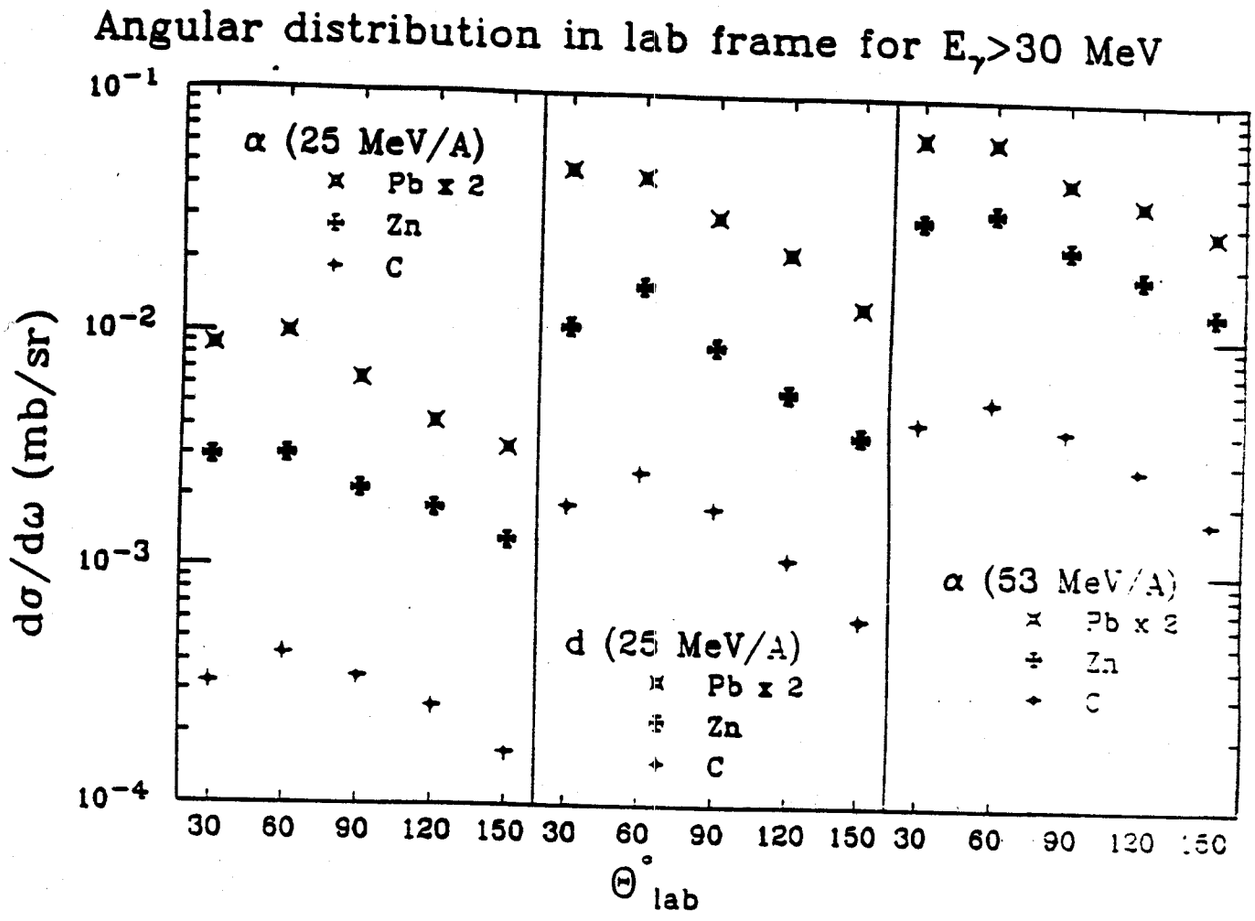

Figure IV-10 Integrated angular distributions for photon energies above 30 MeV in the laboratory frame.

$$y'' = \frac{1}{2}\ln\left(\frac{1+\beta}{1-\beta}\right) = \frac{1}{2}\ln\left(\frac{1+\frac{\beta+\beta'}{1+\beta\beta'}}{1-\frac{\beta+\beta'}{1+\beta\beta'}}\right)$$

$$= \frac{1}{2}\ln\left(\frac{(1+\beta)(1+\beta')}{(1-\beta)(1-\beta')}\right) = \frac{1}{2}\ln\left(\frac{1+\beta}{1-\beta}\right) + \frac{1}{2}\ln\left(\frac{1+\beta'}{1-\beta'}\right)$$

i.e. $y'' = y + y'$

To utilize the rapidity plot to determine the source velocity, we have to express the photon double differential cross section in a Lorentz invariant form. The relationship between the photon invariant cross section and the experimental cross section is [Bj 65]:

$$\frac{d\sigma}{d^3p} = \frac{d\sigma}{(1/E)d^3p} = \frac{d\sigma}{(1/E)p^2dpd\Omega} = \frac{1}{p}\frac{d\sigma}{dEd\Omega}$$

Figure IV-11 is a typical example of a contour plot of the photon invariant cross section versus the rapidity and the transverse energy ($E_{trans} = E_\gamma \sin\theta$), for the reaction d + Pb, one of the systems we studied. The rapidity distribution appears to be nearly symmetric about a centroid with rapidity $y \approx 0.16$. By taking advantage of the additive property of the rapidity parameter, the source velocity β can be easily extracted from the centroid of the rapidity distribution, assuming Y-ray emission from a single moving source. In the case of d + Pb, it is close to the half-rapidity of the beam $y_{nn}=0.166$.

Figure IV-12 through IV-14 shows all the rapidity plots for the 9 systems studied, also the nucleon-nucleon center-of-mass rapidities (Y_{nn}) of each beam projectile are indicated on the corresponding graphs as well. All the rapidity plots are nearly symmetric with respect to the nucleon-nucleon

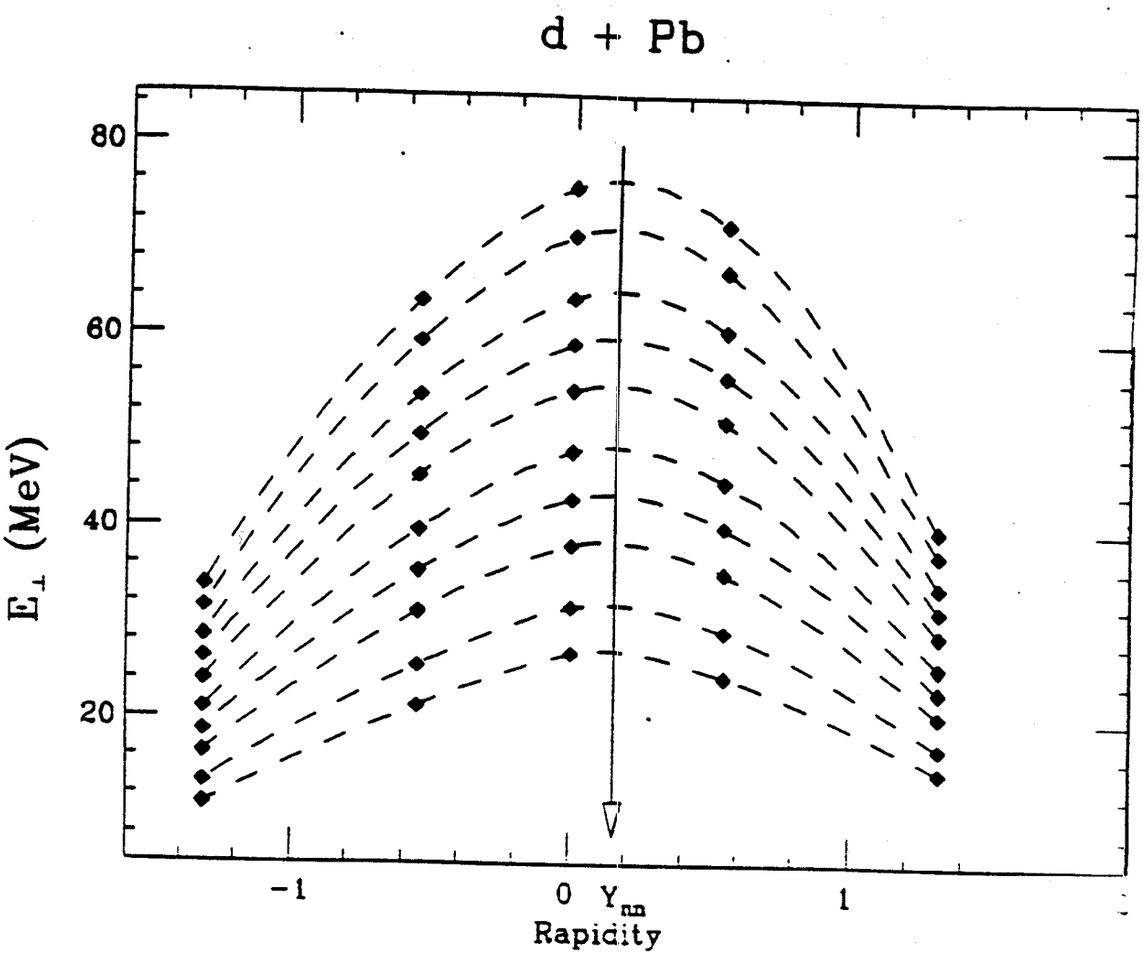

Figure IV-11 Rapidity distributions for 53 MeV/nucleon ^2H + Pb induced high energy gamma ray.

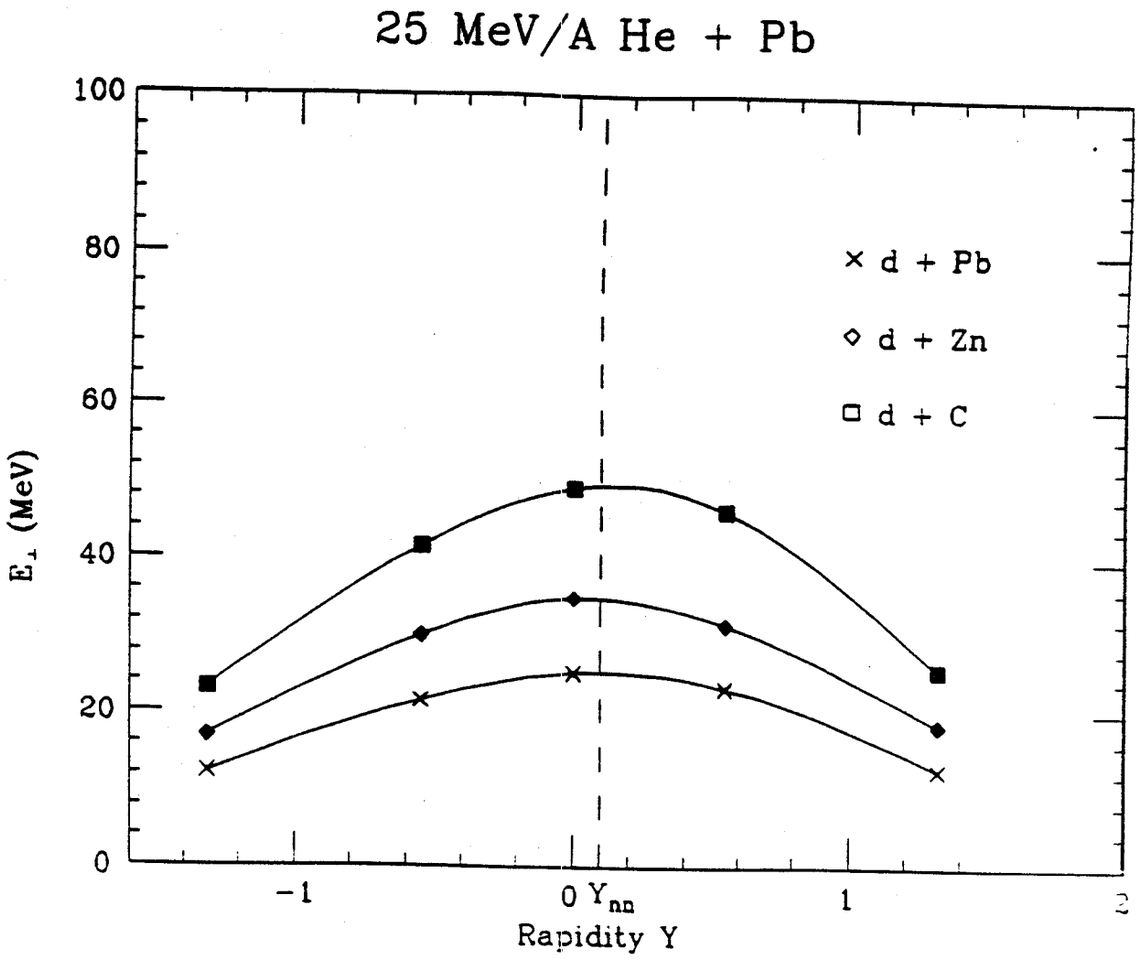

Figure IV-12 Rapidity plot for 25 MeV/nucleon ^{4}He beam on three different targets: Pb, Zn and C.

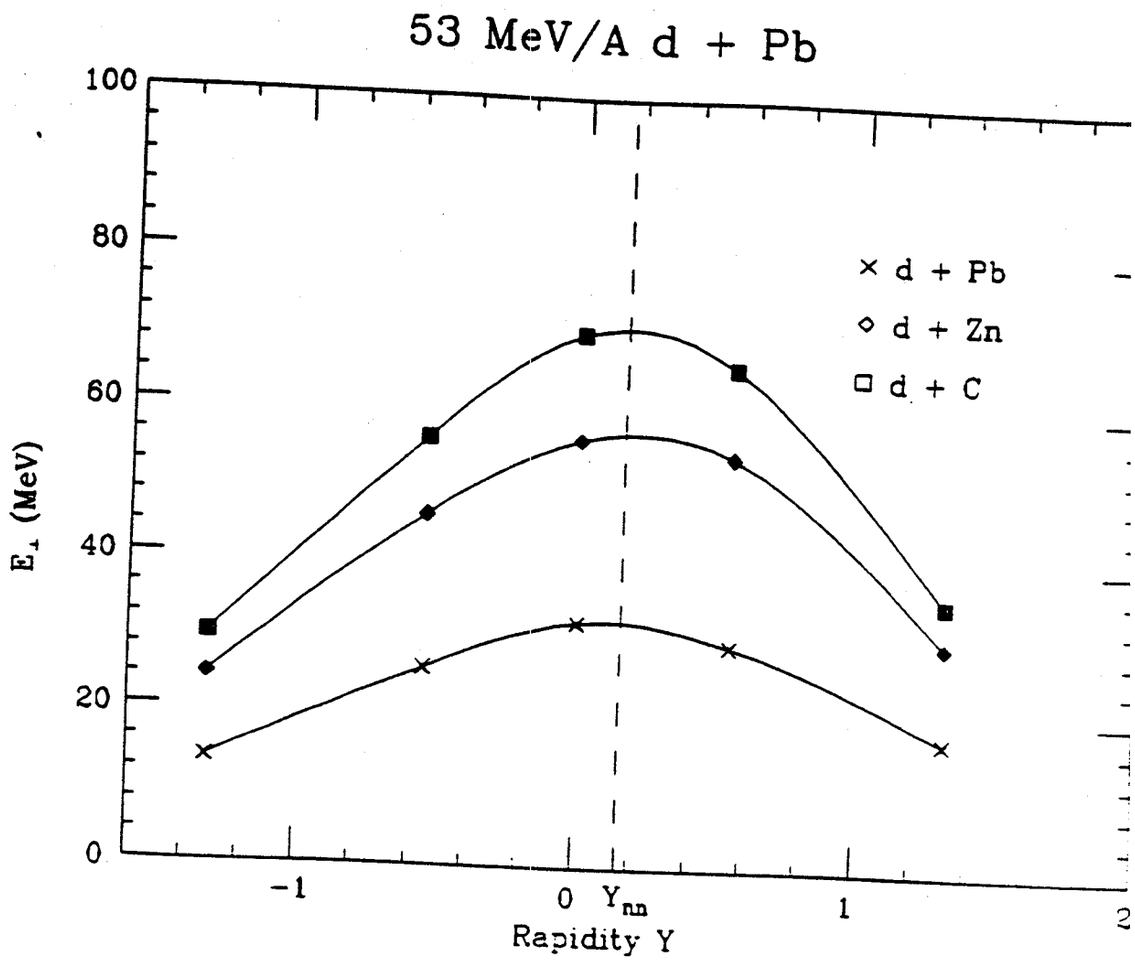

Figure IV-13 Rapidity plot for 53 MeV/nucleon ^{2}H beam on three different targets: Pb, Zn and C.

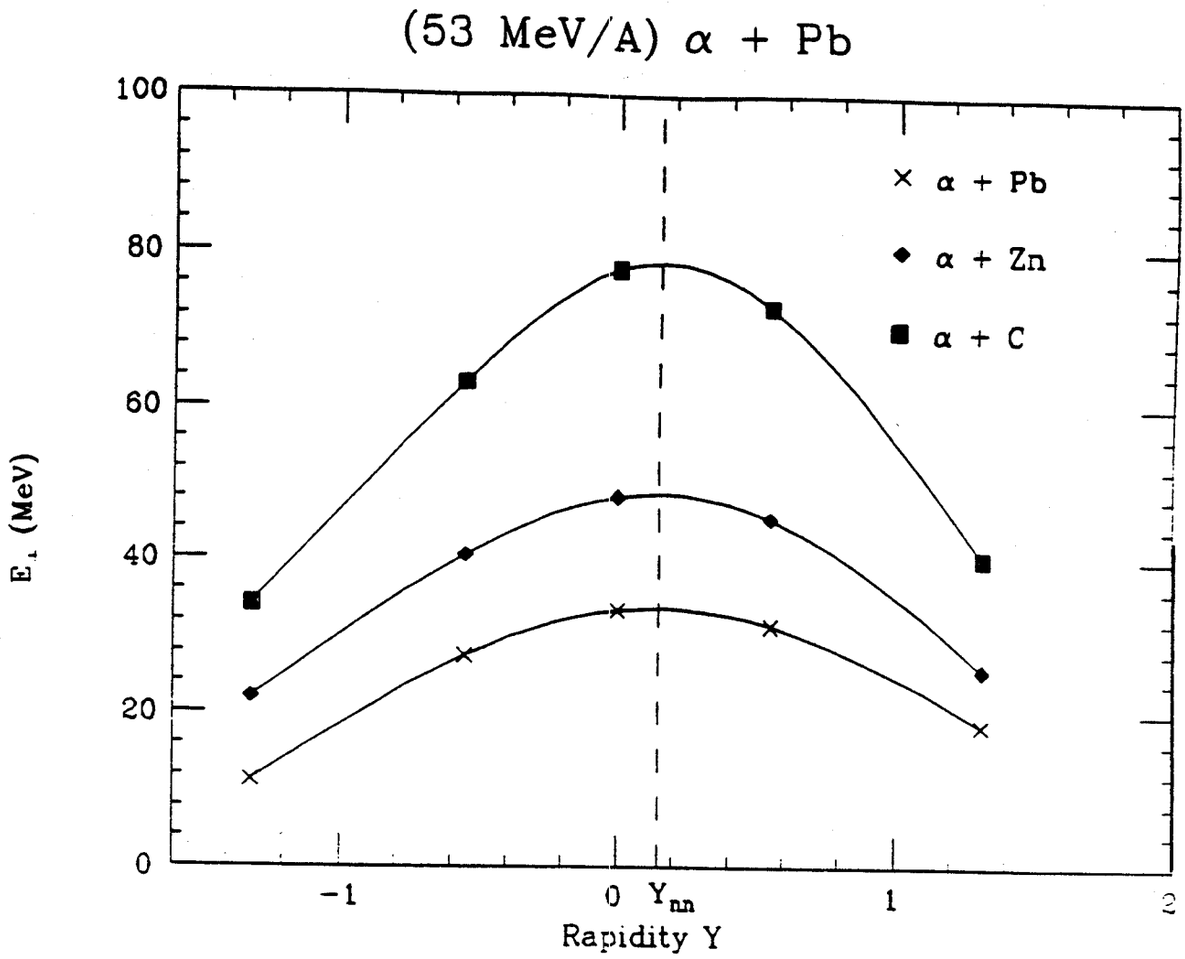

Figure IV-14 Rapidity plot for 53 MeV/nucleon ^{4}He beam on the three different targets: Pb, Zn and C.

center-of-mass rapidity line. Quantitative values of the source velocity β_{exp} can also be extracted using a cubic spline fit to the rapidity plots, and are shown in table IV-1 in comparison with the nucleon-nucleon center-of-mass velocity β_{nn}. It was found that the source velocities β_{exp} are quite close to the nucleon-nucleon center-of-mass velocity β_{nn}, with a slight systematic shift to lower velocity.

Figure IV-15 shows the photon angular distributions transformed into the nucleon-nucleon center-of-mass frame. They are roughly symmetrical with respect to 90° in this frame. One of the interesting features is a quite pronounced dipole component in all three of the carbon target data. The data from the heavier targets of Zn and Pb is mainly isotropic, but it also shows a small dipole component.

C. Discussion

C.1. Moving source model fit

Many of the interesting features of the data, such as the strength of the dipole component, the differences between β_{exp} and β_{nn}, as well as the slope parameter and overall strength of the energy spectra, could be better understood using a more systematic approach. A simple moving source model by Tekashi Murakami was employed to fit the data. The model assumes a forward-backward symmetric Y-ray emission from a moving source frame recoiling with a velocity β, and a photon production cross section energy dependence in that frame of the form

$$\left.\frac{d^2\sigma}{d\Omega dE}\right|_s = A\,(1-B\cos^2\theta_s)\,e^{-E/T}$$

Table IV-1 Comparison of extracted source velocities β_{exp} to nucleon-nucleon center-of-mass velocities β_{nn} and nucleus-nucleus center-of-mass velocities β_{NN}.

BEAM	TARGET	E/A(MeV)	β_{exp}	β_{nn}	β_{NN}
^{4}He	C	25	0.08	0.115	0.049
^{4}He	Zn	25	0.07	0.115	0.013
^{4}He	Pb	25	0.10	0.115	0.004
^{2}H	C	53	0.16	0.166	0.040
^{2}H	Zn	53	0.17	0.166	0.010
^{2}H	Pb	53	0.12	0.166	0.003
^{4}He	C	53	0.16	0.166	0.070
^{4}He	Zn	53	0.15	0.166	0.019
^{4}He	Pb	53	0.13	0.166	0.006

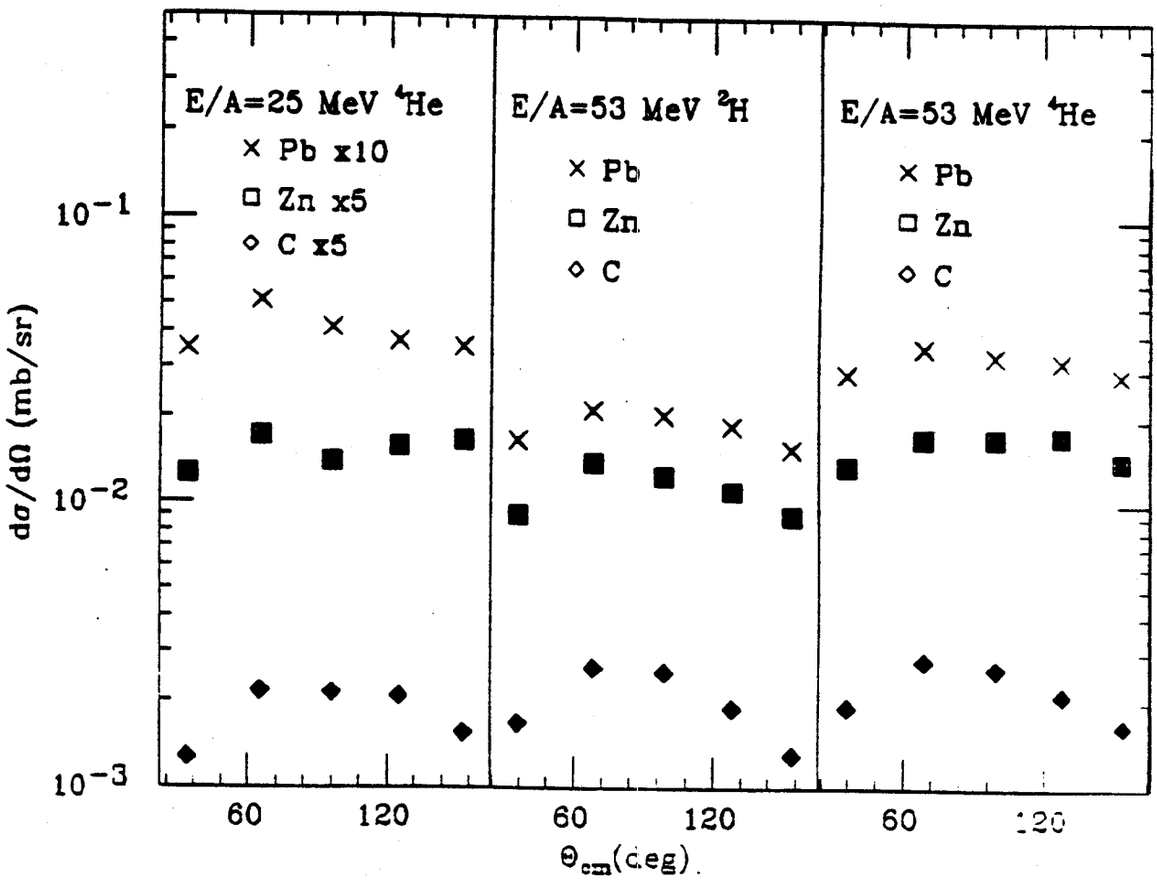

Figure IV-15 Integrated angular distributions for photon energies above 30 MeV in the nucleon-nucleon center-of-mass frame.

When transformed into the laboratory frame (using eq. IV-1), it takes the form of

$$\left.\frac{d^2\sigma}{d\Omega dE}\right|_{lab} = \frac{A}{C}\left[1-B\left(1-\frac{\sin^2\theta}{C^2}\right)\right] e^{-EC/T}$$

where $C=\gamma\,(1-\beta\cos\theta_{lab})$, $\gamma = (1-\beta)^{-1/2}$

Using this model, we carried out a global fit to the five energy spectra from the five laboratory angles and obtained the best fit values of the following parameters: overall strength A, dipole strength B, slope parameter T and extracted source velocity β_{exp}.

C.2. The Moving Source

Table IV-2 shows the results of the fits to all 9 systems. The values of the nucleon-nucleon center-of-mass velocities β_{nn} are also shown in the Table next to the extracted values of the source velocities β_{exp}. It was found that the source velocities β_{exp} extracted from the experimental data set, although very close to their corresponding nucleon-nucleon center-of-mass velocities β_{nn}, appear to be systematically slightly smaller, confirming the previous result using the rapidity plot method. This slight shift may be understood, by assuming target nucleons with higher Fermi momentum opposite to the beam direction have a larger contribution in the production of bremsstrahlung photons, thus resulting a lower effective nucleon-nucleon center-of-mass velocity. Or, it could also be attributed to bremsstrahlung photons coming from multiple scattering. Only the bremsstrahlung photons from the first chance nucleon-nucleon collision would be symmetric in the nucleon-nucleon center-of-mass frame, while gamma rays from subsequent scattering could appear to lower the velocity of the source.

Table IV-2 Parameters for the moving source model fit.

BEAM	TARGET	E/A(MeV)	β_{exp}	β_{nn}	T(MeV)	A (mb/MeV-sr)	B
^{4}He	C	25	0.08±0.01	0.115	7.4±0.2	0.0034±0.001	0.48±0.10
^{4}He	Zn	25	0.08±0.01	0.115	6.5±0.2	0.049 ±0.01	0.35±0.15
^{4}He	Pb	25	0.11±0.01	0.115	6.3±0.2	0.080 ±0.02	0.36±0.19
^{2}H	C	53	0.15±0.01	0.166	10.6±0.2	0.0042±0.001	0.60±0.05
^{2}H	Zn	53	0.14±0.01	0.166	9.4±0.2	0.034 ±0.01	0.55±0.06
^{2}H	Pb	53	0.14±0.01	0.166	9.0±0.2	0.066 ±0.02	0.36±0.08
^{4}He	C	53	0.16±0.01	0.166	13.3±0.2	0.0020±0.0006	0.52±0.05
^{4}He	Zn	53	0.13±0.01	0.166	12.1±0.2	0.018 ±0.006	0.39±0.08
^{4}He	Pb	53	0.15±0.01	0.166	11.3±0.2	0.043 ±0.01	0.38±0.09

A second fit which assumes the source velocity to be the nucleon-nucleon center-of-mass velocity are shown in Figure IV-16 and IV-17. They appear to be rather good fits. The parameters A, B and T given in table IV-2 as well, are obtained using the second fit, in which the fixed source velocities β_{nn} of the corresponding beam energy were used as the source velocity.

C.3. Y-ray angular distributions in the source frame

Although most of the heavy ion induced high-energy photon experiments have reported mainly isotropic angular distributions in the nucleon-nucleon center-of-mass frame, the existence of a dipole component has also been reported both by Grosse et al [Gr 85] and by Bertholet et al [Be 87]. As shown on Figure IV-17, though most pronounced in the carbon target data, all of the systems we studied exhibit some dipole component. The relative strength of the dipole component (table IV-2) for the reactions we studied ranges from approximately 35% for most of the heavier systems up to nearly 60% for the lighter system, while values ranging from 16% to 31% were found by Bertholet et all [Be 87] using heavy-ion beam of 44 MeV/nucleon ^{86}Kr on various targets.

The carbon target data in particular, have rather strongly enhanced dipole components. The values of B of 0.48, 0.52 and 0.60, are significantly larger than those of Bertholet [Be 87] from heavy-ion reactions. However, our light ions on lead target data, which show a dipole strength of about 35%, are comparable to the the Bertholet [Be 87] data. Notice [Ja 75b] that the angular distribution for the nonrelativistic bremsstrahlung process pn→pnY takes the form of $(1 - \frac{3}{5}\cos^2\theta)$ in the long wave length expansion,

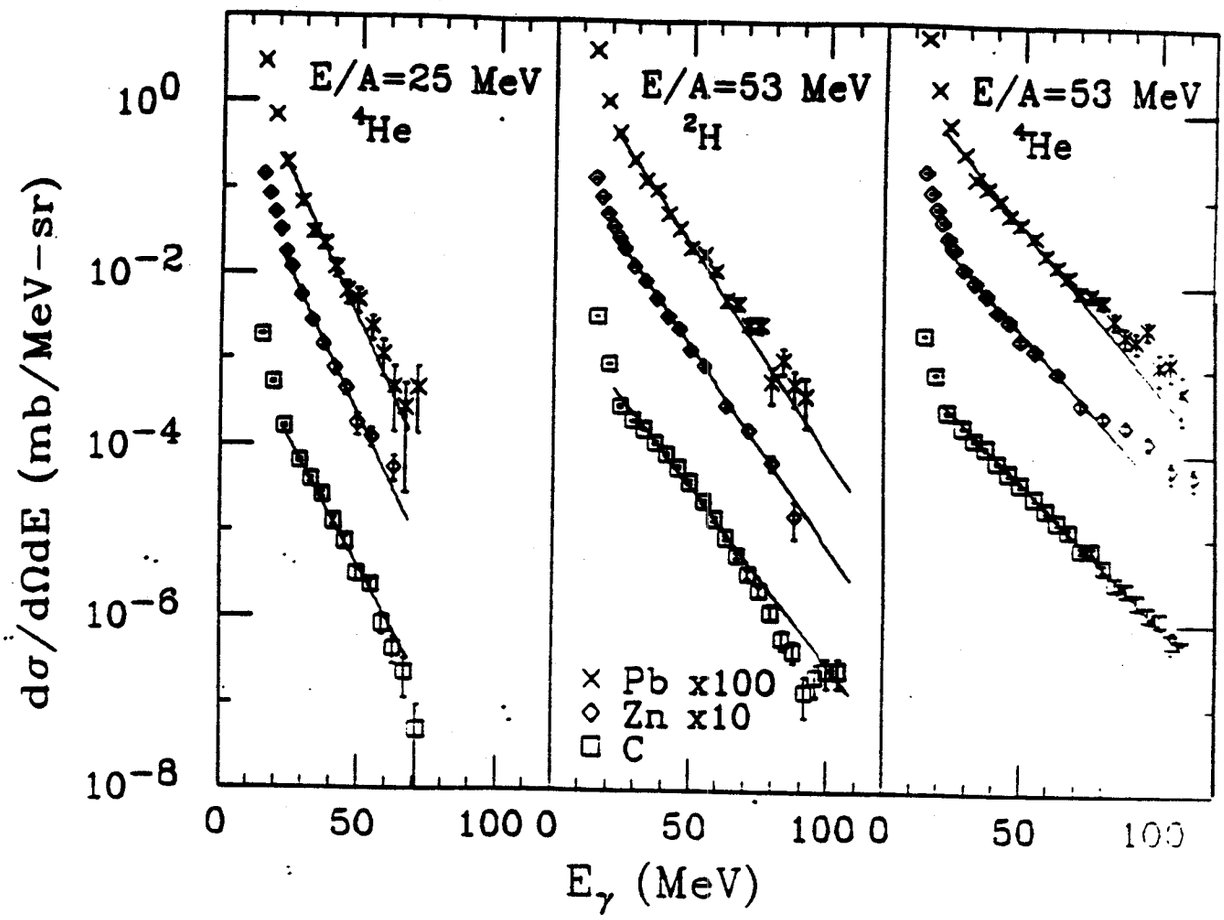

Figure IV-16 Moving source model fit to the photon energy spectra at 90° in the laboratory for all 9 reactions studied.

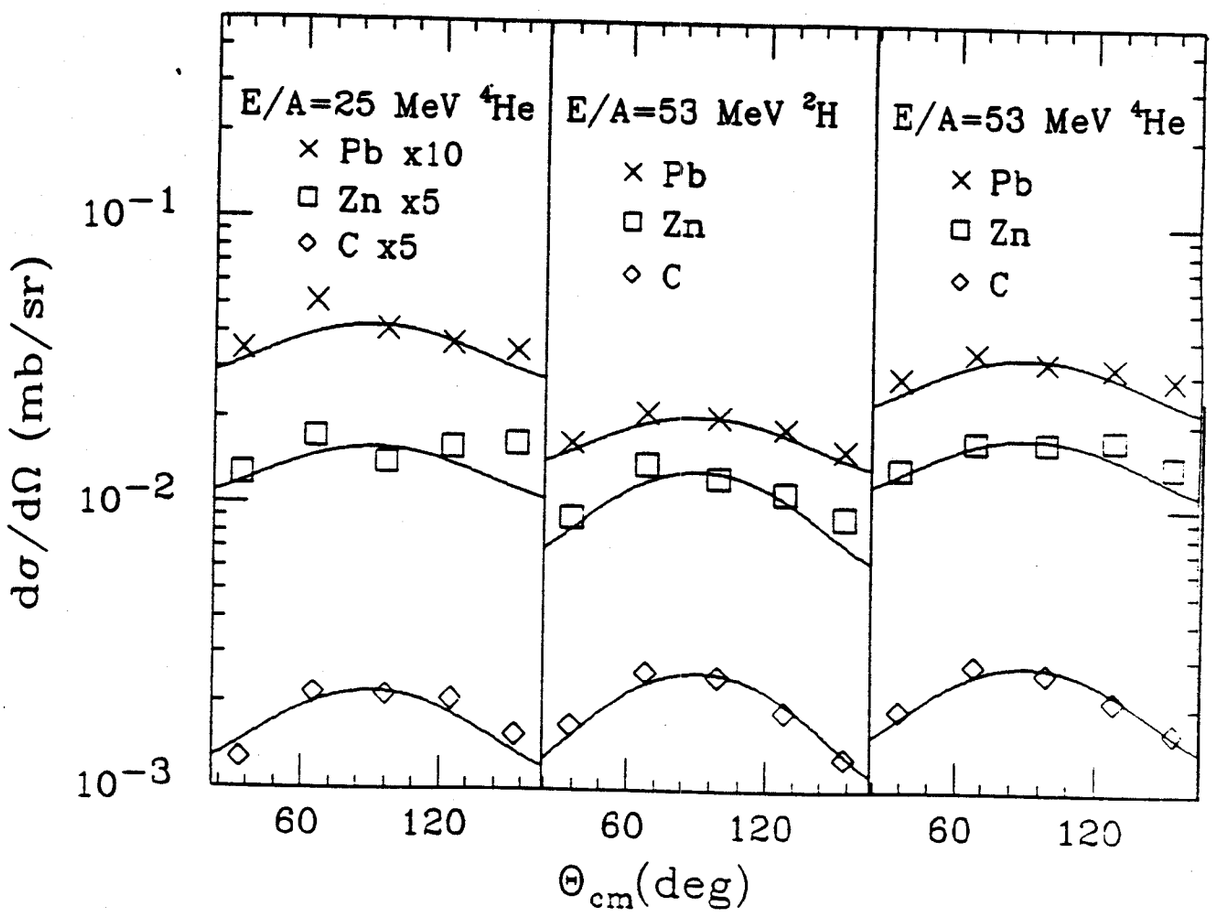

Figure IV-17 Moving source model fit to the photon integrated angular distributions in the nucleon-nucleon center-of-mass frame.

i.e. B=0.6. The dipole component in the carbon target data is close to that expected for the free np bremsstrahlung process, while that of the lead targets is only a little over half of the free np bremsstrahlung value.

This target mass dependence of the dipole component may be qualitatively explained by assuming that the dipole component comes from first chance np collisions while the subsequent multiple scatterings are isotropic in nature. Thus the lighter targets like carbon, having relatively smaller contribution from second or third scatterings than the heavier targets such as lead, can appear to have a substantially larger dipole component than heavier targets.

C.4. Target and projectile mass dependence of Y-ray intensity

The increased contribution of multiple scattering in heavier targets may also be responsible for the target mass dependence in the slope parameters of the photon energy spectra. Figure IV-18 shows the photon energy spectrum at 90° angle induced by the 53 MeV/nucleon ^{4}He beam bombarding three different targets. Unlike most of the heavy-ion data where the slope parameters are largely independent of the target mass, the slope parameters of the light-ion induced Y-ray spectra decrease slightly with increasing target mass. If one assumes that photons produced in the first collisions are more likely to have higher energy than photons from subsequent collisions, then as the contribution of multiple scattering increases with target mass, the slope parameters would decrease.

One of the interesting features in the energy spectra of the high energy photons coming from light-ion reaction is the projectile mass dependence. To illustrate this, the energy spectra of the three different

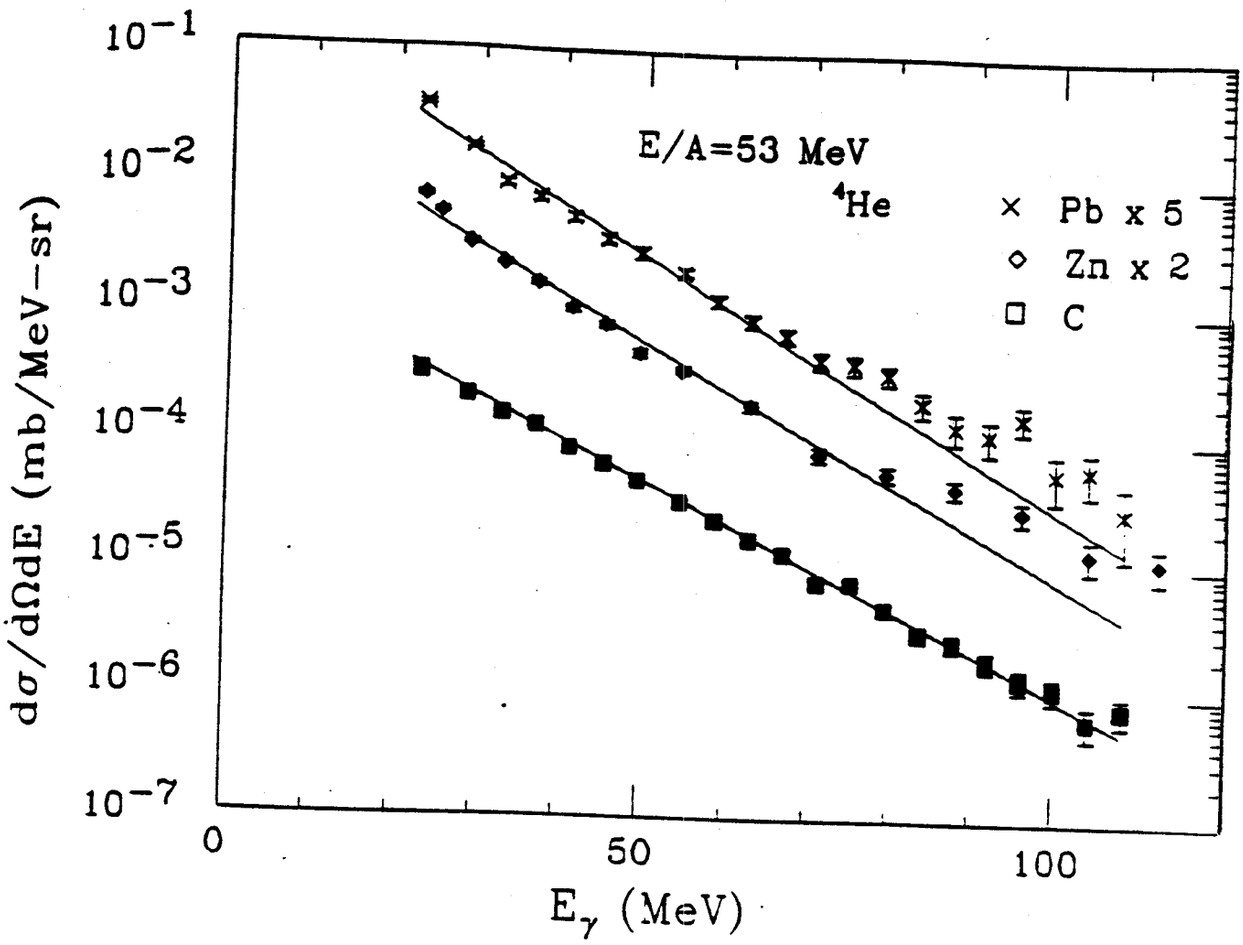

Figure IV-18 Target dependence of the photon cross section.

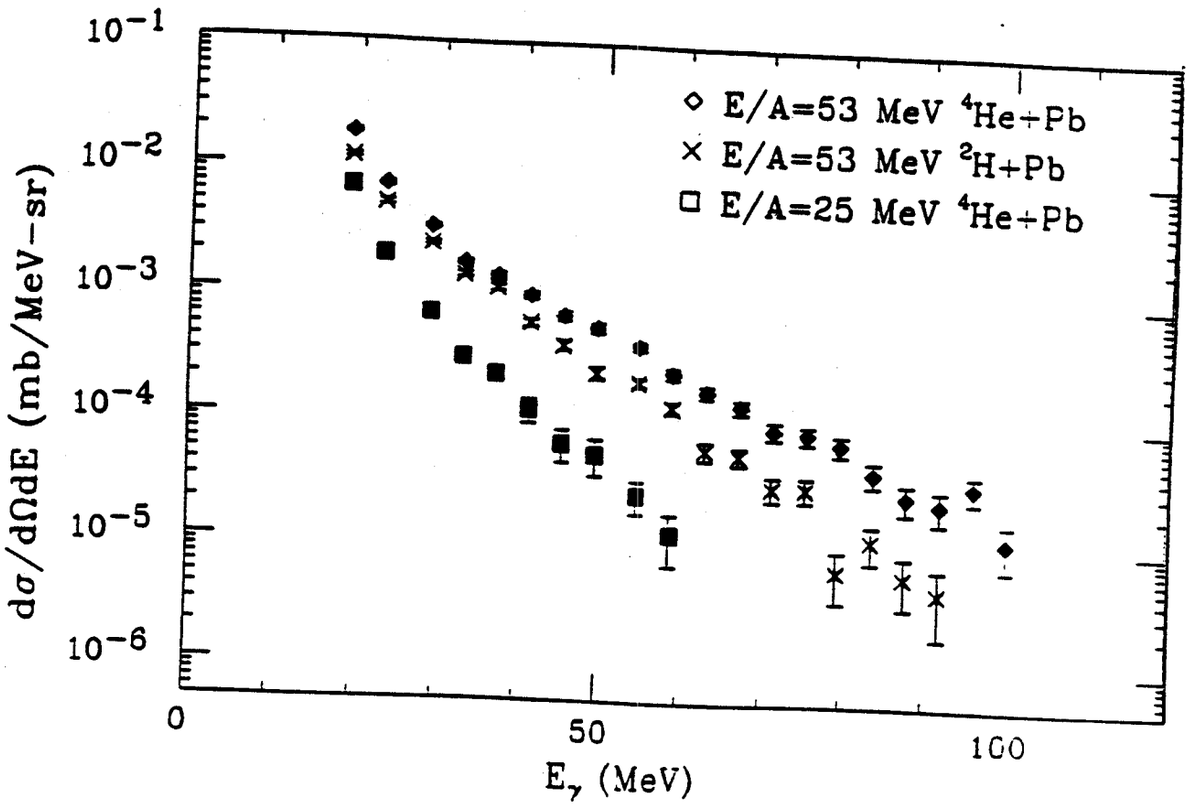

Figure IV-19 Projectile dependence of the photon cross section.

beams on the Pb target are plotted in Figure IV-19. The slope parameters of the three beams are 11.3 MeV, 9.0 MeV and 6.3 MeV respectively.

While the slope parameters of high energy photon spectra in most heavy-ion induced reactions with the same energy/nucleon were found to be the same, the 53 MeV/nucleonlight-ion induced reactions produced slope parameters ranging from 9.0 - 10.6 MeV for ^{2}H beam and 11.3-13.3 MeV for ^{4}He beam of the same energy/nucleon (table IV-2). These values not only depend on projectile (as well as target) mass, but they are also substantially smaller than those obtained in heavy-ion induced reactions at similar beam energy/nucleon. By comparison, for example, Grosse et al.[Gr 86] studied the reaction $^{12}C + C$ at 48 MeV/nucleon and observed a slope parameter of 19 MeV. Table IV-3 and IV-4 show our results together with results from other groups for heavier systems at similar energies.

D. Conclusion

According to the statistical model which assumes the photons are produced within a hot compound system, the 53 MeV/nucleon ^{2}H and 25 MeV/nucleon ^{4}He projectiles would produce nearly the same excitation energy, hence the same compound nucleus temperature. So, the photon energy spectra from the two reactions should have the same slope parameter according to the model. Therefore, the observed significant difference in their slope parameters indicates that high energy photons do not come from a hot compound nuclear system. On the other hand, the difference in the spectra of 53 MeV/nucleon ^{2}H and ^{4}He induced reactions contradicts also the naive first collision model, which predicts the same slope parameter for the two reactions and only a factor of two difference in yield. Part of the

Table IV-3 Comparison of slope parameters for different systems at similar energies per nucleon.

BEAM	TARGET	E/A(MeV)	T(MeV)	References
^{32}S	Al	22	10.8	[Stl 87]
^{32}S	Ni	22	10.0	[Stl 87]
^{32}S	Au	22	9.1	[Stl 87]
^{4}He	C	25	7.4±0.2	
^{4}He	Zn	25	6.5±0.2	
^{4}He	Pb	25	6.3±0.2	

Table IV-4 Comparison of slope parameters of 53 MeV/nucleon light-ion data with systems of different projectile masses at similar energies.

BEAM	TARGET	E/A(MeV)	T(MeV)	References
^{40}Ar	Gd	44	12.6	[Hi 87]
^{86}Kr	C	44	11.7	[Be 87]
^{86}Kr	Ag	44	12.5	[Be 87]
^{86}Kr	Au	44	12.1	[Be 87]
^{12}C	C	48	19	[Gr 86]
^{2}H	C	53	10.6±0.2	
^{2}H	Zn	53	9.4±0.2	
^{2}H	Pb	53	9.0±0.2	
^{4}He	C	53	13.3±0.2	
^{4}He	Zn	53	12.1±0.2	
^{4}He	Pb	53	11.3±0.2	

difference could come from the different internal momentum distribution between the two projectiles. As discussed above, the mass dependence of the photon energy spectra slope parameters may also suggest that the high energy photons do not come entirely from the first collision of nucleons.

To summarize, high energy gamma rays produced in light-ion induced reactions are observed in the energy range similar to that of the heavy-ion reactions. Also, photon energies up to a large fraction of the total energy available were observed, as in the proton case. In the light-ion reactions, the slope of the photon energy spectra are much steeper than those found in the heavy-ion induced reactions of similar beam energy/nucleon, and have some weak dependence on both the target and projectile masses as well. The dipole component of the photon angular distribution in the nucleon-nucleon center-of-mass frame are larger than in reactions with heavy-ions and become more pronounced as the masses of the systems decrease.

CHAPTER 5

HIGH ENERGY GAMMA RAY PRODUCTION FROM NEAR SYMMETRIC SYSTEMS

A.Introduction

A.1. The Nucleus-Nucleus Coherent Bremsstrahlung Model

In the introduction of the last chapter, an overview of the current theories of the production of high energy gamma rays in nuclear reactions was outlined. Most of these theoretical models fit in one of three categories: nucleus-nucleus bremsstrahlung, nucleon-nucleon bremsstrahlung, and statistical or thermal emission.

The nucleus-nucleus bremsstrahlung model by Vasak et. al.[Va 85] is one of the early models proposed to explain the production mechanism of high energy photons. This approach distinguishes itself from the majority of the more recent models, which assume a microscopic production mechanism of incoherent nucleon-nucleon bremsstrahlung between individual nucleons. The nucleus-nucleus bremsstrahlung model makes the assumption that the microscopic production mechanism is collective nucleus-nucleus bremsstrahlung. In that model, both the projectile and target nucleus, or a substantial parts of them, act as a whole when they are scattered off one another. That is, all nucleons within the colliding nuclei experience the acceleration field simultaneously. The high energy photons are therefore

produced by the coherent contribution of the bremsstrahlung of the projectile and target nucleus.

For symmetric systems or systems having the same charge-to-mass ratio, the model predicts a quadrupolar angular distribution in the half beam velocity frame. However, later analysis [He 84][Va 86] found that only the coherent bremsstrahlung gamma rays produced out of the reaction plane would be purely quadrupolar, and that the angular distribution averaged over impact parameter would instead be dipolar in nature. While experimental data point to a photon angular distribution containing both isotropic and dipolar components, it is not in strong disagreement with the theory. So the absence of a quadrupolar angular distribution alone is not sufficient to rule out collective bremsstrahlung as the production mechanism.

The coherent model predicts that the magnitude of the gamma ray cross section for symmetric systems to should have a strong Z^2 dependence. The majority of the experiments, consisted of mostly asymmetric systems, agree instead with a differnt scaling law which predicts a mass dependence of roughly $(A_p A_t)^{2/3}$. These observations, while inconsistent with the coherent bremsstrahlung model, are in qualitative agreement with the prediction of models base on incoherent bremsstrahlung mechanism.

Ko et. al. [Ko 85] calculated bremsstrahlung within a cascade calculation. They found that, while incoherent bremsstrahlung dominates in systems having projectile and target mass less than 20, coherent bremsstrahlung should become observable at lower photon energy ($E_\gamma < 40$ MeV) for heavier ($A_p, A_t > 40$), symmetric systems. Therefore, a change of the angular distribution in the center-of-mass frame from isotropic and dipolar

to one with a quadrupole component would be the experimental signature of the onset of the coherent bremsstrahlung.

A.2. The Goal of the Symmetric System Experiment

We have studied in this experiment a series of symmetric or near symmetric systems ranging from light ($^{7}Li + ^{7}Li$) to heavy ($^{40}Ar + ^{40}Ca$) at the same (30 MeV/nucleon) projectile energy. According to the simple first collision bremsstrahlung model [Na86], symmetric systems of different mass A would produce gamma ray spectra of identical characteristics except for different magnitudes. Using the same experimental set-up and the same incident energy, it was possible for us to look for subtle changes, both in angular distributions and in cross sections that may indicate any changes in the gamma ray production mechanism.

Three beams of the same incident energy per nucleon were used for this experiment: 30 MeV/nucleon ^{7}Li, ^{20}Ne and ^{40}Ar. The following 5 reactions were studied: $^{7}Li+Li$, $^{7}Li+Pb$, $^{20}Ne+Mg$, $^{40}Ar+Ca$, $^{40}Ar+Pb$. For the study of the symmetric systems, a 0.21 mm thick Li, a 0.11 mm Mg and a 0.096 mm Ca target were used, respectively. And for comparison, a 0.0254 mm thick lead target was used for both the $^{7}Li+Pb$ and $^{20}Ar+Pb$ reaction. Energy spectra of photons with energies from 20 to 100 MeV were measured at laboratory angle of 30^{0}, 60^{0}, 90^{0}, 120^{0} and 150^{0} using three Cherenkov plastic range telescopes.

B. Experiment Results

Figure V-1 to Figure V-5 show the energy spectra of high energy photons at laboratory angles of 30°, 60°, 90°, 120° and 150° for the three symmetric

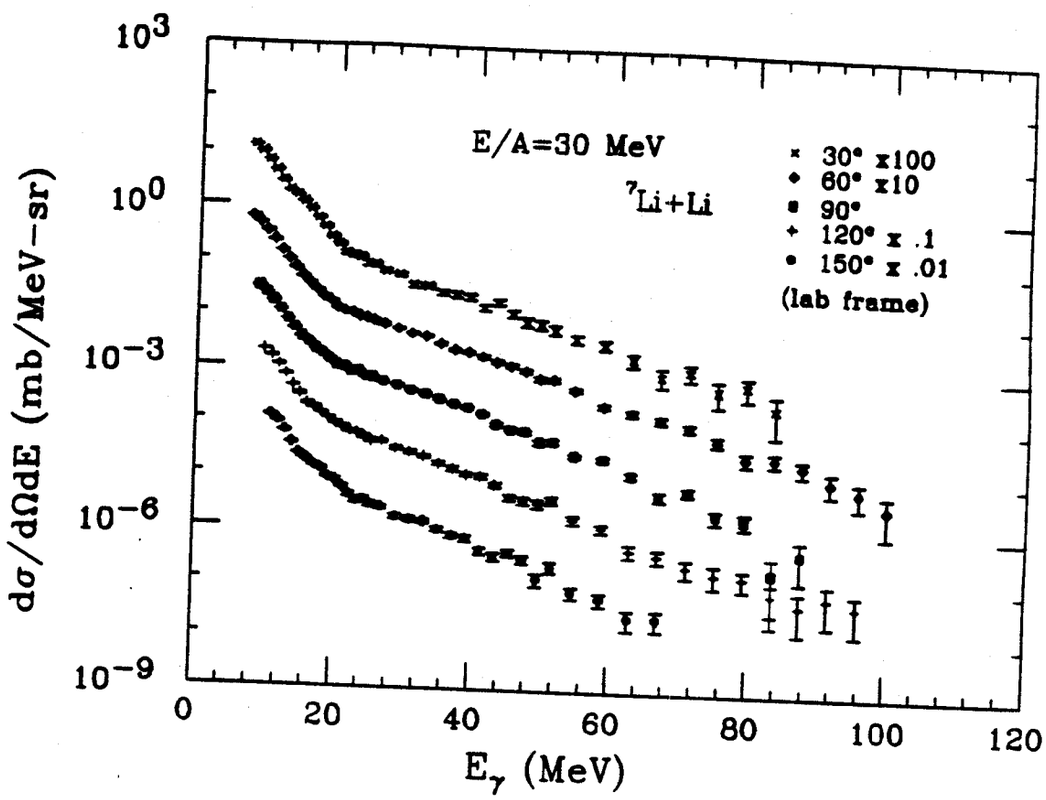

Figure V-1 Photon energy spectra for 30 MeV/nucleon ^{7}Li + Li at laboratory angles of 30°, 60°, 90°, 120° and 150°.

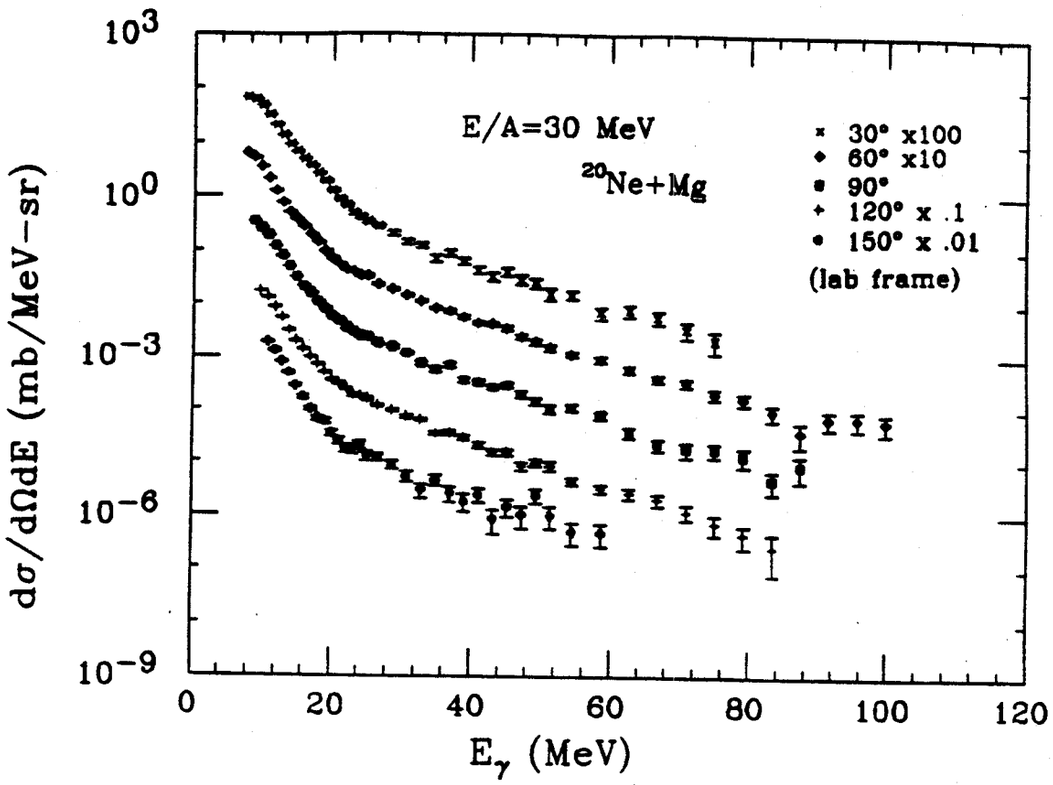

Figure V-2 Photon energy spectra for 30 MeV/nucleon ^{20}Ne + Mg at laboratory angles of 30°, 60°, 90°, 120° and 150°.

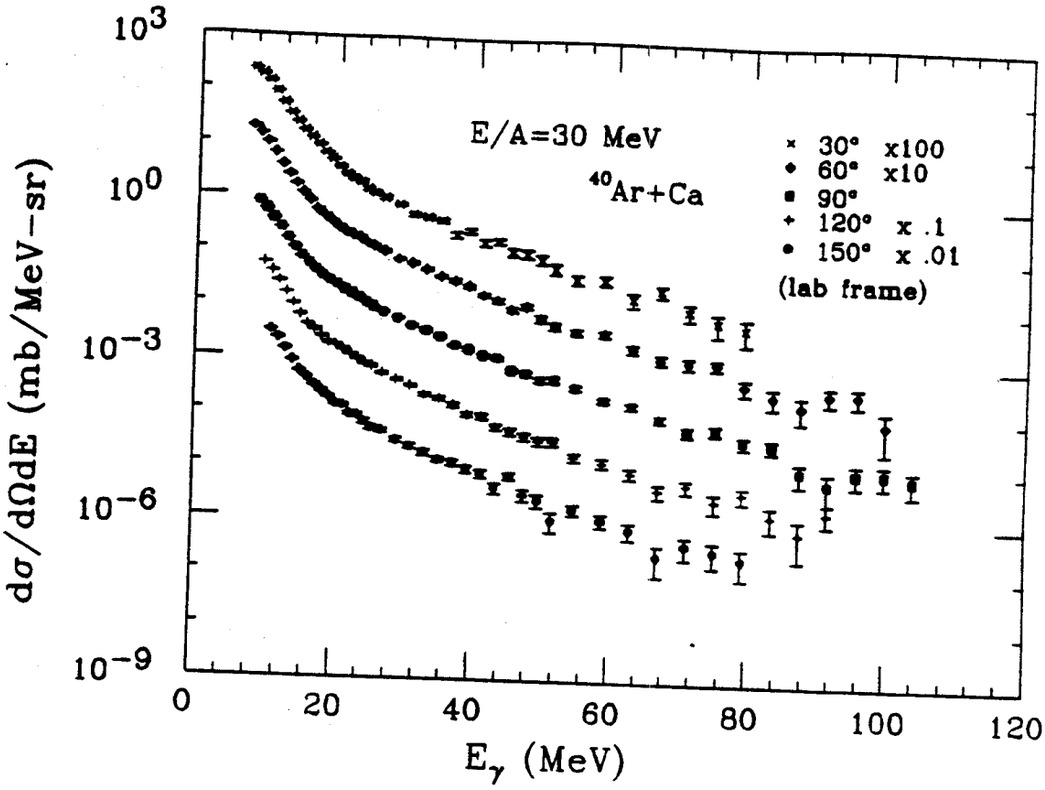

Figure V-3 Photon energy spectra for 30 MeV/nucleon ^{40}Ar + Ca at laboratory angles of 30°, 60°, 90°, 120° and 150°.

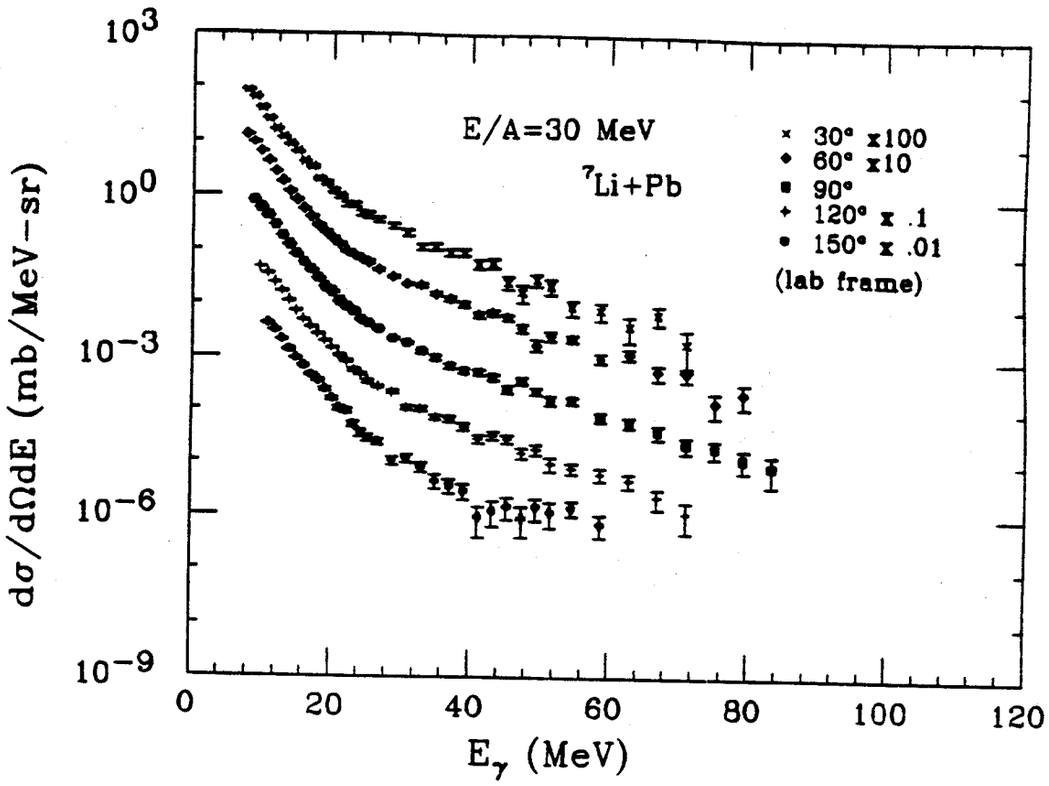

Figure V-4 Photon energy spectra for 53 MeV/nucleon ^{7}Li + Pb at laboratory angles of 30°, 60°, 90°, 120° and 150°.

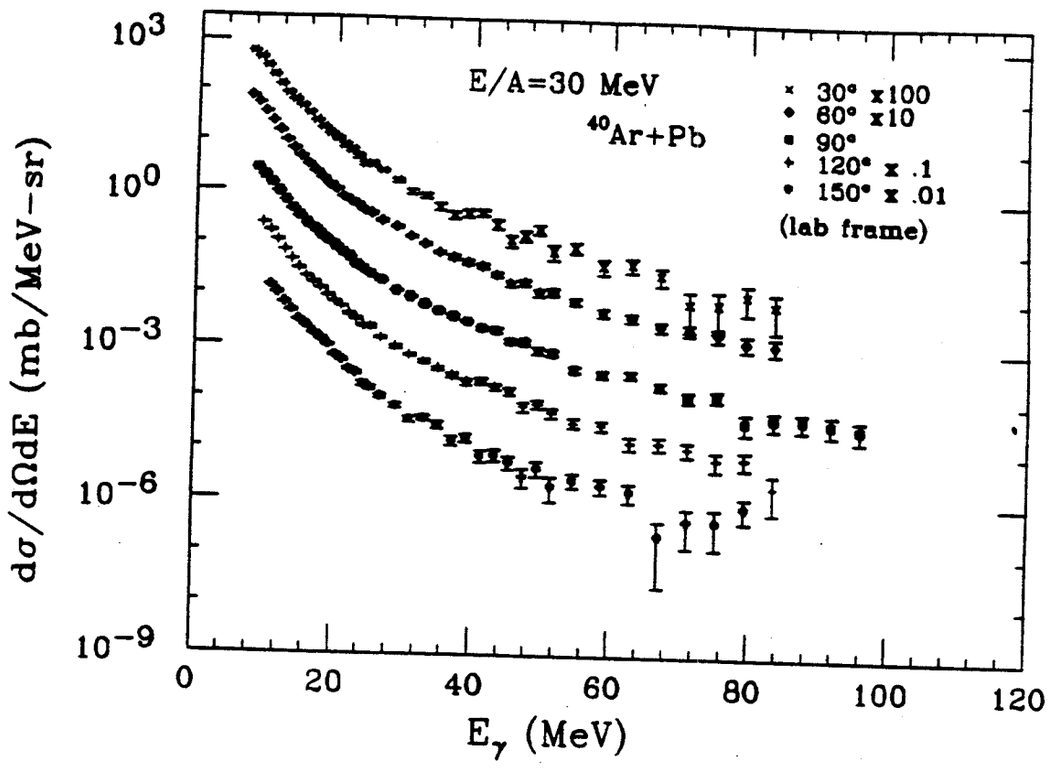

Figure V-5 Photon energy spectra for 53 MeV/nucleon ^{40}Ar + Pb at laboratory angles of 30°, 60°, 90°, 120° and 150°.

systems and the two lead target systems. All of the spectra can be seen to have two regions. The low energy region ($E_\gamma \leq$ 25 MeV), where the spectra are exponentially decreasing with a slope of typically between 2-3 MeV, are thought to be photons coming from statistical decay, giant dipole resonance, as well as bremsstrahlung photons. In the high energy region, $E_\gamma >$ 25 MeV, the spectra are also exponential but with a much flatter slope. We will again concentrate on the "high energy region" of the spectra.

The slopes of the photon energy spectra in the laboratory frame depend on the angles of observation in the lab. The slopes are 'flatter' in the forward angles than those observed in the backward angles. The integrated angular distributions for photon energies above 30 MeV for all five systems are shown in Figure V-6. They are typically forward peaked in the laboratory frame. Therefore, the high energy gamma rays could be coming from a recoiling source. (The relationship between photon energy spectra in the laboratory frame and a source frame moving with velocity β was discussed in chapter 4)

To study better the photon angular dependence, the two dimensional contour rapidity plots discussed in the last chapter were employed to extract the velocity of the recoiling source. The rapidities of a particle moving with velocity $\beta = v/c$ in direction θ in the laboratory frame, $y_{lab} = \frac{1}{2} \ln \left[\frac{1+\beta\cos\theta}{1-\beta\cos\theta}\right] = \frac{1}{2} \ln \left[\frac{1+\beta_{\parallel}}{1-\beta_{\parallel}}\right]$ are plotted both for the symmetric systems and for the lead targets in Figure V-7 and V-8. Here the nearly symmetric nature of the rapidity distributions is again observed. The centroids of the symmetry also appear to be near the rapidity of the nucleon-nucleon center-of-mass frame Y_{NN} in all cases. The quantitative values of fitted centroids,

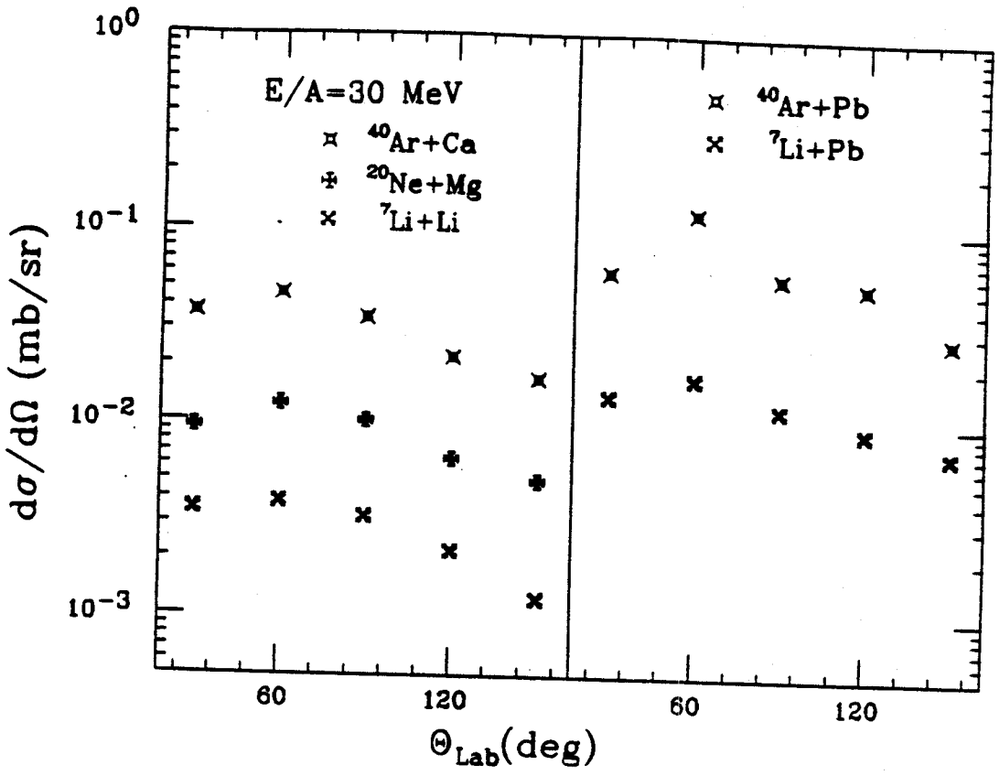

Figure V-6 Integrated angular distributions for photon energies above 30 MeV in the laboratory frame.

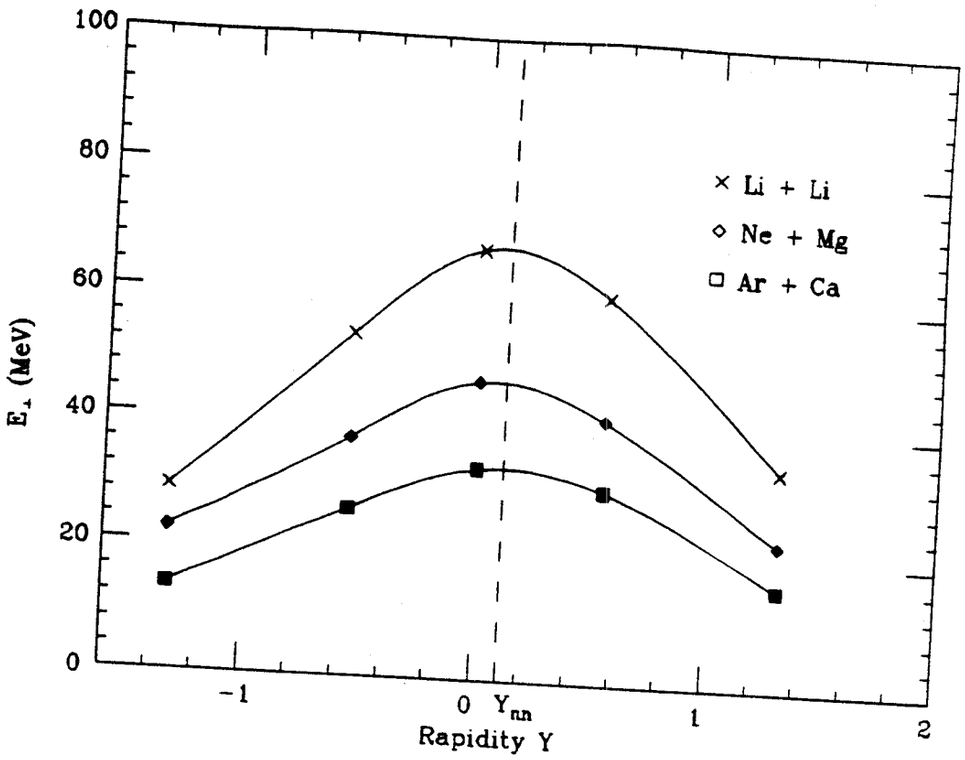

Figure V-7 Rapidity plot for the three symmetric systems.

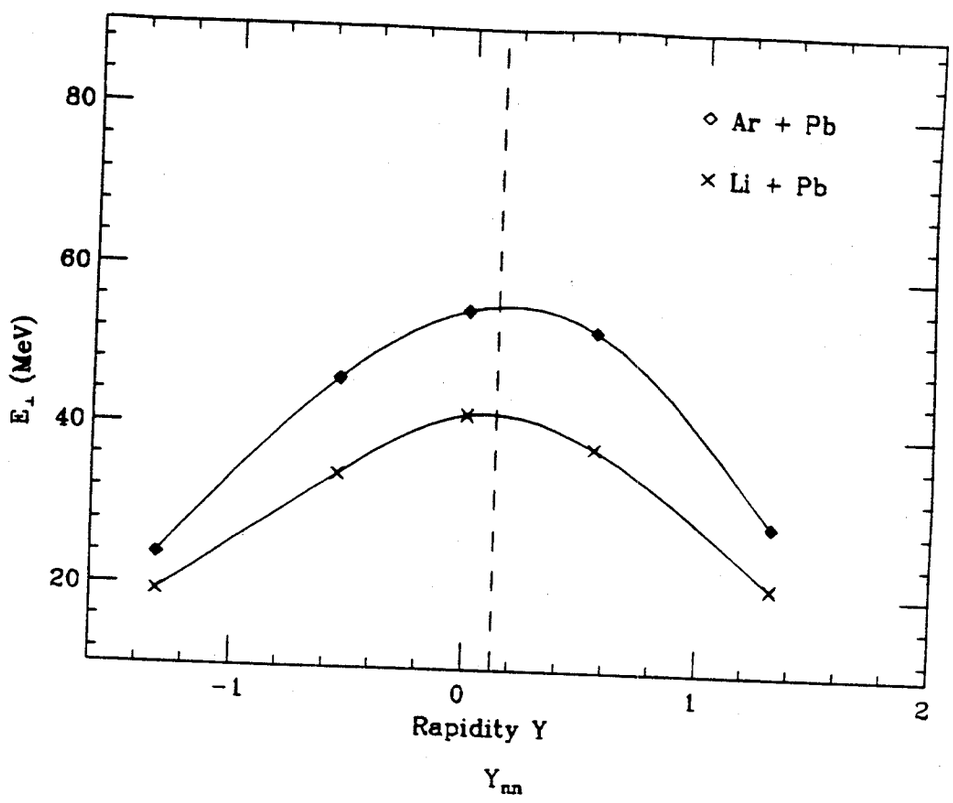

Figure V-8 Rapidity plot for 30 MeV/nucleon ^{7}Li and ^{40}Ar beam on Pb target.

which due to the additive property of the rapidity parameter are the rapidity of the moving source frames assuming Y-ray emission from a single moving source, were obtained by using a cubic spline fit to the rapidity plot. The extracted quantitative values of the emission source rapidities are tabulated in table V-1, together with the nucleon-nucleon center-of-mass velocity for comparison.

It is evident that the source velocities extracted from the measured spectra are rather close to the nucleon-nucleon center-of-mass velocity. Further study of the photon angular dependence can be carried out by transforming the experimental spectra from the laboratory frame to the nucleon-nucleon center-of-mass frame. Figure V-9 contains the Y ray angular distributions in the nucleon-nucleon center-of-mass frame.

C. Discussion

C.1. Systematic Studies of the Data by the Simple Moving Source Fit Model

The photon angular distributions in the center-of-mass frame appear to be fairly symmetric about 90°. All data of the symmetric systems show some evidence of a dipole component superimposed on an isotropic angular distribution. The anisotropy is most pronounced in the lightest system, ^{7}Li + Li. And the ^{7}Li + Pb data also show a rather pronounced dipole component. There is no evidence of any quadrupole component which would otherwise signal the onset of the coherent nucleus-nucleus bremsstrahlung. But as we discussed in the introduction, the absence of quadrupolar angular distributions alone is not sufficient to rule out coherent bremsstrahlung as a possible production mechanism.

Table V-1 The source velocity β_{exp} extracted from the rapidity plot.

BEAM	TARGET	E/A(MeV)	β_{exp}	β_{nn}
^{7}Li	Li	30	0.10	0.126
^{20}Ne	Mg	30	0.09	0.126
^{40}Ar	Ca	30	0.12	0.126
^{7}Li	Pb	30	0.10	0.126
^{40}Ar	Pb	30	0.16	0.126

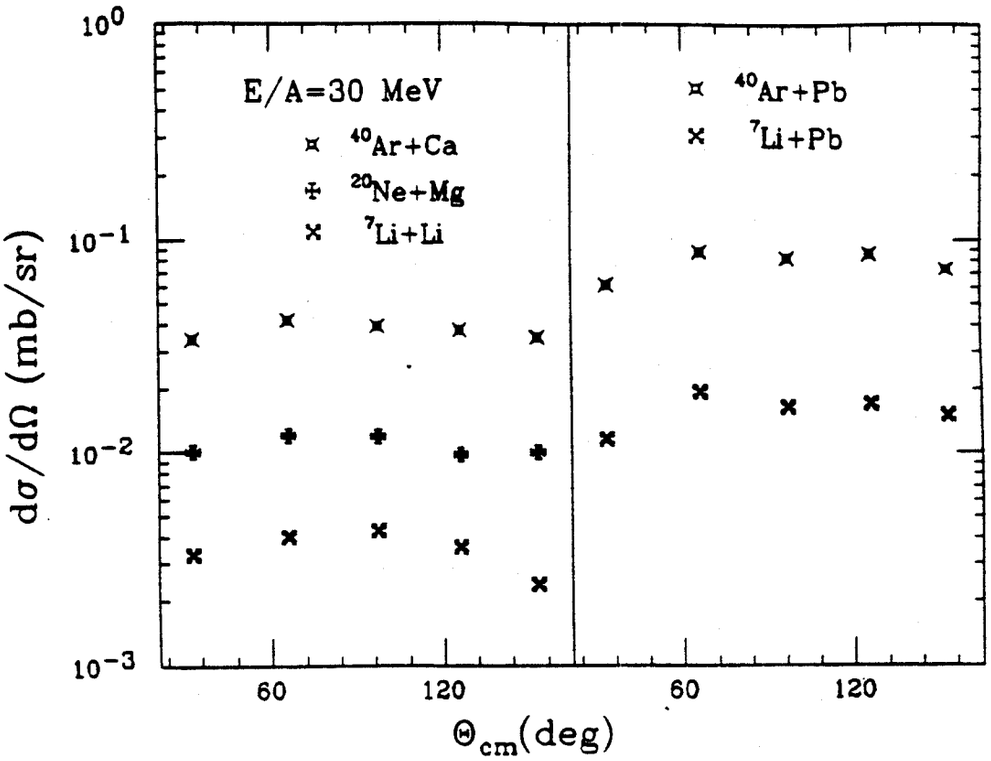

Figure V-9 Integrated angular distributions for photon energies above 30 MeV in the nucleon-nucleon center-of-mass frame.

To study systematically the many interesting features of the measurements, such as the relative strength of the dipole component, the simple moving source model discussed in the last chapter is again used to fit the data. The model assumes that the photon cross section takes the form of $\frac{d^2\sigma}{d\Omega dE} = A\ (1-B\ \cos^2\theta)\ e^{-E/T}$ in the moving source frame, and simultaneously fits to the five energy spectra for each system were made. The best fit values of the following parameters: overall strength A, the relative dipole strength B, slope parameter T and the source frame velocity β_{exp} are shown in Table V-2. The fitted curves for the energy spectra and angular distributions in the nucleon-nucleon center-of-mass are shown in Figure V-10 and V-11.

C.2. Source Velocity of Symmetric and Asymmetric Systems

In table V-2, the nucleon-nucleon center-of-mass velocity β_{NN} is given for comparison with the experimentally extracted source velocities β_{exp} for all the systems studied. The extracted source velocities β_{exp} for the symmetric systems are in good agreement with the nucleon-nucleon center-of-mass velocity β_{NN} within the limit of uncertainty. The source velocities for the lead target data, however, shows a small systematic shift to lower velocities by approximately 0.026c. This small shift may be due to multiple scattering within the colliding nuclei.

For the two asymmetric systems, both involving lighter projectiles bombarding on heavier lead target, only the incoherent sum of the bremsstrahlung photons coming from the first chance individual nucleon-nucleon collision would be symmetric in the nucleon-nucleon center-of-mass

Table V-2 Results of the moving source model fit to all 5 systems

BEAM	TARGET	E/A(MeV)	β_{exp}	β_{nn}	T(MeV)	A (mb/MeV-sr)	B
^{7}Li	Li	30	0.12±0.01	0.126	9.0±0.2	0.014±0.004	0.48±0.09
^{20}Ne	Mg	30	0.13±0.01	0.126	8.8±0.2	0.041±0.012	0.32±0.07
^{40}Ar	Ca	30	0.11±0.01	0.126	8.3±0.2	0.18±0.05	0.29±0.05
^{7}Li	Pb	30	0.10±0.01	0.126	7.9±0.2	0.10±0.03	0.49±0.10
^{40}Ar	Pb	30	0.10±0.01	0.126	7.4±0.2	0.66±0.20	0.36±0.06

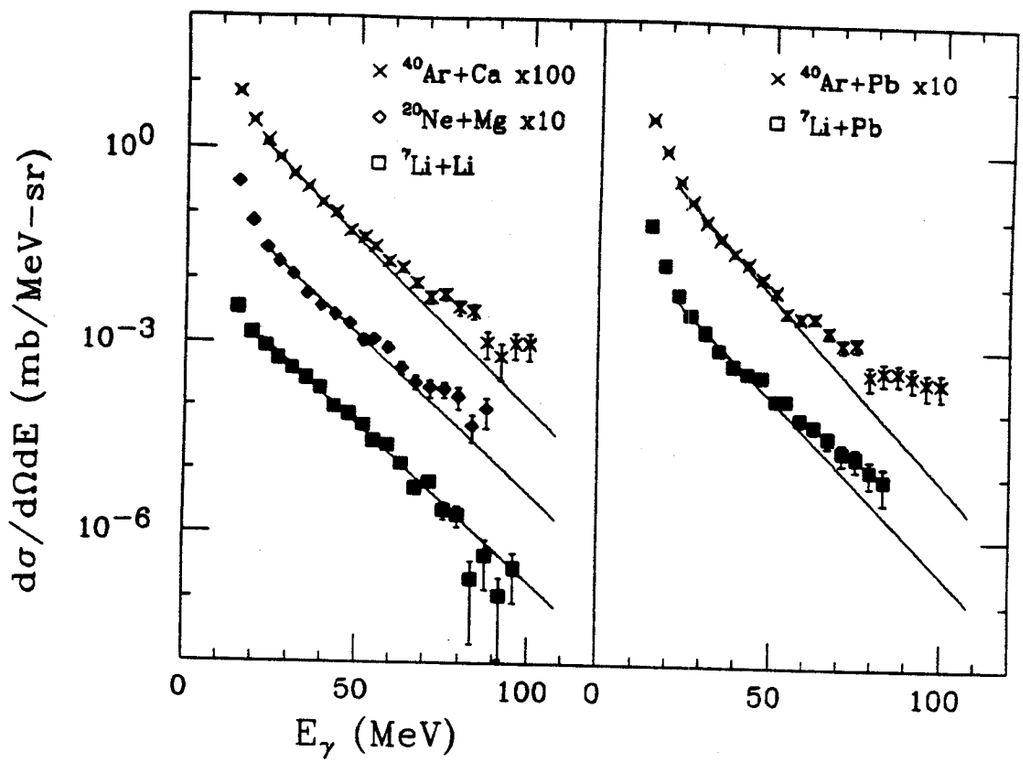

Figure V-10 Moving source model fit to the photon energy spectra at 90° in the laboratory for all 5 reactions studied.

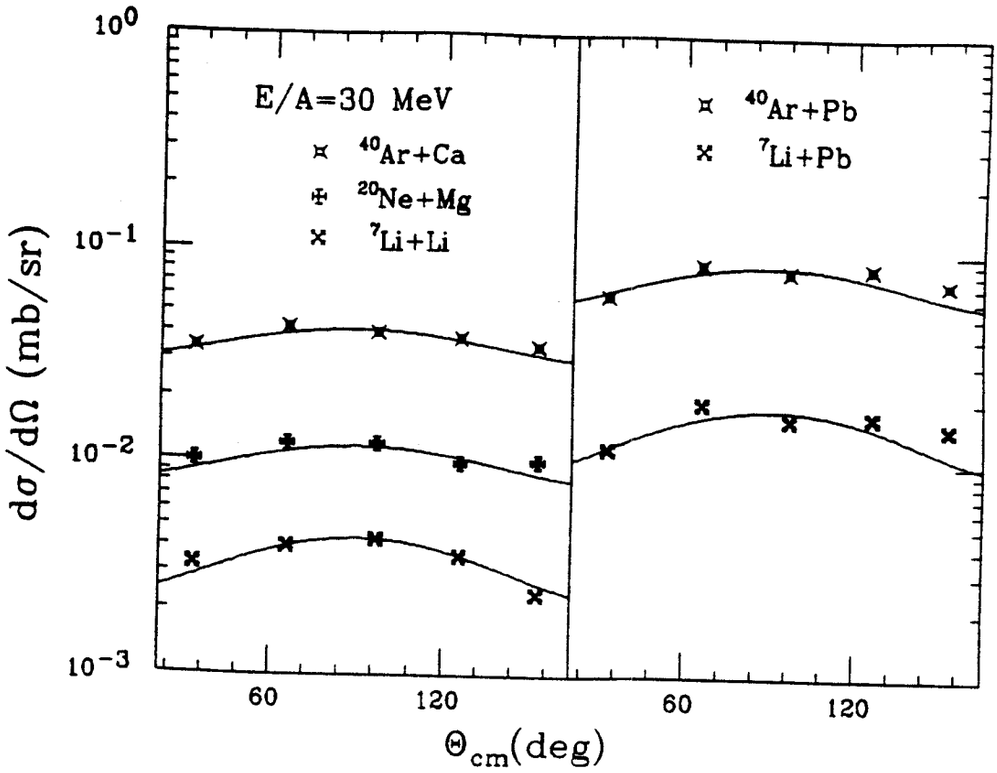

Figure V-11 Moving source model fit to the photon integrated angular distributions in the nucleon-nucleon center-of-mass frame.

frame. Subsequent scatterings, on the other hand, would contribute to this slight lowering of the source velocities.

For the symmetric systems, the nucleon-nucleon center-of-mass and the nucleus-nucleus center-of-mass are identical. Therefore, bremsstrahlung photons from both the first chance nucleon-nucleon collision and subsequent scatterings are expected to be symmetric in this common frame.

C.3. Mass Dependence of the Photon Angular Distributions in Center-of-Mass Frame

There have been reports [Gr 86][Be 87] of small dipole components present in the angular distribution of the high energy bremsstrahlung photons. The relative strength of the dipole component reported by Bertholet et al. [Be 87] ranges from 16% to 31% for 44 MeV/n ^{86}Kr induced reactions. The values for our symmetric systems range from about 29% for ^{40}Ar + Ca to 48% for ^{7}Li + Li, and 36% to 49% for ^{40}Ar + Pb and ^{7}Li + Pb respectively (table V-2). The dipole component appears to decrease with increased system size. The values obtained here are also consistent with our finding from the light-ion induced reactions (discussed in chapter 4) and the finding by Bertholet et al. [Be 87]. For comparison, a relative dipole strength of B=60% for the elementary np bremsstrahlung is predicted in the nonrelativistic long wavelength approximation; the values of B found here range from 50% to 80% of that of the free np bremsstrahlung.

The dependence of the dipole components on target masses may be associated with the multiple scattering between individual nucleons within the colliding nuclei. Only the nucleon-nucleon bremsstrahlung from the first collision can have dipolar angular distribution in the center-of-mass frame;

bremsstrahlung photons produced in subsequent collision no longer bear any clear signature of the initial beam direction, and would therefore be isotropic in the center-of-mass frame. Thus, the increased contribution of multiple scattering in larger systems can lead to a more isotropic angular distribution.

C.4. Mass Dependence of the Photon Energy Spectra

C.4.1. Slope Parameters of the Double Differential Cross Sections

Table V-2 also shows other parameters of the photon energy spectra extracted using the simple moving source model for all the systems studied. They are in general in good agreement with other published data of similar systems. Kwato et al. [Kw 86] had studied high energy gamma ray production from $^{40}Ar + ^{197}Au$ at the same incident energy of 30 MeV/nucleon. They reported a slope parameter of around 7.5 MeV, while the slope parameter for our similar system of $^{40}Ar + ^{208}Pb$ was found to be 7.4±0.2 MeV. The magnitude of the cross section are in rather good agreement as well.

The slope parameters of the energy spectra of the two lead target data are both smaller than that of the corresponding symmetric target data by about 1 MeV, as can be seen in table V-2. Although the slope parameters of the energy spectra of symmetric systems are quite similar, they also decrease slightly as the size of the system increases. A qualitative explanation of this size dependence can be that bremsstrahlung photons produced during first collisions are more likely to be of higher energy than those produced in subsequent collisions. Therefore, larger systems which would have higher probabilities of multiple collisions produce a slightly larger portion of the bremsstrahlung photons from multiple scattering; there

are more photons in the low energy end of the spectra making the spectrum steeper.

C.4.2. Total Cross Section Ratios

An interesting feature of the data is the mass dependence of the total cross sections. Different theories predicted different mass or charge dependences of systems having the same projectile energy/nucleon. The coherent bremsstrahlung model by Vasak et al. [Va 86] predicted a nuclei charge dependence of roughly Z^2. Most of the experimental data, however, did not show such charge dependence. Instead, a phenomenological scaling law assuming photon cross sections proportional to the product of the projectile and target geometrical cross sections, i.e. $\sigma_\gamma \sim (A_t A_p)^{2/3}$ was found quite successful.

A scaling scheme based on first collision incoherent nucleon-nucleon bremsstrahlung was proposed by Nifenecker and Bondorf [Ni 85], which suggests the gamma ray total cross section following the relation:

$$\sigma_\gamma = P_\gamma \langle N_{np} \rangle \sigma_R,$$

They found the probability of emitting a photon per proton-neutron collision P_γ is nearly constant in collisions at beam energies 20 - 85 MeV/nucleon. Thus, the bremsstrahlung cross section should be proportional to the product of the total reaction cross section σ_R and the impact-parameter-averaged number of first chance n-p collisions $\langle N_{np} \rangle$. By assuming uniform density nuclei of radii $R=1.2\ A^{1/3}$ fm, both quantities σ_R and $\langle N_{np} \rangle$ can be easily calculated as follows:

$$\sigma_R = \pi\,(1.2A^{1/3} + 1.2A^{1/3})^2$$

$$\langle N_{np}\rangle = A_p \frac{5A_t^{2/3} - A_p^{2/3}}{5(A_p^{1/3} + A_t^{1/3})} = \frac{\langle A_F\rangle}{A_p A_t}\,(Z_p N_t + Z_t N_p)$$

where $\langle A_F\rangle$ is the average mass of the participant zone (the projectile and target overlap area, assuming $A_p \leq A_t$).

The experimental total cross sections are obtained by integrating over 4π for photons above 30 MeV energy using the fit parameters. The ratio of total cross section for the symmetric systems are ^{7}Li+Li:^{20}Ne+Mg:^{40}Ar+Ca = 1:2.8:9.6 (Table V-3). Also listed in table V-3 for comparison are the prediction of the coherent model, prediction of the simple $(A_pA_t)^{2/3}$ scaling rule, and the prediction base on first collision nucleon-nucleon model by Nifenecker and Bondorf [Ni 85].

One can see clearly from the table that the experimental ratios deviate substantially from the prediction of the coherent bremsstrahlung model. And it appears the simple $(A_pA_t)^{2/3}$ scaling is in better agreement with the experimentally observed ratio than the prediction of the first collision model.

D. Summary

The high energy gamma rays produced in 30 MeV/nucleon heavy ion induced reactions have angular distributions symmetric about 90° in the nucleon-nucleon center-of-mass frame. There is no evidence of quadrupole components in their angular distributions. Instead, all of the reactions we studied show a dipole component superimposed on an isotropic component. The relative

Table V-3 Ratios of total cross section predicted by different models in comparison with experimetnal data.

SYSTEM	$RATIO_{exp}$	$RATIO_{coh}$ (Z^2)	RATIO $(A_t A_p)^{2/3}$	RATIO $P_\gamma \langle N_{np} \rangle \sigma_R$
$^{7}Li+Li$	1	1	1	1
$^{20}Ne+Mg$	2.8	11	4.6	6.6
$^{40}Ar+Ca$	9.6	44	10.2	19.0

strength of the dipole component range from 29% to 49%, and we found a trend of increased dipole components with decreasing masses of the systems. The mass dependence of the relative dipole strength may be due to the increased contribution of multiple scattering within the colliding nuclei.

We were also able to extract the velocity of the recoiling photon emission source. They are in general in agreement with the nucleon-nucleon center-of-mass frame. While the source velocity of the two reactions with lead targets are slightly shifted to the lower side, it may be due to the increased probability of second or third chance collisions from the relatively large mass of the lead target.

The slope parameters obtained for all our systems studied are in general agreement with data at the same energy measured by other groups with similar systems. We have also observed some weak mass dependence of the slope parameter, which may again be due to the contribution of the multiple scattering. With the increased mass of the systems, there appears to be an increased contribution from the later stage of the collision process. The integrated photon cross sections for gamma ray energy above 30 MeV are in better agreement with the simple $(A_p A_t)^{2/3}$ scaling scheme than with the first collision bremsstrahlung model. The ratios of the bremsstrahlung photon total cross section provide no evidence to support the Z^2 charge dependence predicted by the coherent bremsstrahlung model.

Chapter 6

Theoretical Model Calculations and Comparison with Data

A. Introduction

Many different theoretical models have been advocated to explain the high energy gamma ray production in nucleus-nucleus reactions. Most of the models can be categorized into three different basic approaches:

i) The nucleus-nucleus coherent bremsstrahlung approach:

In this approach, the photons are thought to be produced at the early stage of the collision by the coherent bremsstrahlung of the projectile and target nucleus acting as a whole. This model predicts quadrupolar photon angular distributions and a Z^2 charge dependence of cross section magnitudes.

ii) The nucleon-nucleon incoherent bremsstrahlung approach:

These models assume a production mechanism of incoherent bremsstrahlung from individual neutron-proton collisions within the colliding nucleus at the early stage of the reaction. They predict a superposition of isotropic and dipolar angular distributions and an $A^{2/3}$ mass dependence for the magnitude of the cross section.

iii) Thermal model:

In this approach, a 'fireball' or hot zone is formed from the colliding projectile and target nucleus, and photons are emitted from this recoiling hot system at the later stage of the reaction. These models predict isotropic angular distributions and cross sections that depend on the total energy of the projectile.

In the two experiments described in the previous chapters, we measured high energy gamma rays coming from light-ion induced reactions and reactions involving symmetric systems. In our data, we did not observe any evidence of quadrupolar angular distribution. We found that the high energy photon angular distributions consisted of a dipole component on top of an isotropic distribution. In the light-ion induced experiment, the very different features observed for systems having similar total energy indicates that the thermal model is unlikely to be the main origin of the high energy photons. In the experiments with symmetric systems, the ratio of the gamma ray yield, which follows the simple scaling rule of $A^{2/3}$, also suggests first chance np collisions is a major source of high energy gamma rays.

Experimental results covering a wide range of systems (from p+d to ^{136}Xe+Sn) and projectile energies (10 - 125 MeV/nucleon) are available. Most of these show isotropic or dipolar angular distributions in the nucleon-nucleon center-of-mass frame. The success of the $A^{2/3}$ dependence of the cross section indicates that the incoherent neutron-proton collisions in the early stage of the reaction are the main source of these high energy gamma rays.

A variety of incoherent nucleon-nucleon collision models have had some success in explaining the major trends of the experimental results. Many of

them were able to reproduce some of the data sets. In this chapter, we will compare some of the model calculations with the data we obtained.

B. BUU Calculation.

Bauer et al.[Ba 86] introduced an incoherent nucleon-nucleon collision model that contains a complete nucleon-nucleon collisional history of the system. Using the BUU (Boltzmann-Uehling-Uhlenbeck) equation, which describes the time evolution of the nucleon phase space density distribution during the nucleus-nucleus reaction, the model enables a dynamical study of the reaction process in both momentum and coordinate space. The elementary process for gamma ray production is assumed to be the classical individual neutron-proton bremsstrahlung, modified to take into account the energy loss of the nucleons after the production of the high energy photon. They found, by following the time evolution of the gamma emission process, that gamma rays are produced in the early stage of the collision process. Photon production cross sections and angular distributions of a wide range of experiments were satisfactorily reproduced.

B.1. Comparison with the Symmetric Systems Data

Figure VI-1 shows the results of the BUU calculation of the photon energy spectra at 90° laboratory angle for the symmetric systems and systems of Pb targets in comparison with the data. The spectra of the ^{20}Ne + Mg and ^{7}Li + Li were obtained by summing over the results of BUU calculations performed at 1 fm interval of the impact parameter. To calculate the other heavier systems requires significantly more computer time, so a slightly different scheme was employed. The calculation

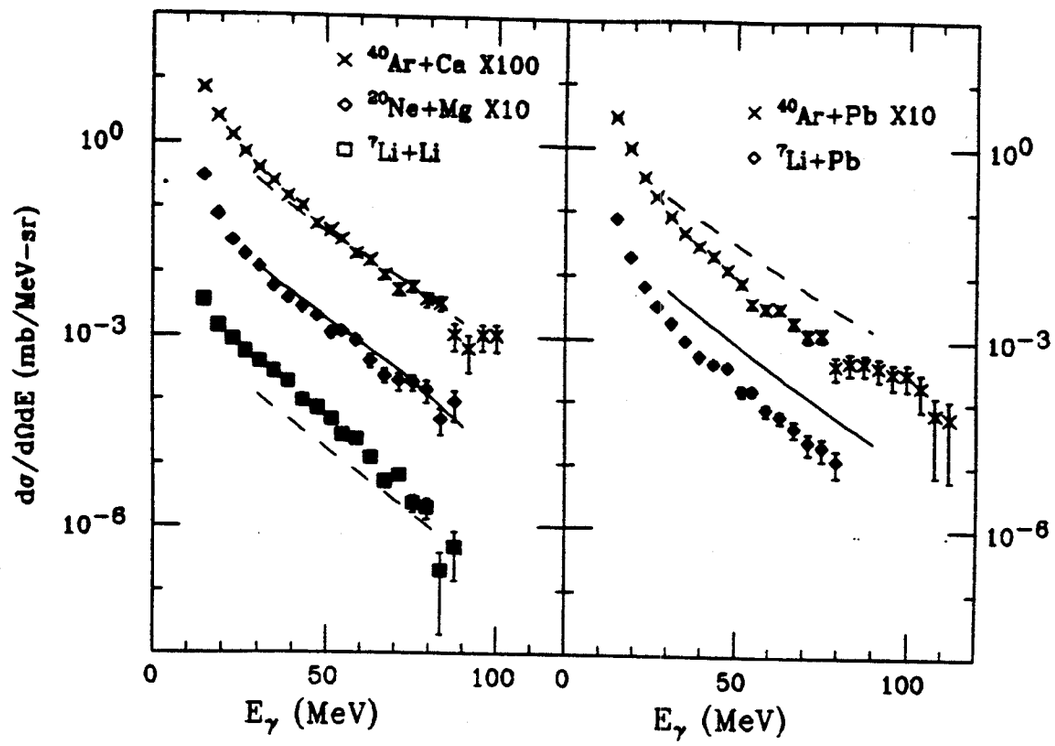

Figure VI-1 Comparison of BUU calculation of the photon energy spectra with experimental data of the symmetric systems.

was done at zero impact parameter to obtain the probability for gamma ray production, then the probability at other non-zero impact parameters were assumed to be nearly proportional to the geometrical overlap area of the two circles having the same radii of the colliding nuclei. For near symmetric systems ($A_p \sim A_t$), the maximum overlap area of two circles of radius $R \sim A_p^{1/3} \sim A_t^{1/3}$ at impact parameter b is [Ba 86]:

$$S(b)=[2R^2\cos^{-1}(b/2R) - b(R^2 - b^2/4)^{1/2}]/\pi R^2 \qquad \text{(VI-1)}$$

And for asymmetric systems of $R=A_t^{1/3}$ and $r=A_p^{1/3}$, the overlap area will be:

$$S(b)=[R^2\cos^{-1}(\frac{b^2+ R^2- r^2}{2bR}) - \frac{R}{2b}(b^2+ R^2- r^2)(1- \frac{b^2+ R^2- r^2}{2bR})^{1/2}$$

$$+ r^2\cos^{-1}(\frac{b^2+ r^2- R^2}{2br}) - \frac{r}{2b}(b^2+ r^2- R^2)(1- \frac{b^2+ r^2- R^2}{2br})^{1/2}]/\pi R^2$$

The agreement between the model and data for ^{40}Ar + Ca and ^{20}Ne + Mg are quite good, but the calculation underestimates the magnitude of cross section for the ^{7}Li + Li spectra by approximately a factor of 3. For the Pb target cases, the calculation overestimates the cross section of ^{7}Li + Pb and ^{40}Ar + Pb by a factor of 3 to 4. Some of the discrepancy in reproducing the Pb targets data may come from the use of the zero impact parameter and the scaling of the non-zero impact parameters. The scaling (formula VI-1) of production cross section in proportion to overlap area was found valid by Bauer et al. [Ba 86] for relatively light projectile and target nuclei (A~12). It may not necessarily be the appropriate scaling rule for the heavy-target nuclei systems studied here.

Figure VI-2 shows the angular distribution in the nucleon-nucleon center-of-mass frame for the symmetric systems and the Pb targets data in comparison with the prediction of the model. Probably due to the poor agreement in the energy spectra, the magnitudes of the integrated cross sections for the ^{7}Li + Li and the two Pb targets are not very well reproduced. To bring the curves into the similar scale for ease of comparison, the BUU curve for the ^{7}Li + Li data has been shifted by a factor of 3, and the curves for the two Pb target data by a factor of 0.25.

The calculation reproduces reasonably well the shapes of the high energy photon angular distribution for the symmetric systems, but it underestimates the dipole component in the ^{7}Li + Li reaction. This may be due to an overestimation of photons originated from multiple scattering. For the Pb target reaction data, however, the model failed to reproduce the shape of the photon angular distribution. The results of the calculation were noticeably backward peaked in the nucleon-nucleon center-of-mass frame. This may originate from an overestimation of gamma ray production in the later stage of the reaction which come, on the average, from a slower moving "source" than the nucleon-nucleon center-of-mass frame. However, some of the discrepancy may have come from the breaking down of the simple geometrical scaling of the zero impact parameter calculations.

B.2. Comparison with the Light-Ion Induced Reactions

Figure VI-3 shows the results of BUU calculation for photon energy spectra at laboratory angle of 90° for carbon target data and the integrated cross sections for photons having energies over 30 MeV. The calculation reproduces the energy spectrum for 53 MeV/nucleon ^{4}He + C reasonably well.

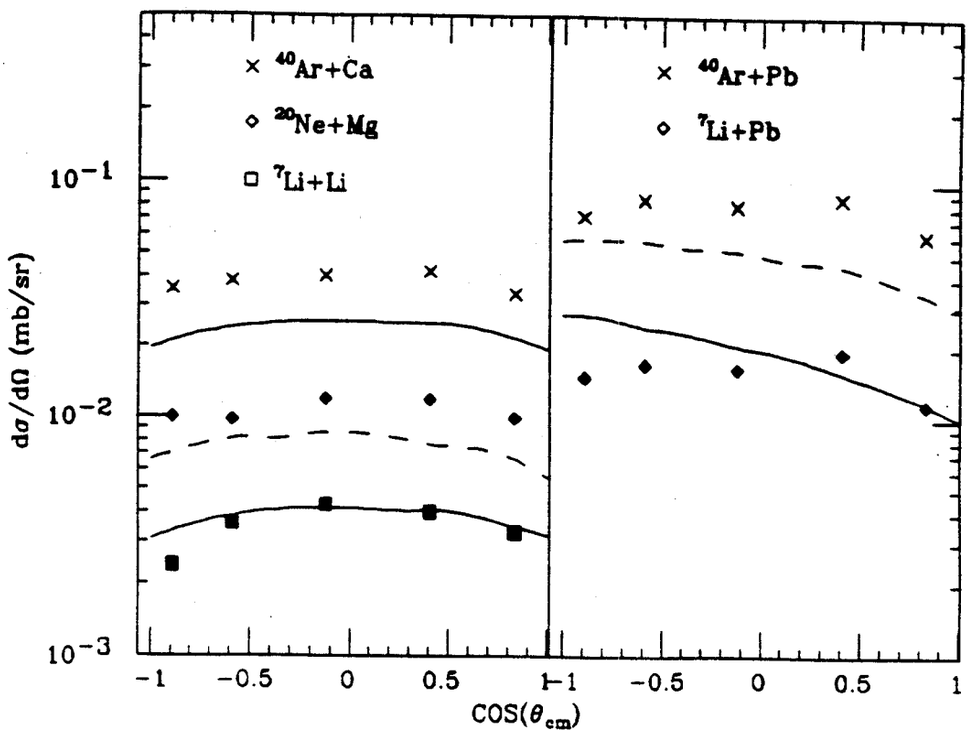

Figure VI-2 Comparison of BUU calculation of the photon angular distributions in the nucleon-nucleon center-of-mass frame with experimental data for the symmetric systems.

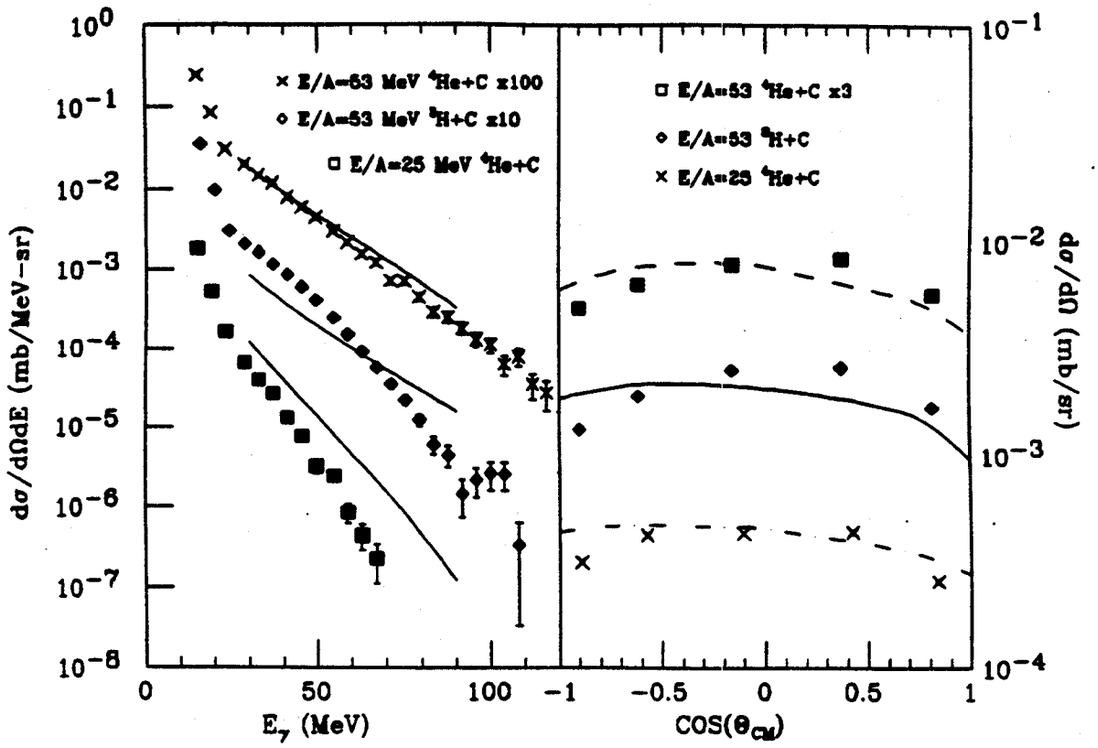

Figure VI-3 Comparison of BUU calculation with experimental data of the light-ion induced reactions systems for both the photon energy spectra and angular distributions in the nucleon-nucleon center-of-mass frame.

However, the predicted slope for the 53 MeV/nucleon ^{2}H + C data is flatter than the experimental result, while the prediction for the cross section for the 25 MeV/nucleon ^{4}He + C is a factor of 2 to 3 too large. Part of the discrepancies may come from the use of a uniform density distribution with radii of $R=1.12A^{1/3}$, which is appropriate for large nuclei, for the light projectile nucleus. Also, the Fermi momentum may not describe the internal momentum distribution of light-ion projectile properly. In addition, the treatment of the Pauli blocking of the final state phase space is adequate only for photon energies up to about 80% of the total available energy. Therefore, results for photons having energy near the kinematical threshold would not be expected to be valid.

The agreement between the BUU calculation and experimental data for the magnitude of the 53 MeV/nucleon ^{4}He + C reaction cross section is reasonably good. But the model under-predicts the 53 MeV/nucleon ^{2}H + C data and over-predicts in the case of 25 MeV/nucleon ^{2}H + C, probably due to the discrepancy in the energy spectra calculations. The calculated curves for the 53 MeV/nucleon ^{2}H + C and ^{4}He + C in Figure VI-3 have been scaled by factors of .33 and 2 respectively for ease of comparison.

However, the model predicts a backward peak for the angular distribution in the nucleon-nucleon center-of-mass frame. This may again, as mentioned in the previous section, be due to an overestimation, particularly for light-ion induced reactions, of gamma rays coming from multiple scattering. The model also underestimates the relative strength of the dipole components in the angular distribution, especially in the E/A = 53 MeV ^{2}H + C case. This is consistent with the overestimation of gamma ray yields from subsequent collisions. So, the use of parameters appropriate for

large nuclei in the calculation may be an important contributing factor to the discrepancy between the prediction and data on the light-ion induced reaction.

C. Simple Fermi Gas Model First-Chance np Collision Bremsstrahlung Calculations for 53 MeV Light-Ion Data

C.1. First Chance Bremsstrahlung Model for Light-Ion Induced Reactions

Due to the limitation of the BUU model discussed in the previous section, the calculation did not reproduce the slope and the magnitude of the photon energy spectra for the light-ion induced reactions. As we mentioned in chapter IV, one interesting feature of light-ion induced bremsstrahlung photon spectra is the projectile dependence. Unlike the heavy-ion induced reaction where projectiles having similar E/A have rather similar behavior except in overall magnitude of the photon yield which follows a simple $(A_t A_p)^{1/3}$ rule, the slope parameters of ^{2}H and ^{4}He induced bremsstrahlung photon production cross section are substantially steeper than heavy-ion induced reactions at similar energy (shown previously in Chapter IV, Table IV-4). Also, the slope parameters of the photon energy spectra for the 53 MeV/nucleon ^{2}H + Pb and ^{4}He + Pb, too, are noticably different. Part of the difference may be coming from their unique internal momentum distribution, which is clearly different from the Fermi sphere distribution commonly used to describe that of the heavy-ions. In this section, we will investigate the role of internal momentum distribution within light-ion projectiles in the production cross section of high energy gamma rays using a simple first collision np bremsstrahlung model developed by K. Nakayama and G. Bertsch.

In this model, the target nucleus is characterized as a sphere both in configuration and momentum space. The elementary cross section for photon production is assumed to be the semi-classical bremsstrahlung cross section. The bremsstrahlung rate is given by the second order formula of perturbation theory: [Na 86]

$$dW_{npY} = 2\pi\left|\langle\psi_{ij}0|j\cdot A\,\frac{1}{E_i-H_o}V + V\,\frac{1}{E_i-H_0}j\cdot A|\psi_{fj}q\rangle\right|^2(dn_f dn_q/dE)$$

Here V is the residual interaction between two particles. The interaction was assumed to be only a function of the spacial separation between the neutron and proton, independent of the energy and momentum transfer, i.e.

$$V=v_o\delta^3(r_p-r_n)$$

In this calculation, v_o = 50 MeV.

Momentum conservation reduces the sum over intermediate states j to a single term in the plane wave representation. The subscripts 1, 2, 3, and 4 denote the energy (or momentum) of the initial proton, initial neutron and that of the final proton and final neutron.

$$\frac{d^2W}{d\omega d\Omega} = \frac{\alpha v_0^2}{2\pi\omega}\,g\int_{<k_F}\frac{d^3p_2}{(2\pi)^3}\int\frac{d^3p_3}{(2\pi)^3}\,Q\delta(\varepsilon_1+\varepsilon_2-\varepsilon_3-\varepsilon_4-\omega)\Sigma\left|\frac{\hat{\varepsilon}\cdot v_3}{1-\hat{k}\cdot v_3}-\frac{\hat{\varepsilon}\cdot v_1}{1-\hat{k}\cdot v_1}\right|^2$$

Q is the Pauli blocking operator. For single nucleon projectile, Q simply takes into account the target Fermi sphere:

$$Q=\Theta(p_3-p_F)\Theta(p_4-p_F)$$

The total collision rate is given by

$$W_{pn}=2\pi|\langle\psi_i|V|\psi_f\rangle|^2\,\frac{dn}{dE^f} = 2\pi v_0^2 g\int_{<k_F}\frac{d^3p_2}{(2\pi)^3}\int\frac{d^3p_3}{(2\pi)^3}\,Q\delta(\varepsilon_1+\varepsilon_2-\varepsilon_3-\varepsilon_4)$$

If we assume pp collisions are just as likely as pn collisions, the differential cross section for np bremsstrahlung is:

$$\frac{d^2P}{d\omega d\Omega} = \frac{1}{2W_{pn}}\frac{d^2W}{d\omega d\Omega}pnY$$

In the simplest approach, only the first collisions are considered. After the first collision, the projectile nucleon loses some of the energy, and its probability of making high energy photon in subsequent collisions is thus reduced drastically. The model was able to reproduce satisfactorily the p + Be data of Edgington and Rose [Ed 66].

In the light-ion induced bremsstrahlung, photons can be produced when the protons in the projectile interact with the neutrons in the target, or when the neutrons in the projectile collide with the protons in the target. So, to make use of this proton-nucleus model to calculate photon production cross section in ^2H induced reaction, we considered the ^2H nucleus a collection of 1 proton and 1 neutron, each of them have a probability $f_H(p)$ of having a particular internal momentum p. Then the photon production cross section is obtained by integrating over all the possible values of the

internal momentum distribution for the proton (or the neutron) inside the ^2H nucleus:

$$\left.\frac{d^2P}{d\omega d\Omega}\right|_H = 2\int d^3p f_H(p)\frac{d^2P(p)}{d\omega d\Omega}_{npY} = 2\int d^3p |\psi_H(p)|^2 \frac{d^2P(p)}{d\omega d\Omega}_{npY}$$

And for ^4He, the cross section is:

$$\left.\frac{d^2P}{d\omega d\Omega}\right|_{He} = 4\int d^3p f_{He}(p)\frac{d^2P(p)}{d\omega d\Omega}_{npY} = 4\int d^3p |\psi_{He}(p)|^2 \frac{d^2P(p)}{d\omega d\Omega}_{npY}$$

Where the distribution of $f_{He}(p_1)$ is different from the distribution inside the ^2H, $f_H(p_1)$, and is the relevant parameter whose role we hope to investigate using this model.

C.2. The Internal Momentum Distribution of ^2H and ^4He

C.2.1. Internal Momentum distribution of ^2H

A simple analytical form of the ^2H wave function in coordinate space is given by the Hulthen wave function [De 67]:

$$\psi(\vec{r}) = [N(r)]^{-1/2}\left(\frac{e^{-r/R} - e^{-r/\rho}}{r}\right)$$

where N(r), is the normalization factor $2\pi(R+\rho-4R\rho/R\rho)$

Here R(= 4.31 fm), the "radius" of deuteron, is a real quantity, and $\rho \approx R/7$ as indicated by experiment[De 67]. The wave function falls off exponentially at large r.

To express the wave function in momentum space, we make a Fourier transform of the wave function from coordinate space to momentum space:

$$\psi(\vec{k}) = (2\pi)^{-3/2} \int d^3r\ \psi(r)\ e^{-i\vec{k}\cdot\vec{r}}$$

$$= (2\pi N(r))^{-1/2} 2\left[\frac{1}{k^2+1/R^2} - \frac{1}{k^2+1/\rho^2}\right]$$

The ^2H induced bremsstrahlung probability is then calculated by integrating over the momentum space:

$$\left.\frac{d^2P}{d\omega d\Omega}\right|_H = 2\int d^3p f_H(p)\ \frac{d^2P(p)}{d\omega d\Omega} npY$$

$$= 2\int d^3k\ \frac{1}{2\pi N(r)}\ \left[\frac{1}{k^2+1/R^2} - \frac{1}{k^2+1/\rho^2}\right]^2 \frac{d^2P(p)}{d\omega d\Omega} npY$$

$$= 2\int d\Omega \int dk\ k^2\ \frac{1}{2\pi N(r)}\ \left[\frac{1}{k^2+1/R^2} - \frac{1}{k^2+1/\rho^2}\right]^2 \frac{d^2P(p)}{d\omega d\Omega} npY$$

$$= 2\int d\Omega \int dk\ k^2\ f_H(k)\ \frac{d^2P(p)}{d\omega d\Omega} npY$$

Figure VI-4 is the plot of the momentum density distribution $4\pi k^2 f_H(k)$. It has the value zero at k=0, goes through a maximum and drops off again at large k as can be seen from the graph.

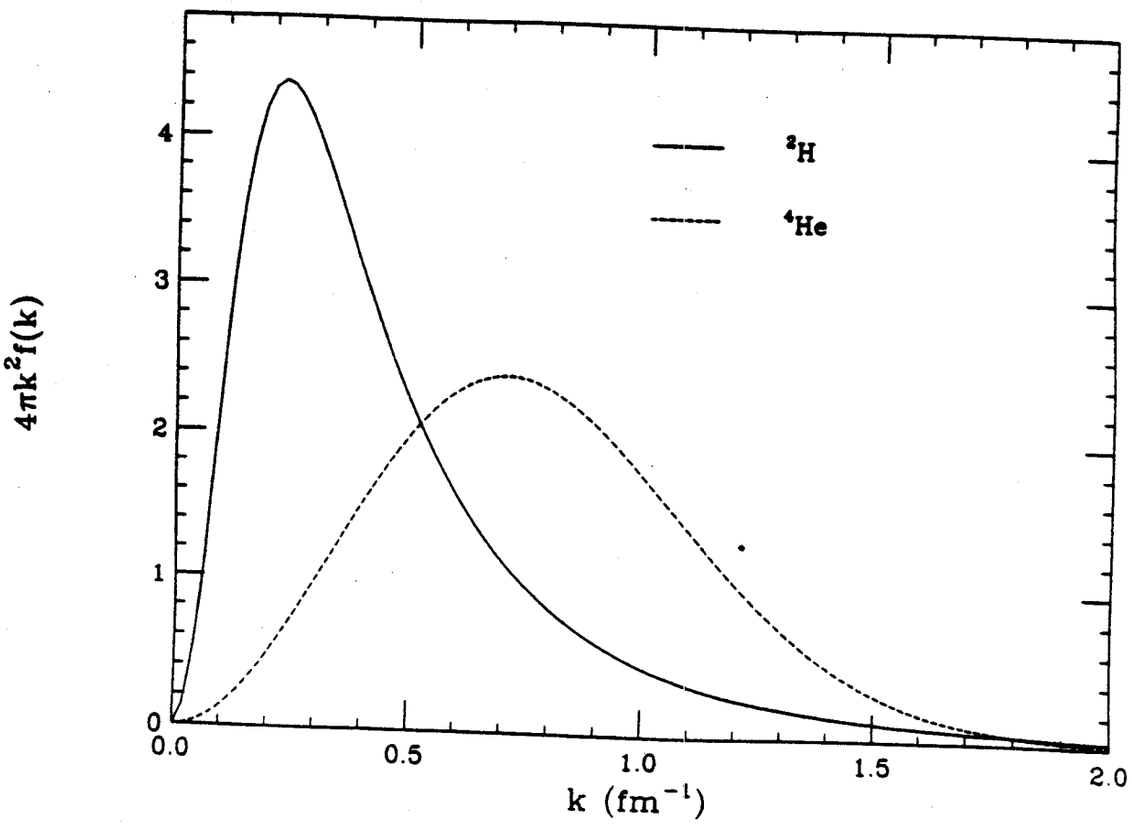

Figure VI-4 ^{2}H and ^{4}He internal momentum distributions.

C.2.2. Internal Momentum Distribution of ^{4}He

For ^{4}He projectile, we use the spherical harmonic oscillator wave function to approximate the behavior of the individual nucleons within the nucleus. In coordinate space, the wave function is:

$$\psi(\vec{r}) = N\, e^{-\nu r^2/2} = N\, e^{-\nu x^2/2} e^{-\nu y^2/2} e^{-\nu z^2/2}$$

Here, $\nu \sim 0.49$. To find the proper normalization constant, we make

$$|\psi(\vec{r})|^2 = N^2 \int e^{-\nu x^2} dx \int e^{-\nu y^2} dy \int e^{-\nu z^2} dz = N^2 \left(\left(\frac{\pi}{\nu}\right)^{1/2}\right)^3 = 1$$

i.e. $$N^2 = \left(\frac{\nu}{\pi}\right)^{3/2}$$

Therefore, we obtain:

$$\psi(\vec{r}) = \sqrt{\left(\frac{\nu}{\pi}\right)^{3/2}}\, e^{-\nu r^2/2}$$

Its Fourier transform is:

$$\psi(\vec{k}) = (2\pi)^{-3/2} \int d^3r\, \psi(r)\, e^{-i\vec{k}\cdot\vec{r}}$$

$$= N(\nu)^{-3/2} e^{-k^2/2\nu}$$

$$= \sqrt{\left(\frac{\pi}{\nu}\right)^{3/2}}\, e^{-k^2/2\nu}$$

This is then the wave function for ^{4}He in momentum space.

The bremsstrahlung probability is then obtained by integrating over all possible momenta of the individual nucleons in the ^{4}He nucleus.

$$\frac{d^2P}{d\omega d\Omega}\Big|_{He} = 4\int d^3p f_{He}(p)\,\frac{d^2P(p)}{d\omega d\Omega}_{npY} = 4\int d^3p\,|\psi_{He}(p)|^2\,\frac{d^2P(p)}{d\omega d\Omega}_{npY}$$

$$= 4\int d^3k\left(\frac{\pi}{\nu}\right)^{3/2} e^{-k^2/\nu}\,\frac{d^2P(p)}{d\omega d\Omega}_{npY}$$

$$= 4\int d\Omega\int dk\; k^2\left(\frac{\pi}{\nu}\right)^{3/2} e^{-k^2/\nu}\,\frac{d^2P(p)}{d\omega d\Omega}_{npY}$$

$$= 4\int d\Omega\int dk\; k^2\, f_{He}(k)\,\frac{d^2P(p)}{d\omega d\Omega}_{npY}$$

The momentum density distribution $4\pi k^2 f_{He}(k)$ is also plotted (in dash line) in Figure VI-4. We can clearly see from the graph that the maximum of the momentum density peaks at a much higher momentum compared to that of the ^{2}H nucleus. That is, the nucleons within the ^{4}He nucleus have a larger probability of having a higher internal momentum.

C.3. Result of the Calculation and Comparison with Data

The bremsstrahlung photon cross sections were obtained by multiplying the bremsstrahlung probability by the geometrical cross section πR^2 ($R = 1.2A_t^{1/3}$) of the target. Figure VI-5 shows the result of our calculation for 53 MeV/nucleon ^{2}H + Pb and ^{4}He + Pb at 90° angle. Both the data and the calculated spectra for the ^{2}H + Pb case are shifted down by a factor of 10 for clarity. The calculation reproduces the slope of the spectrum for the ^{2}H

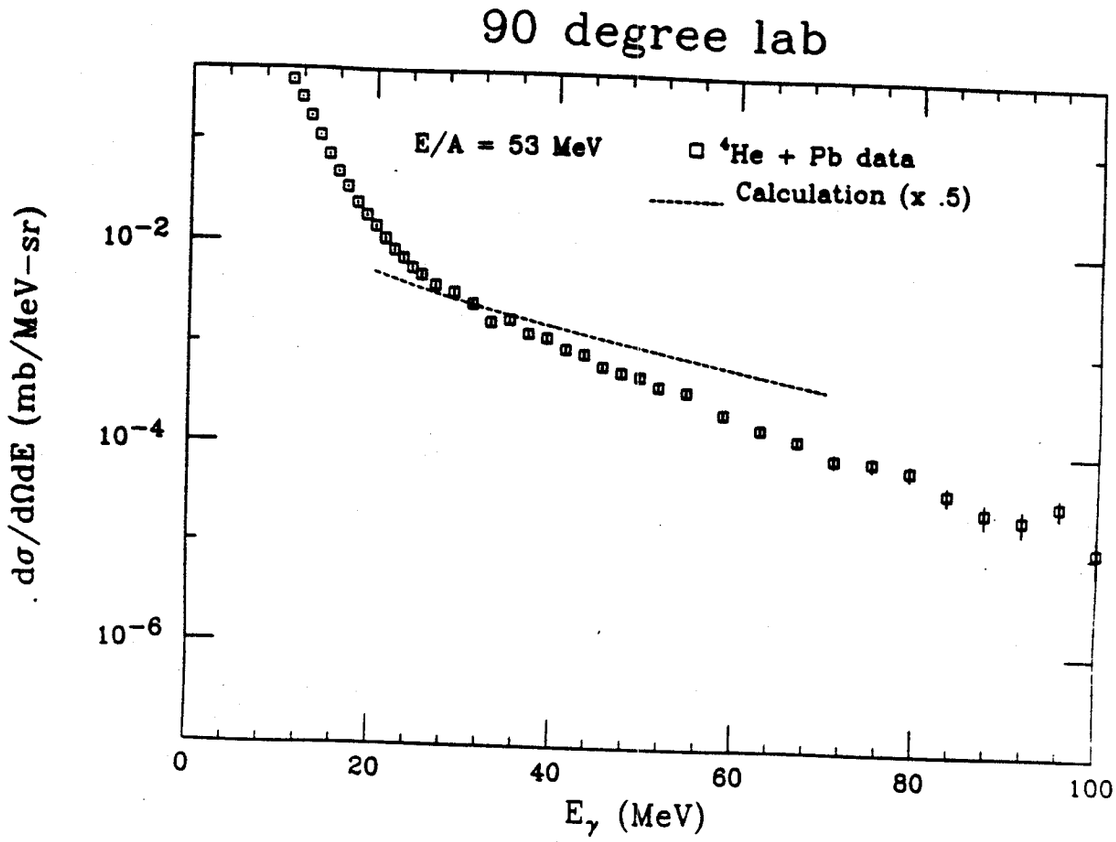

Figure VI-5 Comparison of the photon energy spectra with calculation from the first chance bremsstrahlung model using non-zero temperature internal momenta distribution functions shown in Figure VI-4.

+ Pb, but the overall strength is a factor of 2 larger than the data (in the Figure, the calculated spectra has been shifted down by a factor of 2 for comparison of the slope with the data). However, the predicted slope parameter for the ^{4}He + Pb was too flat when compared with data, and the magnitude of the calculated spectrum is also too large. This failure may come from our use of the harmonic oscillator wave function, which were known to have a high momentum tail, as a model to describe the internal momentum of the ^{4}He nucleus. Therefore, we were not able to establish evidence on the effect of the internal momentum distribution on the bremsstrahlung photon spectra.

C.4. Modified Internal Momentum Distribution Function for ^{2}H and ^{4}He

The difficulty of finding a simple yet realistic analytical expression for the momentum distribution of the light-ion projectiles, particularly for ^{4}He in this case, presents a major obstacle. A different approach to this problem has to be made to investigate the role the proton (or neutron) internal momentum plays in the production of high energy photon. Figure VI-6 shows the deuteron internal momentum distribution function $f_H(p)$ we obtained in the last section. Employing this distribution function, we were able to predict the the shape of the bremsstrahlung photon cross section induced by ^{2}H at 53 MeV/nucleon as shown in the previous section. We decided to replace this distribution with a simpler zero temperature Fermi gas distribution, shown as the solid line in the figure. Conserving the total population, we arrived at a Fermi sphere of radius $p_F = 0.15$ fm^{-1}. Using this new distribution function as the internal momentum distribution of the ^{2}H nucleus, we again calculated the energy spectrum of the 53 MeV/nucleon ^{2}H +

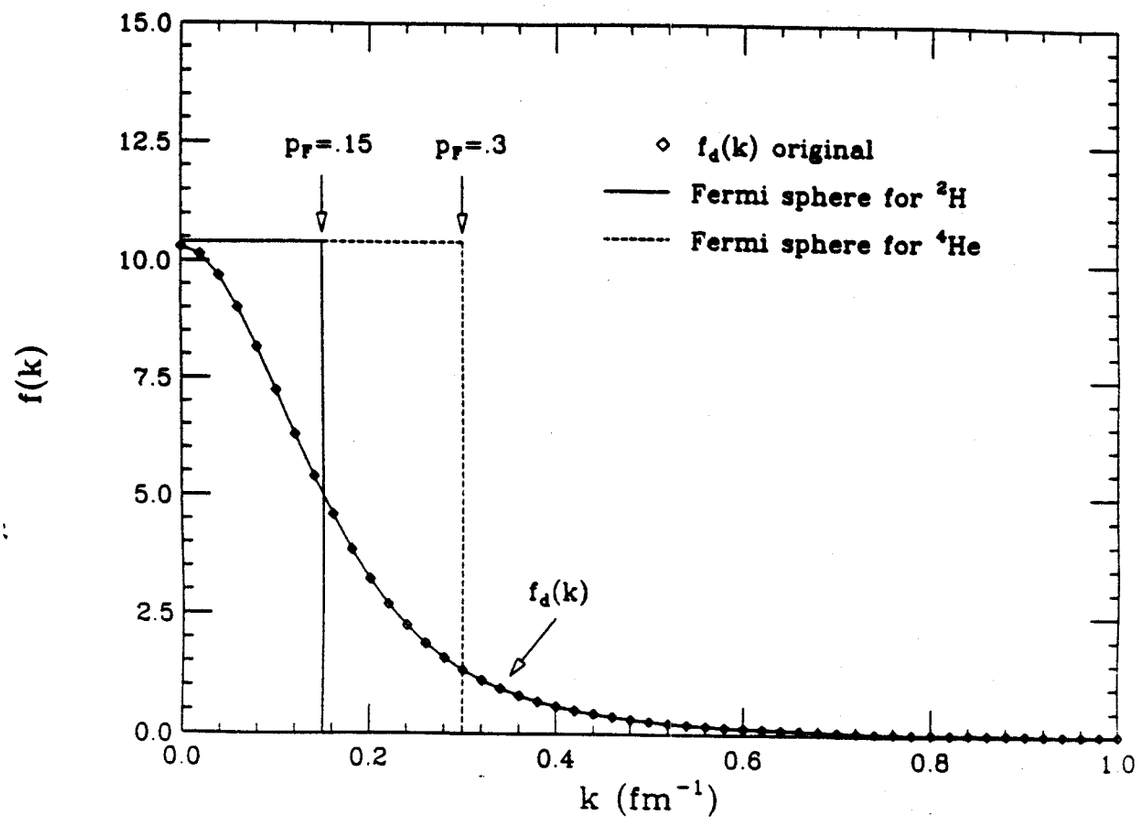

Figure VI-6 Zero-degree-temperature Fermi spheres for ^{2}H and ^{4}He.

Pb at 90° laboratory angle. The resulting spectrum is shown on Figure VI-7, also plotted on the same graph is the experimental data for comparison. The calculated photon yields fall off sharply at energies above 50 MeV because of the sharp cut-off in the deuteron internal momentum distribution. Nevertheless, the calculation was able to predict the slope of the spectrum in spite of the simple minded approximation in the momentum distribution.

Alpha particles not only have one more neutron plus one more proton than deuteron, the individual nucleons within alpha particle also have higher internal momenta. Therefore, the Fermi sphere for ^{4}He nucleus must contain higher momentum, i.e. a larger Fermi radius. We chose the Fermi sphere having twice the radius of the ^{2}H, p_F= 0.3, shown in Figure VI-6 by the dashed line. The energy spectrum of 53 MeV/nucleon ^{4}H + Pb at the 90° laboratory angle was calculated. Figure VI-8 shows the comparison between the energy spectra of ^{2}H + Pb and ^{4}He + Pb both at 53 MeV/nucleon incident energy. The spectrum of ^{4}He + Pb has a larger yield and a flatter slope than the spectrum of ^{2}H + Pb. The predicted spectrum is compared with the data for the 53 MeV/nucleon ^{4}He + Pb reaction at the 90° laboratory angle (Figure VI-9). We find the predicted yield is a factor of 2 larger than the data, while the agreement in slope parameter is quite satisfactory. Therefore, the difference in the internal momentum distribution of both systems having the same energy/nucleon can be responsible for the different slope parameter we observed.

D. Conclusion

We have calculated in this chapter, using the BUU model by Bauer et al., both the reactions of symmetric systems and the light-ion induced

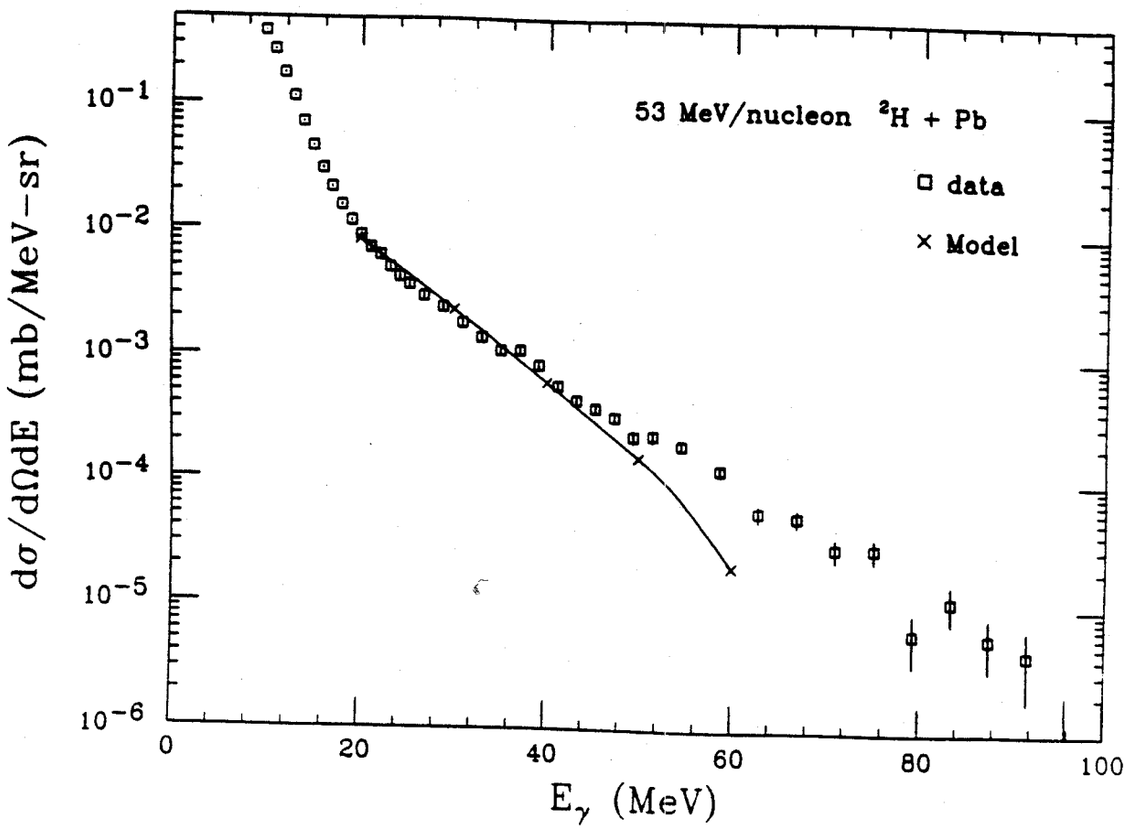

Figure VI-9 Comparison between experimental data and calculations using the zero temperature internal momentum distribution shown in Figure VI-6 for 53 MeV/nucleon ^{4}He + Pb.

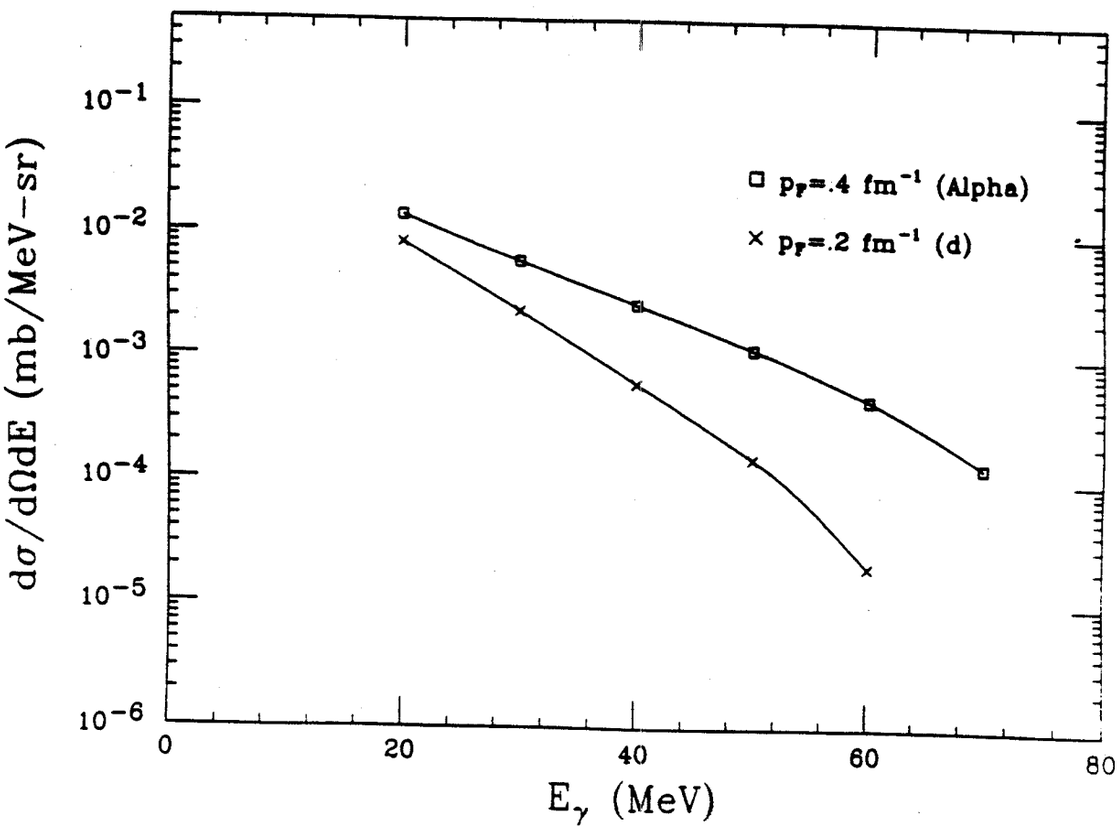

Figure VI-8 First chance np bremsstrahlung model calculations for ^{2}H + Pb and ^{4}He + Pb reactions assuming the zero-degree-temperature Fermi gas as internal momentum distribution fuctions (shown in Figure VI-6).

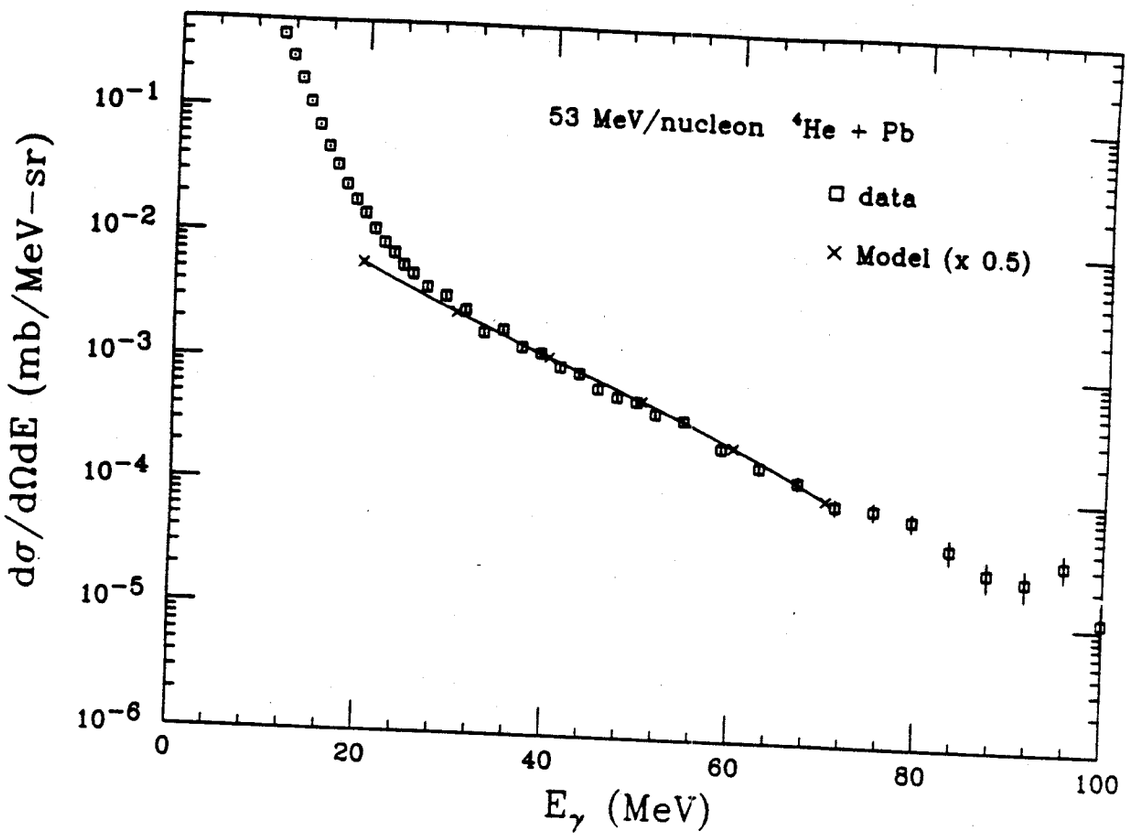

Figure VI-7 Comparison between experimental data and calculations using the zero temperature internal momentum distribution shown in Figure VI-6 for 53 MeV/nucleon ^{2}H + Pb.

reactions. The BUU model was able to reproduce most of the energy spectra of the symmetric system data reasonably well. But it failed to predict the correct slope and overall strength of the light-ion data, probably due to its use of some of the parameters that are more suitable for heavy-ion systems. The predicted angular distributions in the nucleon-nucleon center-of-mass frame, which are backward peaked, disagree with the data. The discrepancy may be due to an overestimation of multiple scattering within the colliding nucleus.

We adapted the first-chance collision Fermi gas model, proposed by Nakayama and Bertsch, to study the effects of internal momentum of the light-ions on the production probability of bremsstrahlung photons. The calculation was in good agreement with the data from 53 MeV/nucleon ^{2}H + Pb reaction. But the agreement with the 53 MeV/nucleon ^{4}He + Pb data was poor, due to the poor approximation of the internal momentum distribution we have chosen. In order to investigate the projectile dependence of the photon cross section, a simplified internal momentum distribution, zero temperature Fermi gas, was used. Using this new approximation of the internal momentum distribution, the model was able to reproduce the data of ^{2}H + Pb. Then by varying the size of the Fermi sphere, we found that $p_F = 0.3\ fm^{-1} = 2p_F(^{2}H)$ gives the best agreement with the slope parameter of the 53 MeV/nucleon ^{4}He + Pb data. This calculation shows, for the light-ion case, the increased internal momentum within the ^{4}He projectile could be an important contributing factor for the flatter slopes in the ^{4}He induced bremsstrahlung photon energy spectra.

Chapter 7

Summary

The high energy gamma rays produced in both the light-ion induced reactions and the symmetric systems have exponentially decreasing energy spectra. The double differential cross sections in the nucleon-nucleon center-of-mass frame can be characterized by a function of the form $A(1-B\cos^2\theta)e^{-E/T}$.

The angular distributions are symmetric about 90° in the nucleon-nucleon center-of-mass frame. All of the reactions we studied show a dipole component superimposed on an isotropic component. The relative strength of the dipole component ranges from 29% to 49% for the heavy-ion induced reactions and up to 60% in light-ion on carbon target reactions. We also detected a trend of increased dipole components with the decrease in the masses of the systems. We observed no evidence of quadrupolar angular distribution in the center-of-mass frame.

The slope parameters obtained for all of the heavy-ion induced systems we studied are in general agreement with data at the same energy measured by other groups with similar systems. The slope parameters in the light-ion induced reactions are substantially smaller than those found in heavy-ion induced reactions at similar systems. The projectile dependence in light-ion induced reactions may be due to the difference in the projectile internal momentum distribution. A calculation based on first-chance n-p bremsstrahlung model was able to reproduce the different slopes of ^{4}He and

^{2}H at the same energy. We also observed target mass dependence in the slope parameter T for both the light-ion and heavy-ion induced reactions.

For the three symmetric systems at E/A = 30 MeV, the integrated photon cross sections for gamma ray energy above 30 MeV are in good agreement with the incoherent bremsstrahlung $(A_p A_t)^{2/3}$ scaling scheme. The ratios of the bremsstrahlung photon total cross section provide no evidence to support the Z^2 charge dependence predicted by the coherent bremsstrahlung model.

List of References

A

Al 86 N. Alamanos, P. Braun-Munzinger, R. F. Freifelder, P. Paul, J. Stachel, T.C. Awes, R. L. Ferguson, F. E. Obenshain, F. Plasil, and G. R. Young, Phys. Lett. 173B, 392 (1986).

B

Ba 86a W. Bauer, W. Cassing, U. Mosel, and M. Tohyama, Nucl. Phys. A456, 159 (1986)

Ba 86b W. Bauer, G. F. Bertsch, W. Cassing, and U. Mosel, Phys. Rev. C 34, 2127 (1986)

Ba 87 W. Bauer, T. S. Biro, W. Cassing, U. Mosel, K. Niita, A. L. De Paoli, G. F. Bertsch, "Proceedings of the XXV international Winter Meeting on Nuclear Physics", Bormio, Italy, Jan. (1987)

Be 85 K. B. Beard, W. Benenson, C. Bloch, E. Kashy, J. Stevenson, D. J. Morrissey, J. ban der Plicht, B. Sherrill, and J. S. Winfield, Phys. Rev. C 32, 1111 (1985)

Be 87 R. Bertholet, M. Kwato Njock, M. Maurel, E. Monnand, H. Nifenecker, P. Perrin, J. A. Pinston, F. Schussler, D. Barneoud, C. Guet, and Y. Schutz, Nucl. Phys. **A474**, 541 (1987)

Bo 88 A. Bonasera, and colleagues, Nucl. Phys. **A483**, 738 (1988)

C

Ca 86 W. Cassing, T. Biro, U. Mosel, M. Tohyama, and W. Bauer, Phys. Lett. **181B**, 217 (1986)

D

De 67 S. DeBenedetti, "Nuclear Interactions" p.47

E

Ed 66 J. A. Edgington and B. Rose, Nucl. Phys. **89**, 523 (1966)

Ev 55 R. D. Evans, "The Atomic Nucleus"

G

Gr 85 E. Grosse, in "Proceedings of the International Workshop on Gross Properties of Nuclei and Nuclear Excitations XIII", Hirschegg, Austria, 1985 (edited by H. Feldmerier) p.65

Gr 86 E. Grosse, P.Grimm, H. Heckwolf, W. F. J. Mueller, H. Noll, A. Oskarson, H.Stelzer, and W. Roesch, Europhysics Lett. 2, 9 (1986).

H

Ha 68 G. D. Harp, J. M. Miller, and B. J. Berne, Phys. Rev. 165, 1166 (1968)

He 84 N. Herrmann, P. Braun-Munzinger, and A. Gobbi, GSI Scientific Report, 48 (1984)

He 86 N. Herrmann, R. Bock, H. Emling, R. Freifelder, A. Gobbi, E. Grosse, K. D. Hildenbrand, R. Kulessa, T. Matulewicz, F. Rami, R. S. Simon, H. Stelzer, J. Wessels, P. R. Maurenzig, A. Olmi, A. A. Stefanini, W. Kuhn, V. Metag, R. Novotny, M. Gnirs, D. Pelte, P. Braun-Munzinger, L. G. Moretto, GSI Scintific Report, 48 (1986)

Hi 87 R. Hingmann, W. Kuhn, V. Metag, R. Muhlahans, R. Novotny, A. Ruckelshausen, W. Cssing, B. Haas, J. P. Vivien, A. Boullay, H. Delagrange, H. Doubre, C. Gregoire, Y. Schutz, Phys. Rev. Lett. 58, 759 (1987).

J

Ja 75a J. D. Jackson "Classical Eletrodynamics" p.376

Ja 75b J. D. Jackson "Classical Eletrodynamics" p.705

K

Ko 85 C. M. Ko, G. Bertsch, and J. Aichelin, Phys. Rev. C **31**, 2324 (1985)

Kw 86 M. Kwato Njock, M. Maurel, E. Monnand, H. Nifenecker, J. Pinston, F. Schussler, and D. Barneoud, Phys. Lett. **175B**, 125 (1986)

Kw 88a M. Kwato Njock, M. Maurel, H. Nifenecker, J. A. Pinston, F. Schussler, D. Barneoud, S. Drissi, J. Kern, J. P. Vorlet, Phys. Lett. B **207**, 269 (1988)

Kw 88b M. Kwato Njock, M. Maurel, H. Nifenecker, J. A. Pinston, F. Schussler, Y. Schutz, to be published in Nucl. Phys. and Proceedings of the 3rd International Conference on Nucleus-Nucleus Collisions St-Malo, June 1988

L

La 88 A. R, Lampis, J. Stevenson, W. Benenson, J. Clayton, D. Cebra, Y. Chen, D. Fox, E. Kashy, D. J. Morrissey, M. Samuel, R. Smith, C.

L. Tam, G. D. Westfall, K. Wilson, and J. S. Winfield, Phys. Rev. C 38, 1961 (1988)

M

Mo 69 J. W. Mothz, H. A. Olsen, and H. W. Koch, Rev. Mod. Phys 41, 581 (1969)

N

Na 86 K. Nakayama and G. F. Bertsch, Phys. Rev. C 34, 2190 (1986)

Ne 85 W. R. Nelson, Hideo Hirayama, and D. W. O. Rogers, SLAC-265 UC-32 (1985).

Ne 87 D. Neuhauser, and S. E. Koonin, Nucl. Phys. A462, 163 (1987)

Ni 85 H. Nifenecker, and J. P. Bondorf, Nucl. Phys. A442, 478 (1985)

Pi 88 J. A. Pinston, Phys. Lett. (1988) in print

Pr 86 M. Prakash and colleagues, Phys. Rev. C 33, 937 (1986)

R

Re 87 B. A. Remington, M. Blann, G. F. Bertsch, Phys. Rev. C **35**, 1720 (1987)

S

St 86 J. Stevenson, K. B. Beard, W. Benenson, J. Clayton, E. Kasky. A. Lampis, D. J. Morrissey, M. Samuel, R. J. Smith, C. L. Tam, and J. S. Winfield. Phys. Rew. Lett. **57**, 555 (1986).

Sp 67 J. E. Spencer and H. A. Enge, Nucl. Instr. and Meth. **49**, 81 (1967)

V

Va 85 D. Vasak, Berndt Muller and Walter Greiner,J. Phys. G: Nucl. Phys. **11**, 1309 (1985).

Va 86 D. Vasak, Phys. Lett. **176B**, 276 (1986)